
Unterschrift des Betreuers



TECHNISCHE
UNIVERSITÄT
WIEN

DIPLOMARBEIT

Dissipative Losses in Self-Interacting Dark Matter Collisions

Lukas Semmelrock

Weisselgasse 26/2, 1210 Wien

ausgeführt am

Institut für Theoretische Physik der Technischen Universität Wien

unter der Leitung von

Prof. Dr. Anton Rebhan

in Verbindung mit dem

Institut für Hochenergiephysik der Österreichischen Akademie der Wissenschaften

unter der Leitung von

Dr. Josef Pradler

Eingereicht am 11.05.2016

Unterschrift

Abstract

Dark matter self-interactions are frequently put forward in the explanation of small structure problems in the universe. They could have important implications on the formation and evolution of structures, from dwarf galaxies to large galaxy clusters. In this thesis, the effects of bremsstrahlung in self-interacting dark matter collisions on structure formation are analyzed. For that purpose, four different dark matter models are studied perturbatively in a non-relativistic and non-degenerate limit. Cross sections and energy loss rates are calculated analytically for all models for vanishing masses of the mediator and emitted particle and numerically for finite masses. To analyze the effect of radiative cooling on structure formation, the cooling time of a gas of dark matter particles t_{cool} , based on perturbative calculations, is compared to the elastic scattering time scale t_{el} , the Hubble time t_0 and the gravitational timescale t_{grav} . Results show that for a fiducial dark matter density $\rho_\chi = 1 \text{ GeV/cm}^3$ the condition $t_{\text{cool}} < t_0$ can be fulfilled for particle-particle scattering if $m_\chi/\alpha \lesssim 100 \text{ MeV}$ and for particle-antiparticle scattering if $m_\chi/\alpha \lesssim 100 \text{ GeV}$ and that therefore radiative cooling has an influence on the formation of structures. Considering the observational constraint $\sigma_T/m_\chi \lesssim 1 \text{ cm}^2/\text{g}$ at cluster scales of $v_\chi \sim 10^{-2}$, it was found that $t_{\text{el}} < t_{\text{cool}} < t_0$ can be fulfilled if $m_\chi/\alpha^{3/2} \gtrsim 10 \text{ GeV}$ with dark matter densities $\alpha \rho_\chi \gtrsim 10^6 \text{ GeV/cm}^3$ for $\chi\chi$ -scattering and $\alpha \rho_\chi \gtrsim 10^2 \text{ GeV/cm}^3$ for $\chi\bar{\chi}$ -scattering.

Deutsche Kurzfassung

Selbst-Wechselwirkungen von Dunkler Materie werden häufig zur Erklärung der Kleinstrukturprobleme im Universum verwendet. Sie könnten wichtige Auswirkungen auf die Entstehung und Entwicklung von Strukturen haben, von Zwerggalaxien bis großen Galaxienhaufen. In dieser Arbeit werden die Auswirkungen von Bremsstrahlung in Kollisionen von selbst-wechselwirkender Dunkler Materie auf die Strukturbildung im Universum analysiert. Zu diesem Zweck werden vier verschiedene Dunkle Materie Modelle störungstheoretisch im nicht-relativistischen und nicht-entarteten Regime untersucht. Wirkungsquerschnitte und Energieverlustraten werden analytisch für alle Modelle berechnet. Für verschwindende Masse des Austausch- und emittierten Teilchens werden analytische Lösungen angegeben, während für endliche Massen auf numerische Lösungsverfahren zurückgegriffen wird. Um die Wirkung der Strahlungskühlung eines Dunkle-Materie-Gases auf die Strukturbildung zu analysieren, wird die Abkühlzeit t_{cool} basierend auf störungstheoretischen Berechnungen mit der Zeitskala elastischer Streuungen t_{el} , der Hubble-Zeit t_0 und der gravitativen Zeitskala t_{grav} verglichen. Es zeigt sich, dass für eine Referenzdichte von Dunkler Materie $\rho_\chi = 1 \text{ GeV/cm}^3$ die Forderung $t_{\text{cool}} < t_0$ für Teilchen-Teilchen Streuung durch $m_\chi/\alpha \lesssim 100 \text{ MeV}$ und für Teilchen-Antiteilchen Streuung durch $m_\chi/\alpha \lesssim 100 \text{ GeV}$ erfüllt werden kann und Strahlungskühlung in diesen Fällen daher einen Einfluss auf die Strukturbildung im Universum hat. Unter Berücksichtigung von astronomischen Beobachtungen, die auf Größenskalen von Galaxienhaufen mit $v_\chi \sim 10^{-2}$ den elastischen Streuquerschnitt auf $\sigma_T/m_\chi \lesssim 1 \text{ cm}^2/\text{g}$ beschränken, zeigt sich, dass $t_{\text{el}} < t_{\text{cool}} < t_0$ erfüllt werden kann, wenn $m_\chi/\alpha^{3/2} \gtrsim 10 \text{ GeV}$ mit Dunkle-Materie-Dichten von $\alpha \rho_\chi \gtrsim 10^6 \text{ GeV/cm}^3$ für $\chi\chi$ -Streuung und $\alpha \rho_\chi \gtrsim 10^2 \text{ GeV/cm}^3$ für $\chi\bar{\chi}$ -Streuung.

Acknowledgements

I would first like to thank my research advisor Josef Pradler for giving me the opportunity to write my diploma thesis in his group and proposing this interesting topic. His office door was always open for me whenever I had questions or ran into problems, which lead to many interesting discussions. I have learned a lot in the past year, not only about particle physics but also about the world of research in general and I am very grateful for having been able to conduct my diploma thesis at the Institute of High Energy Physics. I also want to thank Prof. Anton Rebhan from the Institute of Theoretical Physics for the official supervision of my thesis.

I would like to thank Johannes Brandstetter for drawing my attention to the dark matter theory group in the first place and for the many visits to my office telling me about his everyday shenanigans. I would like to thank him, Thomas Madlener and Philipp Moser for inspiring discussions about physics and physics-related topics at our monthly “journal club” and I want to thank all my other fellow students, who have become great friends to me, for the most pleasant and fun times.

I also want to express my gratitude to Kathrin Bednar for her support and encouragement throughout the past years and for making my life happier. I know that it is not always easy to listen to my everyday physics problems, but I appreciate her listening anyway. Finally, I want to thank my parents for making it possible for me to study physics and for always supporting me and I want to thank my brother and all my friends for making the past years in Vienna an unforgettable time.

Contents

1	Introduction	1
2	Dark Matter	3
2.1	Evidence for Dark Matter	3
2.2	Cosmological Model (Λ CDM)	5
2.3	Structure Formation	7
2.4	Dark Matter Density Distribution in the Universe	14
2.5	Particle Dark Matter	16
3	Dissipation in Self-Interacting Dark Matter Models	21
3.1	S-Matrix, Cross Section and Energy Loss Rate	22
3.2	Fermion Scattering	25
3.2.1	Yukawa Interaction	27
3.2.2	Gauge Interaction	33
3.3	Scalar Boson Scattering	36
3.3.1	Gauge Interaction	38
3.3.2	Scalar Interaction	41
3.4	Elastic Scattering Cross Section	46
4	Effects of Dissipation on Structure Formation	51
5	Conclusions and Outlook	65
A	Appendix	69
A.1	Massive $U(1)$ Gauge Field	69
A.2	Feynman Rules and Amplitudes	71
A.3	Calculation of $ \mathcal{M} ^2$ for $\chi\chi \rightarrow \chi\chi\phi$	76
A.4	Phase Space Integration	82
	References	85

List of Figures

2.1	Dark matter: rotation curve of NGC 6503	4
2.2	Power spectrum of the CMB measured by <i>Planck</i>	6
2.3	Density evolution during structure formation in the universe	9
2.4	Halo mass range during the evolution of the universe	13
2.5	Cusp vs. core problem: rotation curve of F568-3	16
3.1	Tree level diagrams for fermion scattering	26
3.2	Scalar potential with and without vacuum expectation value	28
3.3	Effects of finite scalar mass on $\chi\chi \rightarrow \chi\chi\varphi$	31
3.4	Effects of finite vector boson mass on $\chi\chi \rightarrow \chi\chi V$	34
3.5	Comparison of energy loss rate of $\chi\chi \rightarrow \chi\chi V$ and $\chi\bar{\chi} \rightarrow \chi\bar{\chi} V$	36
3.6	Additional tree level diagrams for scalar boson scattering	37
3.7	Comparison of energy loss rates for fermionic and scalar CDM	40
3.8	Energy loss rate for trilinear coupling	43
4.1	t_{cool} in the ρ, T -plane for a gauge coupling.	56
4.2	t_{cool} in the ρ, T -plane for a gauge coupling.	57
4.3	t_{cool} in the M, z -plane for a gauge coupling.	60
4.4	t_{cool} in the M, z -plane for a gauge coupling.	61

List of Tables

3.1	Summary of energy loss rates	45
4.1	Bounds on m_χ/α for particle-particle scattering	54
4.2	Bounds on m_χ/α for particle-antiparticle scattering	55
4.3	Energy loss rate suppression factors	58

Nomenclature

BSM	Beyond the Standard Model
CMB	Cosmic Microwave Background
CDM	Cold Dark Matter
DM	Dark Matter
Λ CDM	Cosmological Standard Model
QED	Quantum Electrodynamics
SIDM	Self-Interacting Dark Matter
SM	Standard Model of particle physics
WIMP	Weakly Interacting Massive Particle

Units

In this thesis natural units $\hbar = c = k_B = 1$ are used and the electron volt (eV) is chosen to be the unit for mass and energy. The gravitational constant in natural units is $G = 6.709 \times 10^{-39} \text{ GeV}^{-2}$ and the Hubble constant $H_0 = 1.58 \times 10^{-36} \text{ GeV}$. To convert results from natural units to SI units, the following relations are used:

Distance:	$1 \text{ eV}^{-1} = \frac{\hbar c}{1 \text{ eV}} = 1.97 \times 10^{-7} \text{ m}$
Time:	$1 \text{ eV}^{-1} = \frac{\hbar}{1 \text{ eV}} = 6.58 \times 10^{-16} \text{ s}$
Mass:	$1 \text{ eV} = \frac{1 \text{ eV}}{c^2} = 1.78 \times 10^{-36} \text{ kg}$
Temperature:	$1 \text{ eV} = \frac{1 \text{ eV}}{k_B} = 1.16 \times 10^4 \text{ K}$

Introduction

For many centuries, scientists have been studying the motion of astrophysical objects, trying to deduce physical laws of gravitation from their trajectories and, in turn, predicting future positions of planets, solar systems, or even whole galaxies to verify said laws. In the course of this interplay of theory and observation, yet too often discrepancies arose which could only be explained by either theory or observation being wrong. In other words, either the theory of gravitation was incomplete and hence needed to be modified, or the influence of unseen objects was causing the conflict which could be resolved by finding these objects. Both approaches have proven right in different situations in the past¹. In 1846 for example, Neptune was discovered and found responsible for the anomalous motion of Uranus. A few years later, Mercury's perihelion precession was discovered, which lead to the prediction of a new planet, Vulcan, which was never found. In this case, a modification of gravitational theory, *i.e.* Einstein's theory of general relativity formulated in 1915, was able to resolve the problem and fully explain Mercury's motion.

In the course of the 20th century, various observations were made that could not be explained by our gravitational laws governing the visible matter in the universe. First indications of anomalies arose with rather imprecise measurements by Oort of orbital velocities of stars in the Milky Way in 1932 which were supported by Zwicky [2, 3] in the following years who studied the motion of galaxies in clusters. Several decades later, more stringent evidence was found by measuring rotation curves of galaxies [4, 5] and weak gravitational lensing of the Bullet cluster [6]. All this data could not be explained with the current knowledge about the matter distribution in these structures using the laws of gravitation. Like earlier in history, part of the scientific community

¹as nicely presented in Ref. [1]

tried to explain the observations by altering gravitational theory, known as “Modified Gravity” [7], others by introducing new particles, known as “Dark Matter” [1]. Each theory bares some difficulties and the “truth” could be a combination of both. In this thesis a non-modified theory of gravitation will be assumed. Several generic dark matter models will be analyzed in order to find out how properties of dark matter can influence structure formation in the universe.

The thesis is structured as follows: Chapter 2 will give an introduction to dark matter and its distribution in the universe. Assuming that dark matter only interacts gravitationally, N-body simulations of the evolution of our universe have been a huge success in explaining structure formation at large scales but have problems when it comes to reproducing the observed dark matter density distribution at small scales. The discrepancies between simulation and observation can be divided into three categories known as the three big problems of dark matter structure evolution in the universe [8]. These problems, however, may be resolved assuming dark matter is not only influenced by gravitation, but also has a self-interaction [9]. In Chap. 3, several models of self-interacting dark matter will be introduced. The role of bremsstrahlung in such self-interactions will be analyzed and cross sections and energy loss rates will be calculated for different scenarios. In Chap. 4, the cooling time of a gas of particles due to dissipation will be compared with the time scale of a collisionless gravitational collapse, with the Hubble time and with the average time between two elastic collisions in order to estimate whether the energy loss due to bremsstrahlung is a relevant factor for structure formation in the universe. The conclusions will be presented in Chap. 5.

Dark Matter

Dark Matter (DM) is a substance that to our current knowledge makes up 26% [10] of the energy content of our universe. It is assumed to be made up of particles, like ordinary matter, but has to behave very differently, feebly or not at all interacting with light or any other forces in the standard model of particle physics (SM). If it interacts with ordinary matter, the interaction is very weak, which is why DM has never been observed in laboratory experiments. To this date, the only direct evidence for dark matter in the universe is of gravitational kind.

2.1 Evidence for Dark Matter

The historically first evidence for DM stems from observations of rotational velocities of matter around its center of gravity. Starting with Oort and Zwicky, who measured velocities of stars in the Milky Way (MW) and velocity dispersions of galaxies in clusters respectively, the most frequently cited evidence for DM nowadays is probably the observation of rotation curves of galaxies [5]. Following Newtonian dynamics, for an approximately circular movement of matter around the center of a galaxy, its velocity v as a function of the distance from the center r is given by

$$v(r) = \sqrt{\frac{GM(r)}{r}}, \quad (2.1)$$

$$M(r) = 4\pi \int_0^r \rho(r') r'^2 dr' \quad (2.2)$$

where $M(r)$ is the mass within the orbit, $\rho(r)$ is the matter density profile and G the gravitational constant. Beyond the optical disk¹ of baryonic matter, which is

¹Structures of baryonic matter tend to form disks in order to minimize the energy while conserving angular momentum. This is only possible due to energy dissipation and therefore dark matter, which

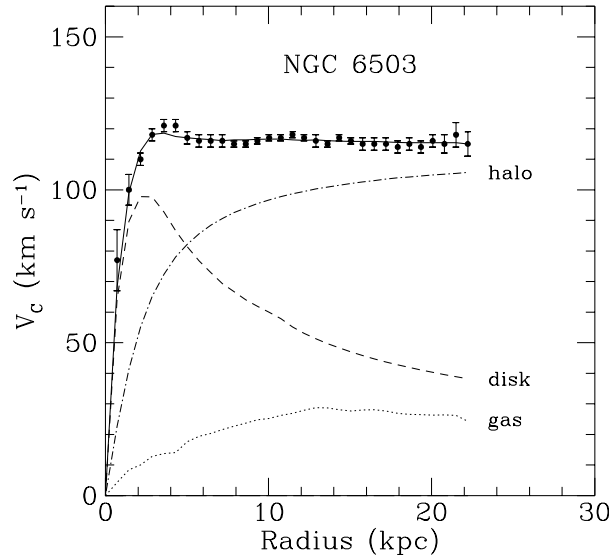


Figure 2.1: Rotation curve of NGC 6503. The dotted, dashed and dash-dotted lines are the contributions of gas, disk and dark matter, respectively [1].

typically $\sim 10 - 50$ kpc in size, M is constant and $v(r) \propto r^{-1/2}$ (compare dashed line in Fig. 2.1). However, observations show that the velocity flattens out at large distances (data points in Fig. 2.1). This implies the existence of a halo² with $M(r) \propto r$ and $\rho(r) \propto r^{-2}$ (dash-dotted line in Fig. 2.1). Explicitly, this means that in order to explain the rotation curves of visible particles in galaxies, we have to add a halo of invisible particles whose density profile falls with the square of the distance from the center of the galaxy. Invisible in this context means, that the particles do not interact via the electromagnetic force and therefore do not absorb or emit light, a property coining the name dark matter.

At the scale of galaxies and galaxy clusters, the evidence for dark matter has become even more compelling through gravitational lensing measurements (*e.g.* of the Bullet cluster [6]) and by studying the profile of X-ray emission that traces the distribution of hot emitting gas in rich clusters [11]. From these measurements at galactic scales, one can deduce local abundances of DM in galactic structures. However, for determining the average density of dark matter in the universe, a more extensive (*i.e.* cosmological) model as well as observational data from large parts of the universe are needed.

in many models is dissipationless, does not show this behaviour.

²A halo is an approximately spherical distribution of matter, which is one of the simplest structures to be formed due to gravitational attraction (for details, see Sec. 2.2).

2.2 Cosmological Model (Λ CDM)

In order to understand the role of dark matter in our universe, it is essential to understand its evolution and the formation of structures therein. Using general relativity, the expansion of the universe from the big bang up to the present time can be described by the Friedmann equations (see, *e.g.*, Ref. [12] or [13])

$$\left(\frac{\dot{a}(t)}{a(t)}\right)^2 + \frac{K}{a(t)^2} - \frac{\Lambda}{3} = \frac{8\pi G}{3}\rho(t), \quad (2.3a)$$

$$\frac{\ddot{a}(t)}{a(t)} - \frac{\Lambda}{3} = -\frac{4\pi G}{3}[\rho(t) + 3p(t)]. \quad (2.3b)$$

These two equations describe the universe as a continuous fluid with ρ being its energy density and p its pressure. They explain the evolution of a homogeneous (*i.e.* the same at every point) and isotropic (*i.e.* the same in every direction) universe, where $a(t)$ is the scale factor of the universe which increases as the universe expands, $\dot{a}(t)/a(t) = H(t)$ is the Hubble rate which is the rate at which the universe doubles its linear size, K its curvature which to our current knowledge is very close to zero and Λ is the cosmological constant. The cosmological constant is usually absorbed into ρ and p by redefining them ($\rho \rightarrow \rho - \Lambda/8\pi G$ and $p \rightarrow p + \Lambda/8\pi G$) yielding the redefined Friedmann equations assuming zero curvature

$$H^2(t) = \frac{8\pi G}{3}\rho(t), \quad (2.4a)$$

$$\frac{\ddot{a}(t)}{a(t)} = -\frac{4\pi G}{3}[\rho(t) + 3p(t)]. \quad (2.4b)$$

The first Friedmann equation (2.4a) tells us, that the rate at which the universe expands is governed by its energy density $\rho(t) = \rho_R(t) + \rho_M(t) + \rho_\Lambda$ where R stands for radiation, M for (dark and ordinary) matter and Λ for dark energy. The energy densities all scale differently with time. So, $\rho_R(t) \propto a(t)^{-4}$, $\rho_M(t) \propto a(t)^{-3}$ and ρ_Λ is constant during the evolution of the universe. From (2.4a) we can define the critical energy density

$$\rho_c(t) = \frac{3H^2(t)}{8\pi G} \quad (2.5)$$

in order to get a normalized energy density parameter

$$\Omega(t) = \frac{\rho(t)}{\rho_c(t)} = \Omega_R(t) + \Omega_M(t) + \Omega_\Lambda(t) = 1 \quad (2.6)$$

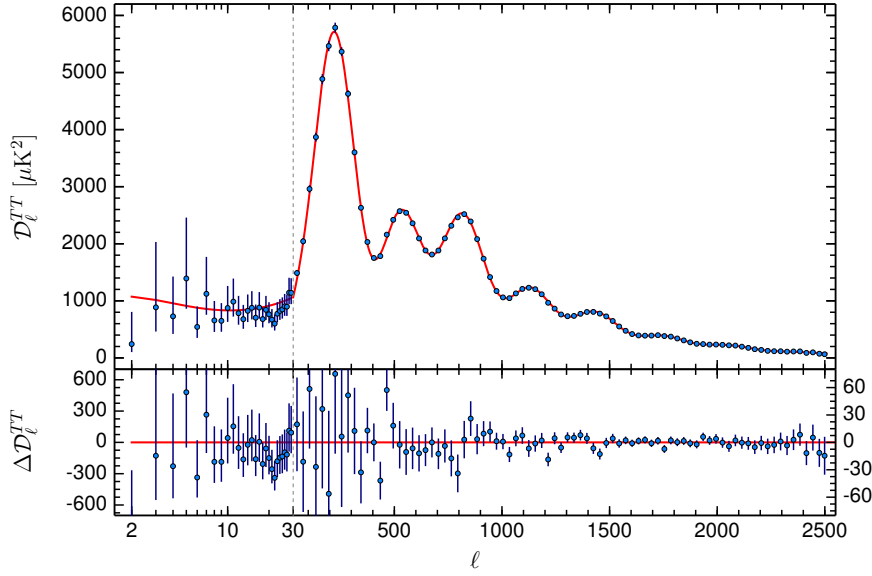


Figure 2.2: Anisotropy of the CMB power spectrum measured by *Planck* [10], with the multipole expansion parameter l on the x -axis and the coefficient of the decomposition into spherical harmonics $D_l = l(l+1)C_l/2\pi$ on the y -axis. The coefficient $C_l \delta_{ll'} \delta_{mm'} = \langle \theta_{lm}^* \theta_{l'm'} \rangle$ with $\theta_{lm} = \int d\Omega Y_{lm}(\hat{n}) [T(\hat{n})/\langle T \rangle - 1]$. The average CMB temperature $\langle T \rangle = 2.7255\text{K}$ and the anisotropies arise at the mK-level. They arise from the interaction between baryonic matter and radiation before the decoupling of the photons. Anisotropies in the baryonic matter density (*i.e.* baryon acoustic oscillations) in the early universe lead to anisotropies in $T(\hat{n})$ and thus in the photon spectrum. Since dark matter does not interact with photons but alters the gravitational potential, the DM density indirectly affects the CMB power spectrum. By fitting the parameters of the Λ CDM-model (red line) onto the CMB spectrum (blue data points) one can deduce the relic DM and baryonic densities to great precision.

whereas the last equality only holds for $K = 0$. The parameters in (2.6) are inferred to great accuracy by analyzing the cosmic microwave background (CMB). The CMB is the background radiation of photons that have been able to stream freely since the universe has cooled down so much that electrons and protons could recombine to form neutral atoms. This happened around 380,000 years after the Big Bang. These photons have been redshifted in the following 13 billion years and are now measurable as microwaves. The spectrum of these photons is almost an ideal black body spectrum, but the small deviations can be used to deduce the abundance of the different kinds of matter and energy in the universe (see Fig. 2.2), which we know today to a precision of a few percent [10]:

$$\Omega_{SM}^0 = 0.04924 \pm 0.00031 \quad (2.7a)$$

$$\Omega_{DM}^0 = 0.2623 \pm 0.0022 \quad (2.7b)$$

$$\Omega_M^0 = \Omega_{SM}^0 + \Omega_{DM}^0 = 0.3089 \pm 0.0062 \quad (2.7c)$$

$$\Omega_R^0 = 5.46(19) \times 10^{-5} \quad (2.7d)$$

$$\Omega_\Lambda^0 = 0.6911 \pm 0.0062 \quad (2.7e)$$

where the superscript 0 denotes that these values refer to the current abundances at $t = t_0$. At this point, it is convenient to introduce the convention of measuring time in terms of the redshift

$$z = \frac{\lambda(t_0) - \lambda(t)}{\lambda(t)} = \frac{a(t_0)}{a(t)} - 1 \quad (2.8)$$

of photons with wavelength λ at a given time t . By this convention the redshift at the time when the CMB was emitted is $z_{CMB} \approx 1100$. The first galaxies were formed at $z \approx 10$. It is worth to notice that the redshift parameter tells us how much smaller the universe was at that time, *i.e.*,

$$\frac{a(t)}{a(t_0)} = \frac{1}{z + 1} \approx \frac{1}{z} \quad \text{for } z \gg 1 \quad (2.9)$$

which tells us that at the emission of the CMB the universe was about 1/1100 of its current size in linear dimension.

Since the energy densities ρ_R , ρ_M and ρ_Λ scale differently in time, their importance in the universe also changes in time. In the universe's early ages, it was hot and dense and dominated by radiation until at a redshift of $z \approx 3600$ (when the universe was about 47,000 years old) $\rho_R = \rho_M$ and so the universe entered its matter dominated era which ruled most of its history in time and where structures could form. It was only in the universe's recent history at a redshift of $z \approx 1$ (about 4 billion years ago) that the universe entered the phase where it is governed by the cosmological constant which accelerates its expansion.

2.3 Structure Formation

The Friedmann equations describe the universe on large scales on which the universe is homogeneous and isotropic and the energy densities can be described by rather simple analytical equations. On smaller scales, however, we know that the universe today is not at all homogeneous and isotropic. The reason for that is the evolution of small

initial over- and under-densities

$$\delta(\vec{x}, t) = \frac{\rho(\vec{x}, t) - \bar{\rho}(t)}{\bar{\rho}(t)} \quad (2.10)$$

during the expansion of the universe, with $\bar{\rho}(t)$ being its mean matter density. The density fluctuations $\delta(\vec{x}, t)$ are assumed to be random at each point in space at a given time. While a general random field $\delta(\vec{x}, t)$ would be very complicated, the initial density field in the Universe is found to be well approximated by a homogeneous and isotropic Gaussian random field [14, p. 204]. The probability for a field configuration δ is

$$P_x(\delta)d\delta = \frac{1}{\sqrt{2\pi\sigma^2}} e^{-\frac{\delta^2}{2\sigma^2}} d\delta \quad (2.11)$$

with $\sigma^2 = \langle \delta^2 \rangle$, which is completely determined by its power spectrum.

During the evolution of the universe, the expansion of matter in over-dense regions (which for simplicity we assume spherically symmetric) lags behind. The evolution of the radius $r(t)$ of material at initial radius r_i in a flat universe without cosmological constant (see Ref. [13, p. 733ff] or [14, p. 215ff]) is governed by Newton's laws,

$$\frac{d^2 r}{dt^2} = -\frac{GM}{r^2}. \quad (2.12)$$

We are only interested in perturbations that will collapse. Assuming that the material inside our region of interest has too little energy to escape, we can write the solution to (2.12) parametrically as

$$r = A(1 - \cos \theta) \quad t = B(\theta - \sin \theta) \quad (2.13)$$

with $B = \sqrt{A^3/(GM)}$. The average density inside the sphere is $\rho_s = [1 + \delta(t)]\bar{\rho}(t)$, with the average density of the Friedmann-Robertson-Walker Model of a matter dominated universe $\bar{\rho}(t) = (6\pi G t^2)^{-1}$ far outside the sphere. Here, the over-density δ is only a function of time, because the sphere is assumed to be homogeneous. The small initial perturbations grow with time

$$\delta(t) = \frac{\rho_s(t)}{\bar{\rho}(t)} - 1 = \frac{9}{2} \frac{(\theta - \sin \theta)^2}{(1 - \cos \theta)^3} - 1 \quad (2.14)$$

slowing the expansion in over-dense regions until their expansion stops at $r(\theta = \pi) =$

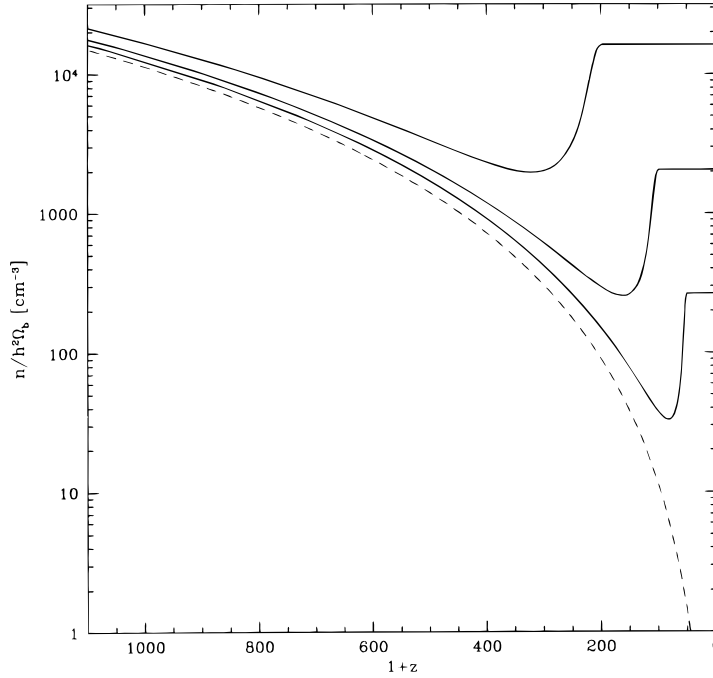


Figure 2.3: Density evolution during structure formation in the universe [15]. Overdense regions expand slower than the average expansion of the universe until they reach a point at $\delta_{\text{turn}} \approx 4.5$ where the expansion stops and the region collapses due to gravitational attraction. The region then virialises and finally settles at a virial plateau value of $\delta_{\text{vir}} \approx 180$. The dashed line is the mean matter density of the universe $\bar{\rho}(t)$ and the solid lines are the local overdensities of different sizes.

2A with an over-density at turnaround of

$$\delta_{\text{turn}} = \delta(\theta = \pi) = (3\pi/4)^2 - 1 \approx 4.55 \quad (2.15)$$

at a turnaround time $t_{\text{turn}} = \pi B$ [14, p. 215ff]. After the over-dense region has decoupled from the expansion of the universe, the system collapses due to internal gravitational attraction and, in this model, would contract to a single point at $t = 2t_{\text{turn}}$. In fact, however, even a collisionless system would not contract to a single point but relax into equilibrium at $t_{\text{vir}} = 2t_{\text{turn}}$ with an over-density of $\delta_{\text{vir}} = 18\pi^2 \approx 178$ [15] and thereby decouple from the expansion of the universe. This process is depicted in Fig. 2.3.

Assuming a collisionless collapse, the relaxation is governed by two processes – phase mixing and violent relaxation [13, p. 379ff]. Phase mixing describes the process in which particles oscillate around the minimum of the gravitational potential, whereas particles with high energies oscillate slowest because they travel the longest distance

while particles with low energies oscillate faster. This implies that an initially compact group of phase space points gets smeared out and after several oscillations the phase space density is approaching uniformity, while remaining confined to the area between the curves of minimum and maximum energy. While phase mixing changes the phase space density of the gas on a macroscopic level, it does not change the energy of a microscopic particle because the gravitational potential the particles are moving in is constant. In reality, however, the gravitational potential changes with time since the particles, which are the sources of the potential are constantly moving. Therefore, the energy of a given particle is not conserved anymore. Particles can gain or lose energy (even without collisions) leading them to relax homogeneously in a spherical volume. This volume is called a “halo” and is the equilibrium state for a gravitationally interacting collisionless gas cloud.

The combination of phase mixing and violent relaxation is called virialization since the relaxed halo satisfies the virial theorem $\langle E_{\text{kin}} \rangle = -1/2 \langle E_{\text{pot}} \rangle$. The potential energy of a spherical system is given by

$$E_{\text{pot}} = -4\pi G \int_0^\infty dr r \rho(r) M(r) \quad (2.16)$$

which, for a homogeneous sphere with $M(r) = 4\pi\rho r^3/3$, is

$$E_{\text{pot}} = -\frac{16\pi^2}{3} G \rho^2 \int_0^r dr' (r')^4 = -\frac{16}{15} \pi^2 G \rho^2 r^5 = -\frac{3}{5} \frac{GM^2}{r}. \quad (2.17)$$

At the turnaround point the kinetic energy is zero, therefore the total energy of this sphere is

$$E = -\frac{3}{5} \frac{GM^2}{r_{\text{turn}}} \quad (2.18)$$

where r_{turn} is the radius at maximum expansion. Since a collisionless system cannot dissipate its energy during the collapse, the gravitational potential energy has to be converted into kinetic energy of the particles involved in the collapse during relaxation. The final object, therefore, has a potential energy of

$$E_{\text{pot}} = -\frac{3}{5} \frac{GM^2}{r_{\text{vir}}} \quad (2.19)$$

and, applying the virial theorem, a kinetic energy

$$E_{\text{kin}} = \frac{3}{10} \frac{GM^2}{r_{\text{vir}}}. \quad (2.20)$$

From the virial theorem we can also deduce that $r_{\text{vir}} = r_{\text{turn}}/2$. With the average kinetic energy of a classical gas with a Maxwell-Boltzmann velocity distribution $\langle E_{\text{kin}} \rangle = 3T/2$, we find that

$$\frac{3}{2}T_{\text{vir}} = \frac{3}{10} \frac{GMm_{\chi}}{r_{\text{vir}}} = \frac{m_{\chi}v_{\text{vir}}^2}{2}, \quad (2.21)$$

where M is the mass of the whole system, m_{χ} the mass of one particle and r_{vir} , v_{vir} are the virial radius and velocity respectively.

Including collisions without dissipation, yields a qualitatively similar result. However, if the gas can radiate energy it will form a “disk”, because it will occupy the state of lowest energy while conserving angular momentum. For a distribution of angular momentum along an axis, the lowest energy state of the system is a flat disk perpendicular to that axis [13, p. 456].

An important property of a spherical matter distribution is its circular velocity

$$v_{\text{circ}}(r) = \sqrt{\frac{GM(r)}{r}} \quad (2.22)$$

which can be obtained by setting the centripetal force equal to the gravitational force of a particle with negligible mass in a circular orbit and which for $r = 5r_{\text{vir}}/3$ is equal to the virial velocity. Since the circular velocity of baryonic matter is often easily accessible to observation and due to its relation to an object’s mass, the circular velocity of galactic structures is often used as a synonym for their mass. Very small dwarf galaxies have a typical circular velocity of $v_{\text{circ}} \sim 10$ km/s, larger galaxies have $v_{\text{circ}} \sim 100$ km/s and clusters of galaxies can have circular velocities of $v_{\text{circ}} \sim 1000$ km/s.

One can see in Fig. 2.3 that the density of a halo after virialization depends on the time when it was formed. Since the density of a self-gravitating object is related to its total mass, one can already guess that structures with similar mass will form at similar times. Press and Schechter developed a formalism using Gaussian random fields to relate the number density of collapsed objects with a certain mass M to the time when

they are formed [14, p. 327ff]. They start with a smoothed density field

$$\delta_s(\vec{x}, R) = \int d^3x' \delta_0(\vec{x}') W(\vec{x} + \vec{x}', R) \quad (2.23)$$

where $W(\vec{x} + \vec{x}', R)$ is a window function of radius R corresponding to the mass $M = 4\pi\bar{\rho}R^3/3$. Expanding (2.14), we get $\delta(t) = 3/20 \theta^2 + \mathcal{O}(\theta^4)$ and for the initial condition $\delta_i \ll 1$ we can neglect higher orders and write $\delta_i = 3/20 \theta_i^2$. Similarly, (2.13) yields $A = 2r_i/\theta_i = 3r_i/(10\delta_i)$. Thus, we find for the collapse time t_{vir}

$$t_{\text{vir}} = 2t_{\text{turn}} = 2\pi\sqrt{A^3/(GM)} \approx 2.19 \frac{t_i}{\delta_i^{3/2}} \quad (2.24)$$

yielding, as a requirement for a collapse to commence, that the initial over-density is at least

$$\delta_c(t_i, t) \approx 1.69 \left(\frac{t_i}{t_{\text{vir}}} \right)^{2/3} \quad (2.25)$$

which we call the critical over-density. The Press-Schechter formalism assumes that the probability that $\delta > \delta_c$ is given by integrating the Gaussian distribution of fields

$$P(\delta_s > \delta_c) = \frac{1}{\sqrt{2\pi}\sigma(M)} \int_{\delta_c}^{\infty} e^{-\frac{\delta_s^2}{2\sigma^2(M)}} d\delta_s. \quad (2.26)$$

where

$$\sigma^2(M) = \langle \delta_s^2 \rangle = \frac{1}{\sqrt{2\pi}} \int_0^{\infty} P(k) \tilde{W}^2(\vec{k}, R) k^2 dk \quad (2.27)$$

is the mass variance of the density field, with $P(k)$ its power spectrum and $\tilde{W}(\vec{k}, R)$ the Fourier transform of the window function. According to (2.26), the probability that $\delta > \delta_c$ is given by the mass fraction F of collapsed objects with mass greater than M . The problem with (2.26) is that the probability is not normalized to 1 for $M \rightarrow 0$ which would mean that only a fraction of the universe is part of collapsed objects of any mass. Press and Schechter solved this problem by introducing a factor 2, *i.e.*,

$$F(> M) = 2P(> \delta_c). \quad (2.28)$$

This results in a number density of collapsed objects with masses in the range $[M, M +$

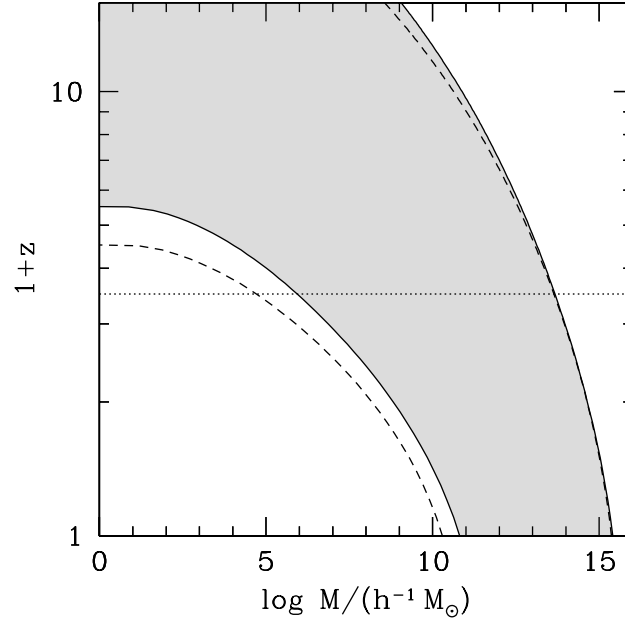


Figure 2.4: Halo mass range as a function of the redshift presented in Ref. [16]. The gray area was obtained by simulations based on a flat, Λ CDM cosmology, fitting on the numerical results a Press-Schechter-like mass function of the kind (2.29d). One can see that small structures are more likely to have formed in the early stages of the universe while larger structures are more likely to have formed in the universe's later history.

$dM]$ given by the Press-Schechter mass function

$$n(M, t)dM = \frac{\bar{\rho}}{M} \frac{\partial F(> M)}{\partial M} dM \quad (2.29a)$$

$$= 2 \frac{\bar{\rho}}{M} \frac{\partial P(> \delta_c)}{\partial \sigma} \left| \frac{d\sigma}{dM} \right| dM \quad (2.29b)$$

$$= \sqrt{\frac{2}{\pi}} \frac{\bar{\rho}}{M^2} \frac{\delta_c}{\sigma} e^{-\frac{\delta_c^2}{2\sigma^2}} \left| \frac{d \ln \sigma}{d \ln M} \right| dM \quad (2.29c)$$

$$= \frac{\bar{\rho}}{M^2} f_{\text{PS}}(\nu) \left| \frac{d \ln \nu}{d \ln M} \right| dM \quad (2.29d)$$

where in the last step we have defined the variable $\nu = \delta_c/\sigma(M)$ and the multiplicity function $f_{\text{PS}} = \sqrt{2/\pi} \nu \exp(-\nu^2/2)$. The Press-Schechter mass function shows how structures form in a hierarchical model. In Fig. 2.4 one can see the range of halo masses M forming at a given redshift z [16]. In this model, only small structures can form in the early universe while large structures have formed only recently. We will use this figure in Chap. 4 to guide the eye in the presentation of our results.

2.4 Dark Matter Density Distribution in the Universe

As we have seen in the previous section, during the structure evolution of the universe small over- and under-densities are amplified, entering a non-linear regime which cannot be calculated analytically. Therefore, numerical N-body simulations [17] are used to predict the evolution of structures in the universe.

Since dark matter has to be gravitationally interacting and since its abundance in the universe is about five times larger than the abundance of ordinary matter, it is intuitive that dark matter plays an essential role in structure evolution. Simulations of the evolution of the universe containing CDM, starting from a homogeneous and isotropic universe and using simple Newtonian mechanics provide a very good fit to observations on large scales ($\gg 1$ Mpc). However, on galactic and sub-galactic scales (\leq few Mpc), simulations based on Λ CDM lead to differences compared to observations [9]. The differences between Λ CDM N-body simulation and observation on small scales are known as the three big unsolved problems of structure formation in the universe. They all involve the density distribution of dark matter halos, which are embedded in structures of ordinary matter and are observed via gravitational effects on the latter. The unsolved problems came to be known as the “missing satellite problem”, the “too big to fail problem” and the “cusp vs. core problem” and shall be briefly explained in the following.

Missing Satellite

The missing satellite problem [18, 19, 20] refers to the difference in the number of predicted CDM sub-halos obtained by N-body simulations compared to the number of satellite galaxies (*i.e.* small galaxies orbiting larger ones due to gravitational attraction) observed in our local group of galaxies. As CDM halos are expected to be hosted by structures of ordinary matter, these numbers should coincide. Simulations, however, predict ~ 5 times more satellite galaxies than observed with a circular velocity $v_{\text{circ}} \approx 10 - 20$ km/s.

A possible solution to explain this discrepancy is that said galaxies are small and faint and therefore have, up to now, evaded detection. This means that in building larger and better telescopes it should be possible to find the missing galaxies. Other theories, *e.g.* baryon feedback [21], assume processes that suppress gas accretion (*i.e.* structure formation in the standard model sector) in these dark matter halos, keeping them free from ordinary matter and therefore impossible to discover via telescopes.

Too Big to Fail

In contrast to the missing satellite problem, the too big to fail problem [22, 23] states that the galaxies are too faint to be detected by pointing out that some of the galaxies predicted by N-body simulations are so massive, that it is very unlikely that they do not host any visible stars. Observations show that the Milky Way has a few satellite galaxies, as does Andromeda which is the second major galaxy in our local group. But comparing the masses of these galaxies and the sub-halos from N-body simulations, leads to a discrepancy, *i.e.*, the mass of the sub-halos from simulation exceeds the mass of the observed satellite galaxies by a factor four to five.

Since simulations assume CDM which is only gravitationally interacting, it is possible that these sub-halos are governed by interactions in the dark sector which are not taken into account by N-body simulations. We will come back to this scenario in the discussion of the cusp vs. core problem.

Cusp vs. Core

The cusp vs. core problem [8, 24] addresses the fact that observations seem to indicate an approximately constant dark matter density profile $\rho(r) = \text{const}$ in the inner parts of galaxies (core), while simulations indicate a steep power-law-like (cuspy) behavior $\rho(r) \propto r^{-\alpha}$ with $\alpha > 0$.

From (2.1) one can see that a halo with constant ρ leads to a rotation curve with a linear increase in r whereas a cuspy halo with $\rho(r) \propto r^{-1}$ leads to a rotation curve increasing with $r^{1/2}$. Combining measurements of rotation curves to obtain the overall matter density $\rho(r) = \rho_{DM}(r) + \rho_{SM}(r)$ of galactic structures with absolute brightness measurements to obtain the luminous (or ordinary) matter content $\rho_{SM}(r)$, one can extract the DM density profile for the observed structure. In Fig. 2.5 one can see the measurement of the rotation curve for the galaxy F568-3 which fits a core-like density distribution and is in disagreement with a cuspy behavior.

To summarize, the cusp vs. core problem refers to the fact that Λ CDM simulations predict a larger amount of dark matter in the center of galaxies than observed in experiments. One intuitive solution to this problem would be to introduce an interaction between the CDM particles, that allows for a heat transfer from the outer regions to the center and therefore can reproduce a more core-like behavior [9, 25, 26]. In order for this mechanism to resolve the conflict, Spergel and Steinhardt [9] assume for their CDM self interaction a “large scattering cross-section but negligible annihilation or dis-

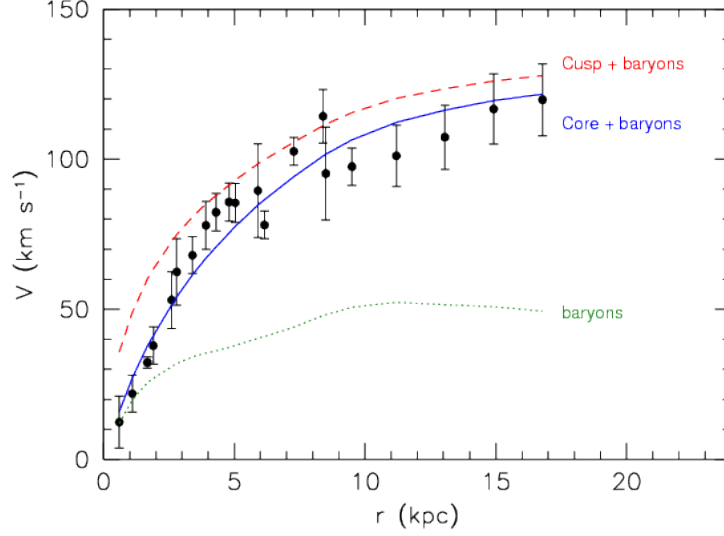


Figure 2.5: The measured rotation curve of F568-3 (points) compared to model fits assuming a cored dark matter halo (blue solid curve) or a cuspy dark matter halo (red dashed curve). The dotted green curve shows the contribution of baryons (stars+gas) to the rotation curve, which is included in both model fits. One can see that for small r a cored dark matter density profile yields a better fit to the data. [8]

sipation”. In the following chapters we will focus on various models of self interacting dark matter (SIDM) and explore how bremsstrahlung contributes to energy dissipation in these models.

2.5 Particle Dark Matter

Even though today we know to tremendous precision how much DM is contained in our universe and how it behaves in the context of gravity, we know almost nothing about its particle character. The mass of dark matter particles as well as their self-interaction and their interaction with ordinary matter is strongly model dependent.

Assuming that there is an interaction between dark and ordinary matter, which is the key prerequisite for being able to detect dark matter, we can classify different dark matter scenarios by their interaction rate $\Gamma_{\text{int}}^{\text{DM} \leftrightarrow \text{SM}} = n \langle \sigma_A v \rangle$ with ordinary matter³ (see, *e.g.*, Ref. [12, p. 115ff]). In the relativistic regime ($T \gg m_{\text{DM}}$), the number density $n \propto T^3$ and $\Gamma_{\text{int}}^{\text{DM} \leftrightarrow \text{SM}}$ will vary as some power of T , while in the non-relativistic regime ($T \lesssim m_{\text{DM}}$), $n \propto (mT)^{3/2} \exp(-m/T)$ such that $\Gamma_{\text{int}}^{\text{DM} \leftrightarrow \text{SM}}$ decreases exponentially. In the early universe when $T \gg m_{\text{DM}}$, dark matter and ordinary matter are in thermal

³The interaction rate is a function of the equilibrium number density n , and the velocity averaged annihilation cross section into standard model particles $\langle \sigma_A v \rangle$.

equilibrium if

$$\Gamma_{\text{int}}^{\text{DM} \leftrightarrow \text{SM}} \gtrsim H(T) \quad (2.30)$$

where in the context of this discussion the Hubble rate is a function of the average temperature of the universe⁴. We denote this case as the “normal” dark matter scenario where in the early universe the number of dark matter particles is equal to the number of standard model particles

$$\frac{N_{\text{DM}}}{N_{\gamma}} \sim 1 \quad (2.31)$$

which at that point all behave relativistically. At the time during the evolution of the universe when $T \lesssim m_{\text{DM}}$, the dark matter number density decreases because dark matter cannot be thermally produced anymore. All dark matter particles would annihilate into standard model particles as long as $\Gamma_{\text{int}}^{\text{DM} \leftrightarrow \text{SM}} \gtrsim H(T)$. It follows from the model, however, that at some point $\Gamma_{\text{int}}^{\text{DM} \leftrightarrow \text{SM}} < H(T)$, which means that the universe expands faster than it takes two dark matter particles to “find” each other and annihilate, which stabilizes the dark matter density. This process is called thermal freeze out.

A class of dark matter candidates which fall into this category is called *Weakly Interacting Massive Particles* (WIMPs) [1]. In order for the thermal freeze out to produce the right relic density the WIMP mass cannot be too small, *i.e.* $m \gtrsim \text{GeV}$. Particles fulfilling the above criteria are, *e.g.*, the lightest supersymmetric particle such as the neutralino⁵ or the lightest Kaluza-Klein particle of theories with extra dimensions. The interaction in this dark matter scenario is constrained to be in the order of the weak scale. However, it can be mediated by new scalar or vector bosons or dark matter might couple to ordinary matter via a Higgs portal.

In the second dark matter scenario that we want to discuss,

$$\Gamma_{\text{int}}^{\text{DM} \leftrightarrow \text{SM}} \ll H(T) \quad (2.32)$$

for $T \gg m_{\text{DM}}$ which means that dark and ordinary matter are not in thermal equilibrium in the early universe. Assuming that all dark matter particles are produced from

⁴The Hubble rate follows from the first Friedmann equation $3H^2(T) = g_*(T)\pi^2 T^4/(30m_{Pl}^2)$, where $g_*(T)$ are the relativistic degrees of freedom and m_{Pl} is the Planck mass (see Ref. [12]).

⁵The neutralino is a linear combination of the neutral superpartners of the SM gauge bosons and the Higgs bosons, *i.e.* the higgsino, bino and neutral winos.

standard model particles, this implies that

$$\frac{N_{\text{DM}}}{N_\gamma} \ll 1. \quad (2.33)$$

Dark matter candidates in this category are often called *Super Weakly Interacting Massive Particles* (or Super-WIMPs) because their interaction with ordinary matter is very weak. They might even only interact gravitationally. Particles referred to as Super-WIMPs are, *e.g.*, Supersymmetry’s gravitino or a sterile neutrino.

In addition to the above two scenarios, *axions* also represent a viable dark matter candidate [27]. They are postulated by the Peccei-Quinn theory to solve the strong CP-problem in quantum chromodynamics, but to the present day, many dark matter theories have been proposed involving “axion-like” particles in the sense that they are pseudo-scalar bosons which derivatively couple to ordinary matter. They have to be very light ($\lesssim 10^{-2}$ eV) and are expected to be extremely weakly interacting with ordinary matter which implies that they were not in thermal equilibrium in the early universe. For the axion to be a viable dark matter candidate, the axion field has to start out with a non zero initial field value $\phi \neq 0$ and

$$\frac{N_{\text{DM}}}{N_\gamma} \gg 1 \quad (2.34)$$

in the early universe. The field, at first, slowly rolls down the potential because the Hubble rate acts as a friction term in the equations of motion of the axion field, but at some some point the friction term becomes negligible and the field starts oscillating around the minimum of the potential, giving a contribution to the matter density ρ_M .

All the above dark matter candidates are motivated by theories beyond the Standard Model (BSM), like Supersymmetry, models with extra dimensions, the Peccei-Quinn symmetry in the strong CP problem or extensions of the neutrino sector. However, many more dark matter models have been postulated that might or might not be embedded in a larger framework, meaning that dark matter may well be composed of only one kind of particle (boson or fermion) that interacts with the standard model via any kind of new interaction. Since dark matter has not been detected, the only constraints coming from experiments are upper bounds on the interaction strength. We will use this freedom in the next chapter to construct generic models of bosonic and fermionic dark matter to investigate bremsstrahlung in the dark sector, *i.e.*, we will not be interested in the interaction of dark matter with the Standard Model sector

but only in self-interactions in the dark sector.

Dissipation in Self-Interacting Dark Matter Models

The only direct evidence for dark matter, as described in Chap. 2, is of gravitational nature. Various experiments have tried to find direct or indirect evidence for dark matter in detectors by assuming that it interacts weakly with ordinary matter. Measurements of this kind have not found any significant hints for dark matter but have produced constraints on the mass and cross section for interactions of dark matter particles with standard model particles. However, since we can only detect dark matter via ordinary matter, these constraints do not give any restrictions for dark matter self-interactions. Therefore, interactions in the dark sector are only weakly constrained by observations, *e.g.* of the Bullet cluster, and allow for the assumption of a strong self-interaction [9] and possibly for a resolution of the discrepancies between simulation and observation. In order to do so, one needs a large elastic scattering cross section¹ of $\sigma_{el}/m_\chi \sim 1 \text{ cm}^2/\text{g}$ and low dissipation $m_M \gg m_\chi v_\chi^2$, which can be reached with non-relativistic dark matter and a relatively light mediator² since the elastic cross section goes parametrically as $\sigma_{el} \propto \alpha^2 m_\chi^2/m_M^4$ (where m_χ is the dark matter and m_M the mediator mass). A dark matter self-interaction, however, does not only imply scattering of dark matter particles but may also lead to the emission of the (gauge) boson that mediates the interaction (*i.e.* bremsstrahlung) if $m_M \lesssim m_\chi v_\chi^2$. This dissipative process may counteract the formation of a core-like density profile.

In the following, we will introduce various models of dark matter. We discuss the

¹In fact, instead of the full elastic cross section one uses the transport or viscosity cross section, which regularizes the divergences for vanishing mediator mass (see Sec. 3.4).

²Of course, $m_M \gg m_\chi v_\chi^2$ still has to hold. In order for the elastic cross section to scale with m_M^{-4} even the stronger requirement $m_M \gg m_\chi v_\chi$ has to hold.

scattering process of fermionic and scalar CDM χ with a mass $m_\chi \sim \text{GeV}$ and a typical velocity $v_\chi \ll 1$ corresponding to a temperature $T \sim m_\chi v_\chi^2 \lesssim \text{MeV}$. The interaction between the CDM particles is mediated by a light scalar ϕ or vector boson V with a mass which is smaller than the center of mass (CM) energy of the system $m_{\phi,V} < m_\chi v_\chi^2$ for the particle being able to be emitted as bremsstrahlung in the scattering event. We assume the dark matter gas to be dilute or non-degenerate, in order to treat the thermodynamics of the gas semi-classically with a Maxwell-Boltzmann distribution. Furthermore, we assume the coupling strength between the CDM particle and the mediator to be small, $g < 1$, in order to treat the scattering process perturbatively.

3.1 S-Matrix, Cross Section and Energy Loss Rate

In scattering theory, a very important but rather abstract quantity is the S-matrix [see 28, ch.5-6], which relates the ingoing momentum eigenstates to the outgoing ones and therefore encodes all interesting information about how often given initial states $|i\rangle$ produce given final states $|f\rangle$

$$S_{fi} = \langle f | S | i \rangle. \quad (3.1)$$

In a free theory without interactions, the S-matrix is $\mathbb{1}$ because the momentum eigenstates $|i\rangle$ and $|f\rangle$ are the eigenstates of the free theory. We can therefore write

$$S = \mathbb{1} + i(2\pi)^4 \delta^{(4)}(\Sigma p_i - \Sigma p_f) \mathcal{M} \quad (3.2)$$

with the second term describing the deviation from the free theory, where p_i and p_f are the initial and final states' 4-momenta. The squared matrix element which is of great importance in quantum field theory and whose calculation for different dark matter models will be an essential part of this chapter, is given by

$$|\mathcal{M}|^2 = \sum_{\text{spins}} |\langle f | \mathcal{M} | i \rangle|^2. \quad (3.3)$$

For all following calculations, we define $|\mathcal{M}|^2$ as summed over initial and final spins. The squared matrix element itself is not experimentally accessible but can be used to calculate physically measurable quantities. The scattering cross section is calculated

from $|\mathcal{M}|^2$ by integrating over the Lorentz invariant phase space of the final states

$$\prod_{\text{final states } j} \frac{d^3 p_j}{(2\pi)^3} \frac{1}{2E_j} (2\pi)^4 \delta(\Sigma p_i - \Sigma p_f), \quad (3.4)$$

yielding for the process of interest in this thesis, *i.e.* a two body collision with bremsstrahlung ($2 \rightarrow 3$ process)

$$\sigma = \frac{(2\pi)^4 S_f}{(2E_1)(2E_2)|\vec{v}_1 - \vec{v}_2|} \int \prod_{j=3}^4 \frac{d^3 p_j}{(2\pi)^3 2E_j} \int \frac{d^3 q}{(2\pi)^3 2\omega} \frac{1}{g_\chi^2} |\mathcal{M}|^2 \delta^{(4)}(p_1 + p_2 - p_3 - p_4 - q). \quad (3.5)$$

Here, the 4-dimensional delta function assures energy and momentum conservation, indices 1 and 2 correspond to the incident particles, indices 3 and 4 to the final states and ω and \vec{q} are the energy and momentum of the emitted particle. S_f is a symmetry factor for identical particles in the final state, where $S_f = \frac{1}{2}$ for identical particles and $S_f = 1$ otherwise and g_χ accounts for the number of spin states in the initial state which is 2 for fermions and 1 for scalar bosons. The factor g_χ^{-2} in 3.5 therefore accounts for an average over the initial spins since we want to calculate the non-polarized cross section. Note that the factor $|\vec{v}_1 - \vec{v}_2|$ is not Lorentz invariant under boosts in a direction other than the collision axis. Therefore, the expression is only valid for collinear collisions. For an arbitrary frame of reference, the Lorentz invariant quantity is $\sqrt{(p_1 p_2)^2 - m_1^2 m_2^2} / (E_1 E_2) = \sqrt{(\vec{v}_1 - \vec{v}_2)^2 - (\vec{v}_1 \times \vec{v}_2)^2}$.

The physical quantity of interest in our calculation is the energy loss rate (*i.e.* the energy per unit time that is lost by the system due to bremsstrahlung). The energy loss rate is given by the phase space integral

$$\dot{\epsilon} = S(2\pi)^4 \int \prod_{i=1}^4 \frac{d^3 p_i}{(2\pi)^3 2E_i} f(E_1) f(E_2) \int \frac{d^3 q}{(2\pi)^3 2\omega} \omega |\mathcal{M}|^2 \delta^{(4)}(p_1 + p_2 - p_3 - p_4 - q) \quad (3.6)$$

where $S = S_i S_f$ is a symmetry factor for identical particles in the initial and final state, $f(E_i)$ are the distribution functions for the dark matter particles in the initial state. The Pauli blocking factors $[1 - f(E_f)]$ for fermion scattering and enhancing factors $[1 + f(E_f)]$ for boson scattering, which account for the blocking of filled fermionic states and for enhancing filled bosonic states for the final particles, as well as a factor $[1 + f(\omega)]$ for stimulated emission are omitted since we assume that the dark matter

gas is non-degenerate, the occupation number of the emitted particle is small and that it streams freely after emission.

The energy loss rate is connected to the cross section (3.5) in the following way

$$\dot{\epsilon} = \frac{S_i g_\chi^2}{(2\pi)^6} \int d^3 p_1 d^3 p_2 f(E_1) f(E_2) |\vec{v}_1 - \vec{v}_2| \int d\omega \omega \frac{d\sigma}{d\omega} \quad (3.7)$$

where g_χ^2 accounts for the spin degeneracy in the initial states. In the non-relativistic limit, in substituting the integration variables in the phase space integration by dimensionless variables, as demonstrated in App. A.4, one can rewrite (3.6), (3.5) and (3.7) to get

$$\begin{aligned} \dot{\epsilon} &= \frac{S n_\chi^2}{2^7 g_\chi^2} \frac{T^{7/2}}{\pi^{7/2} m^{5/2}} \int_0^\infty du e^{-u} \int_0^u dx \sqrt{u(u-x)} x^2 \int_{-1}^1 dz |\mathcal{M}(u, x, y, z)|^2 \\ &= \frac{4 S_i n_\chi^2 T^{3/2}}{\pi^{1/2} m^{1/2}} \int_0^\infty du u e^{-u} \int_0^\infty dx x \frac{d\sigma}{dx} \end{aligned} \quad (3.8)$$

whereas $u = p_i^2/m_\chi T$ is connected to the center of mass energy, $x = \omega/T$ to the emitted particle's energy, $z = \cos \theta_{fi}$ to the angle between initial and final state momenta and $y = m_M^2/m_\chi T$ to the mediator mass which remains a free parameter in the integration. (For details, see App. A.4).

We will use the energy loss rate to calculate the cooling timescale [29]

$$t_{\text{cool}} = \frac{3n_\chi T}{\dot{\epsilon}}$$

which is the time it takes a gas cloud with particle density n_χ , temperature T and energy loss rate per collision $\dot{\epsilon}$ to cool due to dissipation. The influence of cooling on the gas cloud depends on the ratio of t_{cool} at the virial temperature T_{vir} to the gravitational collapse timescale

$$t_{\text{grav}} = \sqrt{\frac{3\pi}{8m_\chi n_\chi G}}$$

which is the time it takes a gas cloud to contract due to the gravitational attraction and the Hubble time

$$t_0 = H_0^{-1}$$

which is roughly the age of the universe. If $t_{\text{cool}} > t_0$ the energy loss due to dissipation can only have negligible influence on structure formation in the universe since it takes longer than the age of the universe for a gas cloud to cool. If $t_0 > t_{\text{cool}} > t_{\text{grav}}$ cooling can have a significant role in structure formation, *i.e.* it can speed up the collapse of a gas cloud and lead to the formation of disks (see, *e.g.*, [30]). In case that $t_{\text{cool}} < t_{\text{grav}}$ we are entering an extreme regime where all kinetic energy is quickly radiated away and the collapse is dominated by dissipation. We will discuss the effects of dissipation due to bremsstrahlung and do a detailed analysis of different dark matter scenarios in Chap. 4.

3.2 Fermion Scattering

When calculating the scattering of two dark matter fermions, at tree level there are three different channels that contribute to the scattering process (see Fig. 3.1). We label these channels as the direct or t-channel (a, b, \dots), the exchange or u-channel where the two final states are exchanged (a', b', \dots) and the annihilation or s-channel where two particles annihilate and are created again (a'', b'', \dots). In case of a scattering process of two identical particles, the direct and exchange diagrams contribute to the process and in case of a process involving a particle and its anti-particle, the direct and annihilation diagrams contribute. However, if the particles are Majorana fermions (which means that the particle is its own charge conjugate state), all the channels contribute to the scattering process.

If we want to calculate a scattering process with the emission of a boson (*i.e.* bremsstrahlung), the boson can be emitted at any of the four external fermion legs in the Feynman diagram (as can be seen in Fig. 3.1) which yields a total number of 12 diagrams considering all three channels³. The corresponding Feynman amplitudes can be

³The most general model of DM scattering could contain a trilinear self-coupling term of the scalar mediator, *i.e.* $A_\phi \phi^3$ (A_ϕ being a dimensionful coupling constant), which would lead to the possibility of emitting bremsstrahlung from the mediator, as depicted in the following diagram

$$\begin{array}{c}
 p_1 \text{ --- } \text{---} \text{---} p_3 \\
 \quad \quad \quad \uparrow \text{---} k - q \\
 \quad \quad \quad \vdots \text{---} \text{---} q \\
 \quad \quad \quad \uparrow \text{---} k \\
 p_2 \text{ --- } \text{---} \text{---} p_4
 \end{array} ,$$

which contributes in all three channels. However, we neglect these diagrams because the trilinear coupling constant A_ϕ has to be small in order for $\langle \phi \rangle = 0$, rendering the contribution of these diagrams to the squared matrix element negligible (see Fig. 3.2 and the corresponding discussion in the next section).

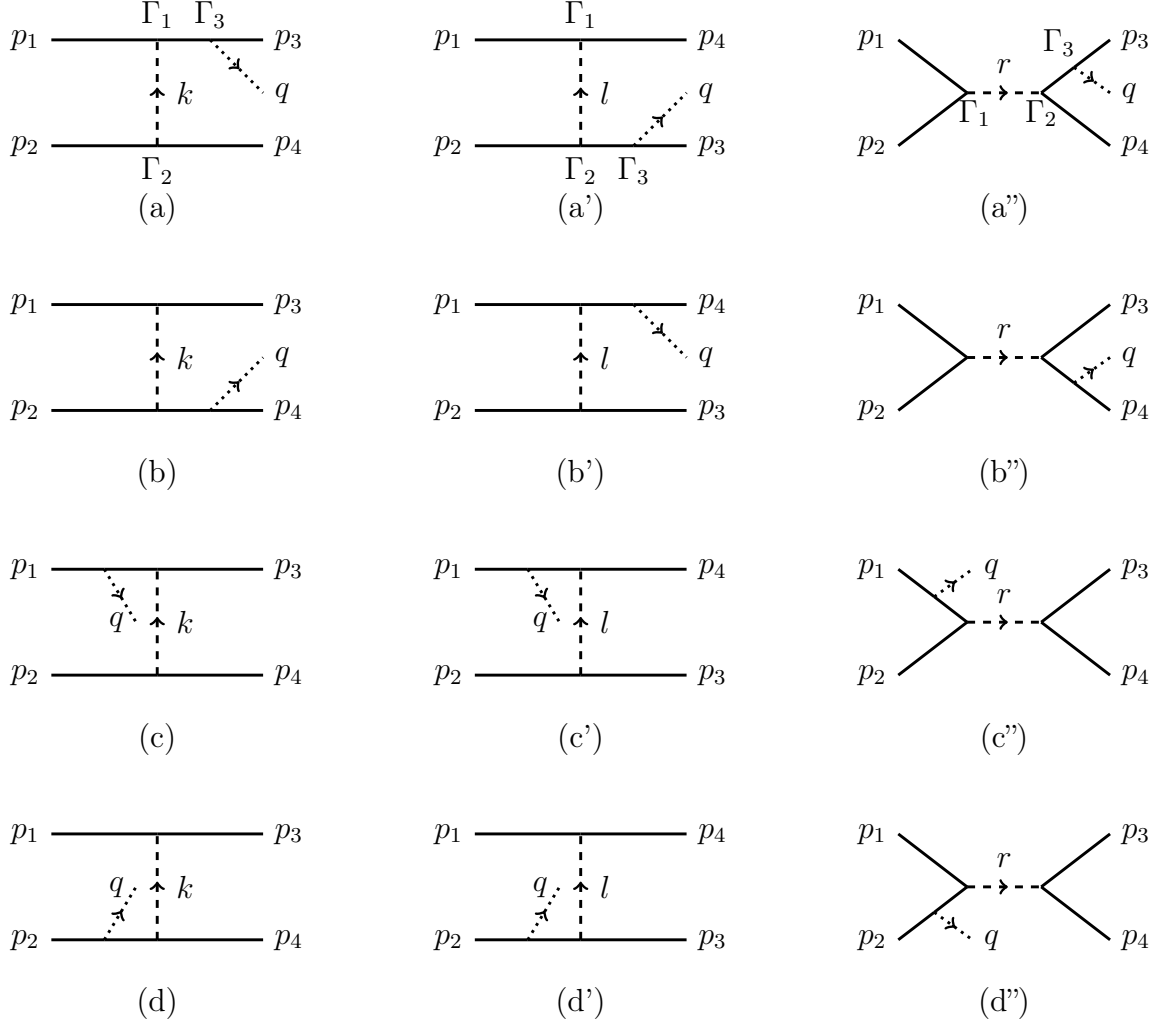


Figure 3.1: 12 tree level diagrams contributing to bremsstrahlung processes in DM scattering. The fermion momentum flows from left to right. For Majorana Fermions, the fermion number flow is arbitrary while for Dirac fermions, the fermion number flows from left to right (particles) or from right to left (anti-particles). The arrows on the boson lines represent the boson momentum flow.

found in App. A.2. The scattering process can be described in terms of the squared matrix element as the square of a coherent sum of the Feynman amplitudes

$$\chi\chi \rightarrow \chi\chi\phi : |\mathcal{M}|^2 = |\mathcal{A} + \mathcal{B} + \mathcal{C} + \mathcal{D} + \mathcal{A}' + \mathcal{B}' + \mathcal{C}' + \mathcal{D}'|^2$$

$$\chi\bar{\chi} \rightarrow \chi\bar{\chi}\phi : |\mathcal{M}|^2 = |\mathcal{A} + \mathcal{B} + \mathcal{C} + \mathcal{D} + \mathcal{A}'' + \mathcal{B}'' + \mathcal{C}'' + \mathcal{D}''|^2$$

$$\tilde{\chi}\tilde{\chi} \rightarrow \tilde{\chi}\tilde{\chi}\phi : |\mathcal{M}|^2 = |\mathcal{A} + \mathcal{B} + \mathcal{C} + \mathcal{D} + \mathcal{A}' + \mathcal{B}' + \mathcal{C}' + \mathcal{D}' + \mathcal{A}'' + \mathcal{B}'' + \mathcal{C}'' + \mathcal{D}''|^2$$

where χ is a Dirac particle, $\bar{\chi}$ is a Dirac anti-particle and $\tilde{\chi}$ is a Majorana particle⁴. This yields a total number 64 squared amplitudes (144 for Majorana fermions) that have to be evaluated for the calculation of the squared matrix element. In order to make the calculation tractable, we use a power counting scheme described in App. A.3 on the basis of the emission of scalar, which will be used in all following calculations. Since in our calculation we are only interested in unpolarized quantities, we define $|\mathcal{M}|^2$ as summed over initial and final spins.

3.2.1 Yukawa Interaction

The Lagrangian for a Dirac fermion χ and a real scalar boson ϕ is given by

$$\mathcal{L} = i\bar{\chi}\not{\partial}\chi - m_\chi\bar{\chi}\chi \quad (\text{free fermion}) \quad (3.9a)$$

$$+ \frac{1}{2}[(\partial_\mu\phi)^2 - m_\phi^2\phi^2] \quad (\text{free scalar}) \quad (3.9b)$$

$$- \frac{1}{3!}A_\phi\phi^3 - \frac{1}{4!}\lambda_\phi\phi^4 \quad (\text{scalar potential}) \quad (3.9c)$$

$$- g_\phi\phi\bar{\chi}\chi \quad (\text{interaction}) \quad (3.9d)$$

where χ is the spinor describing the DM fermion, ϕ the real scalar field describing the mediator and the emitted particle and g_ϕ is the real valued coupling between fermions and mediator, which we assume to be small to justify restricting our calculations to the tree level (as higher order corrections imply higher powers of g_ϕ).

The scalar potential is a polynomial of degree 4, consisting of the ϕ^2 , ϕ^3 and ϕ^4 terms. Imposing that the potential be bounded from below, implies that $\lambda > 0$. Assuming that ϕ is a physical field and thus $m_\phi^2 > 0$, yields a potential with two minima at most, one at $\phi = 0$ and the other depending on the couplings (see Fig. 3.2). Since we do not want ϕ to gain a non-zero vacuum expectation value, we have to impose $A_\phi < \frac{1}{18}m_\phi\sqrt{\lambda}$

⁴If not stated otherwise χ will denote a fermion with spin 1/2 in this section. In order to emphasise this fact, we will use the subscript F for fermion at points where it might be unclear.

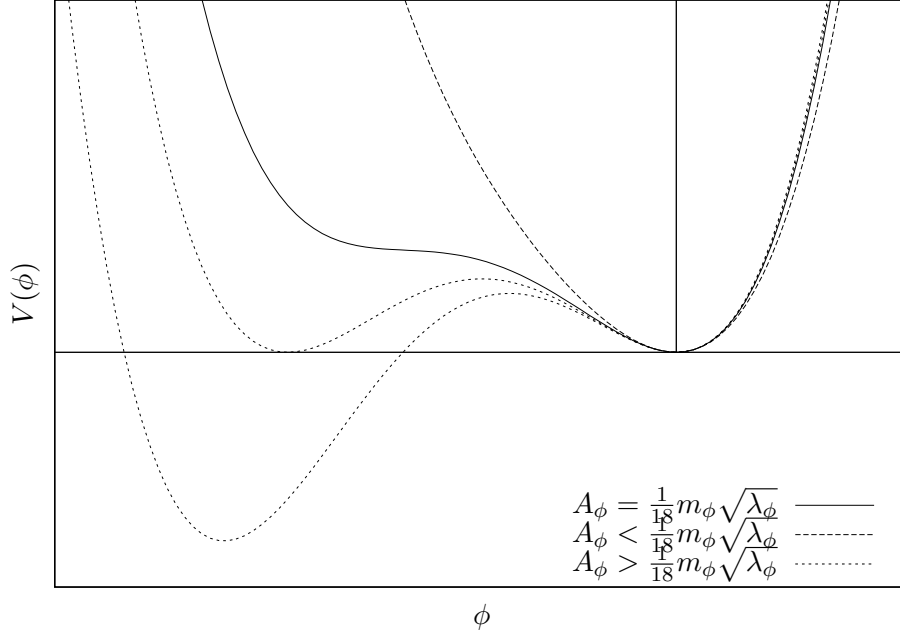


Figure 3.2: Potential of ϕ for several values of the couplings A_ϕ , λ_ϕ and mass m_ϕ showing how ϕ can gain a vacuum expectation value.

in order for the potential to have only one minimum. Since we assume $m_\phi \sim m_\chi v^2$ in order for ϕ to be produced as bremsstrahlung, $A_\phi/m_\chi \lesssim 10^{-6}$ and we can neglect diagrams containing A_ϕ compared to the ones only containing g_ϕ .

Particle-Particle Scattering $\chi_F \chi_F \rightarrow \chi_F \chi_F \phi$

For particle-particle scattering we have to consider diagrams (a)-(d) and (a')-(d') in Fig. 3.1. Assuming that the fermions are non-relativistic, *i.e.*, $v \ll 1$, we find that the squared matrix element summed over initial and final spins is

$$|\mathcal{M}|^2 = \frac{256}{9} \frac{g_\phi^6}{\omega^2} |\vec{k}|^2 |\vec{l}|^2 \left[1 + \frac{m_{\phi'}}{\omega} + 2 \frac{m_{\phi'}^2}{\omega^2} + 3(\hat{k} \cdot \hat{l})^2 \left(1 + \frac{3}{2} \frac{m_{\phi'}}{\omega} + \frac{1}{2} \frac{m_{\phi'}^2}{\omega^2} \right) \right] \times \left[\frac{1}{(|\vec{k}|^2 + m_\phi^2)^2} + \frac{1}{(|\vec{l}|^2 + m_\phi^2)^2} - \frac{1}{(|\vec{k}|^2 + m_\phi^2)(|\vec{l}|^2 + m_\phi^2)} \right] \quad (3.10)$$

where we differentiate between the mediator mass m_ϕ and the emitted particle's mass $m_{\phi'}$, which, in principle, could be two different particles. Furthermore, we have applied a power counting scheme in the collision velocity for $v_\chi \ll 1$ where we assume that the mass of the emitted particle is small, *i.e.* $m_{\phi'} \lesssim m_\chi v_\chi^2$ in order for it to be produced in the collision. Equation (3.10) is the result to leading order in v_χ which reduces the

full expression for $|\mathcal{M}|^2$ to a tractable form.

Assuming that the mass of the emitted particle $m_{\phi'} \ll m_\chi v_\chi^2$, we neglect the terms containing $m_{\phi'}$ but (for now) still keep the mediator mass m_ϕ in the denominator, yielding

$$|\mathcal{M}|^2 = \frac{256}{9} \frac{g_\phi^6}{\omega^2} |\vec{k}|^2 |\vec{l}|^2 \left[1 + 3(\hat{k} \cdot \hat{l})^2 \right] \times \left[\frac{1}{(|\vec{k}|^2 + m_\phi^2)^2} + \frac{1}{(|\vec{l}|^2 + m_\phi^2)^2} - \frac{1}{(|\vec{k}|^2 + m_\phi^2)(|\vec{l}|^2 + m_\phi^2)} \right]. \quad (3.11)$$

The detailed calculation with explanation of all approximations can be found in App. A.3. In terms of the dimensionless variables defined in App. A.4, one can rewrite the matrix element as

$$|\mathcal{M}|^2 = \frac{1024}{9} \frac{g_\phi^6}{T^2} \frac{x^2 + u(u-x) + uz^2(x-u)}{x^2} \left[\left(2u - x + y - 2z\sqrt{u(u-x)} \right)^{-2} + \left(2u - x + y + 2z\sqrt{u(u-x)} \right)^{-2} - \left((2u - x + y)^2 - 4z^2u(u-x) \right)^{-1} \right] \quad (3.12)$$

where the first second and third term in (3.11) corresponds to the first second and third term in (3.12).

We can use the squared matrix element to calculate the cross section in terms of the dimensionless variables defined in App. A.3, yielding

$$\sigma = \frac{1}{36} \frac{g_\phi^6}{m_\chi^2 \pi^3} \int_0^u dx \frac{1}{x} \left[S_{sq}(u, x, y) + S_{log}(u, x, y) \right] \quad (3.13)$$

with

$$S_{sq} = \left(\frac{4x^2}{4uy + (x-y)^2} - \frac{5}{2} \right) \sqrt{1 - \frac{x}{u}} \quad (3.14a)$$

$$S_{log} = \frac{1}{8u} \frac{16u^2 + x^2 + 5y^2 + 20uy - 16ux - 10xy}{2u - x + y} \ln \left[\frac{2u - x + y + 2\sqrt{u(u+x)}}{2u - x + y - 2\sqrt{u(u+x)}} \right] \quad (3.14b)$$

where we have split up $d\sigma/dx$ into a term proportional to $\sqrt{1 - x/u}$, which gives a measure of the amount of energy passed on to the scalar, and a logarithmic term, where the argument of the logarithm is a ratio of the minimum over the maximum momentum

transfer between the fermions for a given center of mass energy. The factor $1/x$ in (3.13) leads to a IR divergence of the cross section for a massless scalar in analogy to the IR divergence due to photon bremsstrahlung in quantum electrodynamics (QED). For the emission of a massive scalar, however, the lower boundary of the integration in (3.13) is finite, *i.e.* $m_{\phi'}/T$, which regularizes the cross section.

For the calculation of the energy loss rate, the integration over the emitted particle's dimensionless energy x , is weighted by a factor x , regularizing the integral even for $m_{\phi'} = 0$. The energy loss rate can be written in terms of S_{sq} and S_{log} as

$$\dot{\epsilon} = \frac{1}{18} \frac{g_\phi^6 n_\chi^2 T^{3/2}}{\pi^{7/2} m_\chi^{5/2}} \int_0^\infty du u e^{-u} \int_0^u dx \left[S_{sq}(u, x, y) + S_{log}(u, x, y) \right]. \quad (3.15)$$

For a massless mediator, $m_\phi \rightarrow 0$ ($y \rightarrow 0$) and (3.15) becomes analytic yielding a simple expression for the energy loss rate

$$\chi_F \chi_F \rightarrow \chi_F \chi_F \phi : \quad \dot{\epsilon} = \frac{188 - 9\pi^2}{216} \frac{g_\phi^6 n_\chi^2}{\pi^{7/2} m_\chi^{5/2}} T^{3/2}. \quad (3.16)$$

For a finite mass of the mediator and/or emitted particle, the energy loss rate cannot be calculated analytically anymore. The effects of finite masses can be seen in Fig. 3.3. The energy loss rate rapidly drops to zero when the mass of the emitted particle reaches the average kinetic energy in collisions $m_\chi \langle v_\chi^2 \rangle = 3T$ because the particle can only be produced on-shell if the energy for its mass $m_{\phi'}$ can be drawn from the kinetic energy of the system. For increasing mediator mass, the energy loss rate drops as m_ϕ^{-4} which only shows its effect when $m_\phi \gtrsim |\vec{k}| \sim m_\chi v_\chi$. Since the mediator particle is off-shell, it can still be exchanged even if its mass exceeds the kinetic energy of the system and therefore the suppression of the energy loss rate occurs for higher m_ϕ .

Particle-Antiparticle Scattering $\chi_F \bar{\chi}_F \rightarrow \chi_F \bar{\chi}_F \phi$

For particle-antiparticle scattering we have to consider diagrams (a)-(d) and (a'')-(d'') in Fig. 3.1. We find that the annihilation diagrams only give contributions in higher orders of velocity and the squared matrix element is dominated by the direct channel, which yields the same result as the direct channel for particle-particle scattering

$$|\mathcal{M}|^2 = \frac{256}{9} \frac{g_\phi^6}{\omega^2} |\vec{k}|^2 |\vec{l}|^2 \frac{1 + 3(\hat{k} \cdot \hat{l})^2}{(|\vec{k}|^2 + m_\phi^2)^2} \quad (3.17)$$

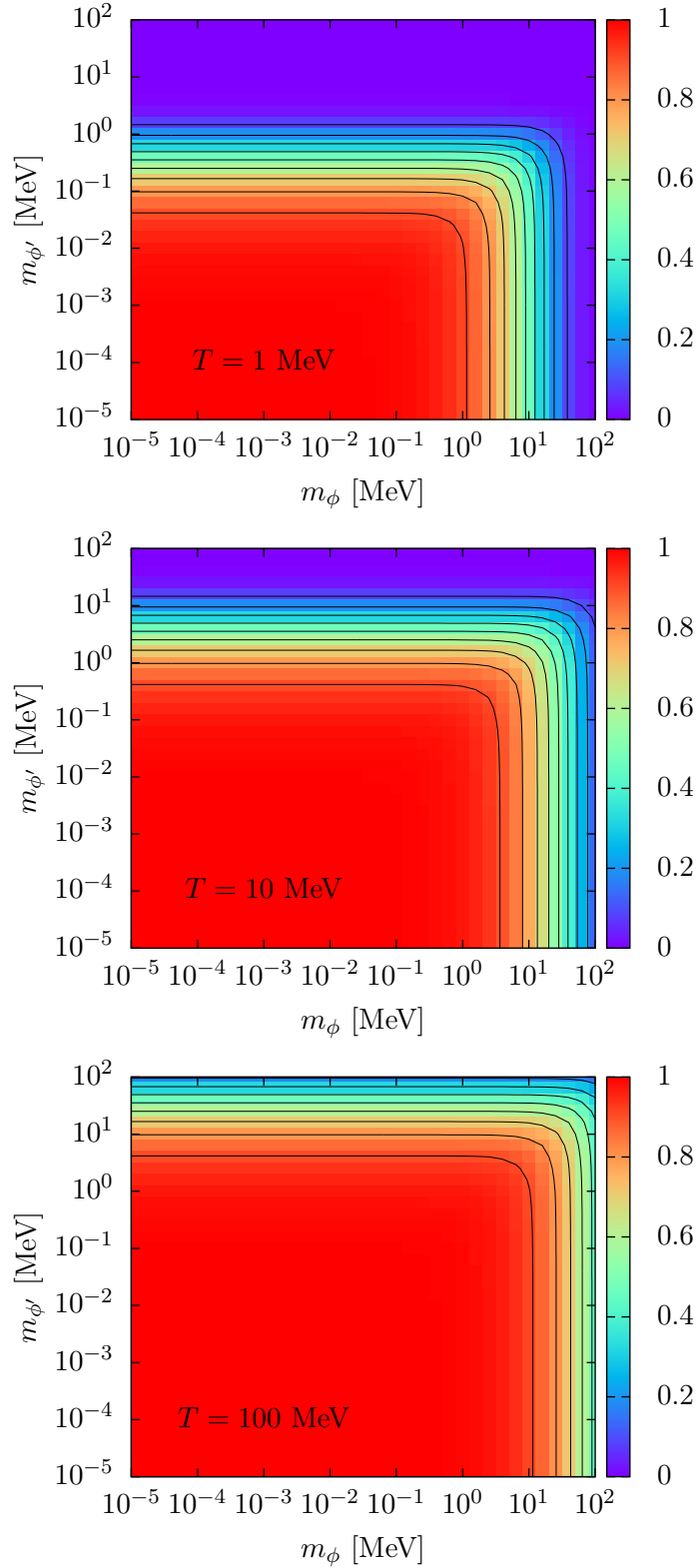


Figure 3.3: $\dot{\epsilon}/\dot{\epsilon}_0$ for $T = 1, 10, 100$ MeV (from top to bottom) for a finite mass of the mediator and emitted particle on the energy loss rate for $m_\chi = 1$ GeV, where $\dot{\epsilon}_0$ corresponds to the energy loss rate for $m_\phi = m_{\phi'} = 0$. It shows, that the energy loss rate drops faster with increasing mass of the emitted particle than it does with increasing mass of the mediator.

where we have already neglected the mass $m_{\phi'}$ of the emitted particle in analogy to (3.11). The full form containing $m_{\phi'}$ can be extracted from (3.10). For the cross section and energy loss rate, we get

$$\sigma = \frac{1}{18} \frac{g_\phi^6}{m_\chi^2 \pi^3} \int_0^u dx \frac{1}{x} \left[S_{sq}(u, x, y) + S_{log}(u, x, y) \right] \quad (3.18)$$

$$\dot{\epsilon} = \frac{2}{9} \frac{g_\phi^6 n_\chi^2 T^{3/2}}{\pi^{7/2} m_\chi^{5/2}} \int_0^\infty du u e^{-u} \left[S_{sq}(u, x, y) + S_{log}(u, x, y) \right] \quad (3.19)$$

with

$$S_{sq} = \left(\frac{2x^2}{4uy + (x-y)^2} - 1 \right) \sqrt{1 - \frac{x}{u}} \quad (3.20a)$$

$$S_{log} = \frac{1}{4u} (2u - x + y) \ln \left[\frac{2u - x + y + 2\sqrt{u(u+x)}}{2u - x + y - 2\sqrt{u(u+x)}} \right]. \quad (3.20b)$$

For a massless mediator, $y \rightarrow 0$ and we get for the energy loss rate

$$\chi_F \bar{\chi}_F \rightarrow \chi_F \bar{\chi}_F \phi : \quad \dot{\epsilon} = \frac{28}{27} \frac{g_\phi^6 n_\chi^2}{\pi^{7/2} m_\chi^{5/2}} T^{3/2}. \quad (3.21)$$

Majorana Particle Scattering $\tilde{\chi}_F \tilde{\chi}_F \rightarrow \tilde{\chi}_F \tilde{\chi}_F \phi$

For Majorana particle scattering we have to consider all diagrams in Fig. 3.1. For a Majorana field $\tilde{\chi}$ with the property $\tilde{\chi}^\dagger \gamma^0 = \tilde{\chi}^T \mathcal{C}$ we get the Lagrangian

$$\mathcal{L} = \frac{i}{2} \tilde{\chi}^T \mathcal{C} \not{\partial} \tilde{\chi} - \frac{1}{2} m_\chi \tilde{\chi}^T \mathcal{C} \tilde{\chi} \quad (\text{free fermion}) \quad (3.22a)$$

$$+ \frac{1}{2} \left[(\partial_\mu \phi)^2 - m^2 \phi^2 + (\partial_\mu \varphi)^2 - m^2 \varphi^2 \right] \quad (\text{free scalar}) \quad (3.22b)$$

$$- \frac{1}{2} g_\phi \phi \tilde{\chi}^T \mathcal{C} \tilde{\chi} - \frac{1}{2} g_\varphi \varphi \tilde{\chi}^T \mathcal{C} \tilde{\chi}. \quad (\text{interaction}) \quad (3.22c)$$

Calculating the Feynman rules for the interaction term of this Lagrangian following [31] (as demonstrated in App. A.2) one realizes that the factors 1/2 in front of the interaction terms are canceled by a factor 2 arising from an increased number of possible Wick contractions in comparison to Dirac fields, yielding in our case the same Feynman amplitudes for Dirac and Majorana fermions. Since the terms involving annihilation diagrams are suppressed by a factor $k^2/r^2 = \mathcal{O}(v^2)$, the leading order contribution of Majorana particle scattering (*i.e.* $\chi = \bar{\chi}$) yields the same result as Dirac particle-

particle scattering.

3.2.2 Gauge Interaction

The Lagrangian for fermionic DM χ with a real vector boson V^μ is given by the gauge coupling $D_\mu = \partial_\mu - ig_V V_\mu$, yielding

$$\mathcal{L} = i\bar{\chi}\not{\partial}\chi - m_\chi\bar{\chi}\chi \quad (\text{free fermion}) \quad (3.23a)$$

$$- \frac{1}{4}V_{\mu\nu}V^{\mu\nu} + \frac{1}{2}m_V^2V^2 \quad (\text{free vector}) \quad (3.23b)$$

$$+ g_V V_\mu \bar{\chi}\gamma^\mu\chi. \quad (\text{interaction}) \quad (3.23c)$$

Note that the vector boson is assumed to be massive, as can be seen in the mass term containing m_V and $m_{V'}$ in (3.23b). The vector boson gains its mass via the Stueckelberg mechanism, which is explained in App. A.1, but since the Stueckelberg field is decoupled from the other fields, we do not include it in the Lagrangian. Contrary to the Stueckelberg mechanism, a gauged Higgs mechanism would give additional contributions to the scattering matrix.

Particle-Particle Scattering $\chi_F\chi_F \rightarrow \chi_F\chi_F V$

For particle-particle scattering with the gauge interaction (3.23c) we find that the squared matrix element is one half of the squared matrix element for the Yukawa coupling (3.11), assuming same masses and coupling strengths, *i.e.*

$$|\mathcal{M}|^2 = \frac{128}{9} \frac{g_V^6}{\omega^2} |\vec{k}|^2 |\vec{l}|^2 \left[1 + \frac{m_{V'}}{\omega} + 2 \frac{m_{V'}^2}{\omega^2} + 3(\hat{k} \cdot \hat{l})^2 \left(1 + \frac{3}{2} \frac{m_{V'}}{\omega} + \frac{1}{2} \frac{m_{V'}^2}{\omega^2} \right) \right] \quad (3.24)$$

$$\times \left[\frac{1}{(|\vec{k}|^2 + m_V^2)^2} + \frac{1}{(|\vec{l}|^2 + m_V^2)^2} - \frac{1}{(|\vec{k}|^2 + m_V^2)(|\vec{l}|^2 + m_V^2)} \right]$$

where again we distinguish between the mediator mass m_V and the emitted particle's mass $m_{V'}$. We can use the squared matrix element to calculate the cross section and energy loss rate in terms of dimensionless variables to get, in analogy to the emission of a scalar boson, where we again neglect the terms containing the emitted particle's mass but keep the mediator mass in the propagator

$$\sigma = \frac{1}{72} \frac{g_V^6}{m_\chi^2 \pi^3} \int_0^u dx \frac{1}{x} \left[S_{sq}(u, x, y) + S_{log}(u, x, y) \right] \quad (3.25)$$

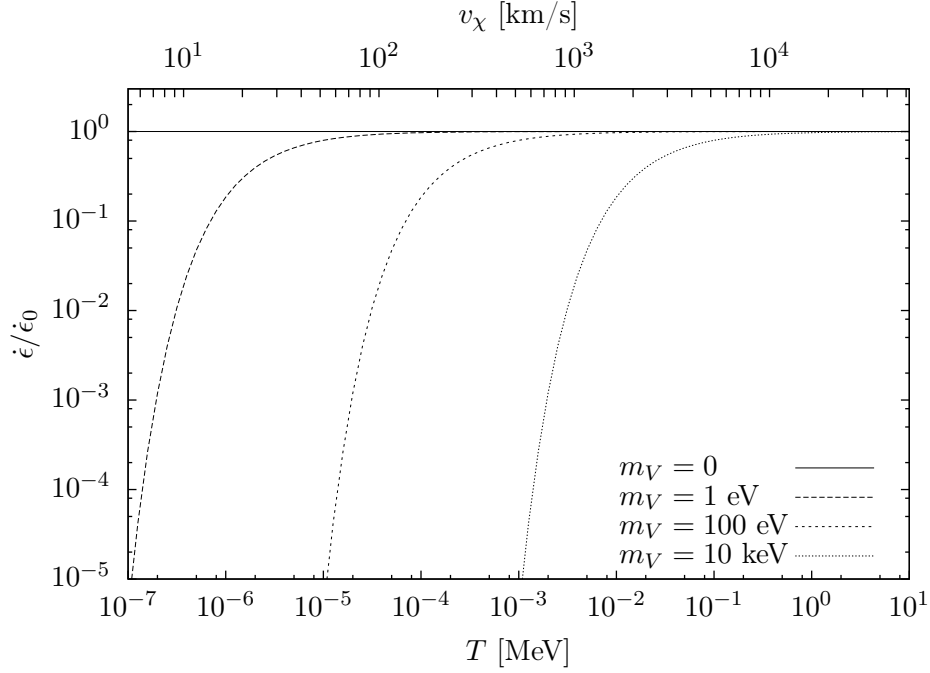


Figure 3.4: Effects of a finite vector boson mass on the energy loss rate for $m_\chi = 1$ GeV, where $\dot{\epsilon}_0$ corresponds to the energy loss rate for $m_V = 0$.

$$\dot{\epsilon} = \frac{1}{36} \frac{g_V^6 n_\chi^2 T^{3/2}}{\pi^{7/2} m_\chi^{5/2}} \int_0^\infty du u e^{-u} \int_0^u dx \left[S_{sq}(u, x, y) + S_{log}(u, x, y) \right] \quad (3.26)$$

with

$$S_{sq} = \left(\frac{4x^2}{4uy + (x-y)^2} - \frac{5}{2} \right) \sqrt{1 - \frac{x}{u}} \quad (3.27a)$$

$$S_{log} = \frac{1}{8u} \frac{16u^2 + x^2 + 5y^2 + 20uy - 16ux - 10xy}{2u - x + y} \ln \left[\frac{2u - x + y + 2\sqrt{u(u+x)}}{2u - x + y - 2\sqrt{u(u+x)}} \right]. \quad (3.27b)$$

For a massless mediator, $y \rightarrow 0$ and (3.26) simplifies to

$$\chi_F \chi_F \rightarrow \chi_F \chi_F V : \quad \dot{\epsilon} = \frac{188 - 9\pi^2}{432} \frac{g_V^6 n_\chi^2}{\pi^{7/2} m_\chi^{5/2}} T^{3/2} \quad (3.28)$$

The effects of a finite vector boson mass $m_V > 0$ on the energy loss rate can be seen in Fig. 3.4, where we show that the energy loss rate is exponentially suppressed if the vector boson mass is larger than the average kinetic energy $m_V \gtrsim 3T$.

Particle-Antiparticle Scattering $\chi_F \bar{\chi}_F \rightarrow \chi_F \bar{\chi}_F V$

For particle-antiparticle scattering, to leading order in the fermion velocity v_χ , the squared matrix element is

$$|\mathcal{M}|^2 = \frac{512}{3} \frac{g^6}{\omega^4} |\vec{k}|^2 \frac{|\vec{k}|^2 |\vec{l}|^2 (\hat{k} \cdot \hat{l})^2}{(|\vec{k}|^2 + m_V^2)^2} \left(1 + \frac{1}{2} \frac{m_V^2}{\omega^2} \right) \quad (3.29)$$

which is of lower order in v_χ than (3.24). The reason for this is a non-vanishing dipole moment of the system, since the fermion and anti-fermion are oppositely charged under the underlying $U(1)$ gauge group. The opposite charges of fermion and anti-fermion result in an attractive force between the particles, whereas two fermions carry the same charge resulting in a repulsive force. For the Yukawa coupling, the dark matter fermions are not charged under any gauge group, opening the possibility for them to be of Majorana kind. Therefore, the squared matrix elements for particle-particle scattering (3.11) and for particle-antiparticle scattering (3.17) are of the same order in v_χ .

For the cross section and energy loss rate we get

$$\sigma = \frac{1}{12} \frac{g_V^6}{\pi^3 m_V} \int_0^u dx \frac{1}{x} [S_{sq}(u, x, y) + S_{log}(u, x, y)] \quad (3.30)$$

$$\dot{\epsilon} = \frac{1}{3} \frac{g_V^6 n_\chi^2 T^{1/2}}{\pi^{7/2} m_\chi^{3/2}} \int_0^\infty du u e^{-u} \int_0^u dx \frac{1}{y} [S_{sq}(u, x, y) + S_{log}(u, x, y)] \quad (3.31)$$

with

$$S_{sq} = -\frac{2y^2}{4uy + (x-y)^2} \sqrt{1 - \frac{x}{u}} \quad (3.32a)$$

$$S_{log} = \frac{y}{2u} \ln \left[\frac{2u - x + y + 2\sqrt{u(u-x)}}{2u - x + y - 2\sqrt{u(u-x)}} \right]. \quad (3.32b)$$

For a massless mediator, the contribution of S_{sq} to the energy loss rate can be neglected and the contribution of S_{log} becomes analytic, yielding a simple expression for the energy loss rate

$$\chi_F \bar{\chi}_F \rightarrow \chi_F \bar{\chi}_F V : \quad \dot{\epsilon} = \frac{2}{3} \frac{g_V^6 n_\chi^2}{\pi^{7/2} m_\chi^{3/2}} T^{1/2} \quad (3.33)$$

Because of the non-vanishing dipole moment, the energy loss rate is much larger for particle-antiparticle scattering than for particle-particle scattering, as can be seen in

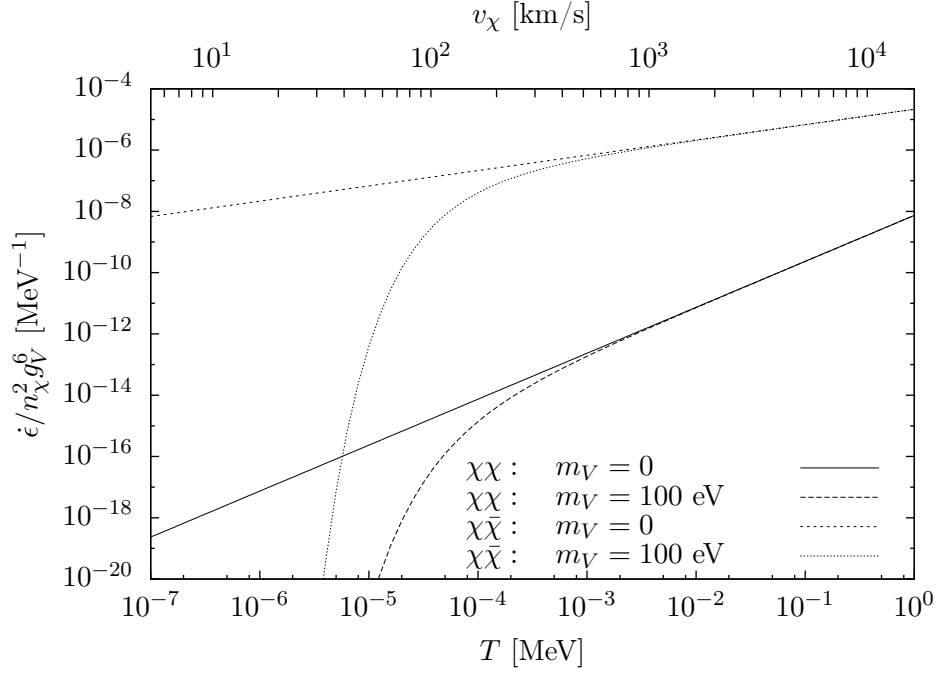


Figure 3.5: Effects of a finite vector boson mass on the energy loss rate for $\chi\chi \rightarrow \chi\chi V$ in comparison to $\chi\bar{\chi} \rightarrow \chi\bar{\chi} V$. The fermion mass is taken to be $m_\chi = 1$ GeV.

Fig. 3.5 for two different vector boson masses. The two cases also have a different temperature dependence (*i.e.* $\dot{\epsilon} \propto T^{3/2}$ for $\chi\chi$ and $\dot{\epsilon} \propto T^{1/2}$ for $\chi\bar{\chi}$). This would lead to a crossing of the two lines in Fig. 3.5 for high temperatures, but in this region our non-relativistic approximation breaks down.

3.3 Scalar Boson Scattering

For the scattering process of two dark matter scalar bosons, we have to consider the diagrams in Fig. 3.6 in addition to the diagrams in Fig. 3.1. This yields a larger amount of Feynman amplitudes which have to be evaluated, but the calculation of each of the amplitudes is much easier for scalar boson scattering. Since in the following we are considering bosons only, we include couplings where the mediator and the emitted particle meet in a vertex (e) and (f), a quartic coupling of the CDM scalars (g) and trilinear couplings between the heavy scalar bosons (h) and (i). Again, we label the t-channel with latin letters, the u-channel with primed letters and the s-channel with double primed ones. Diagrams (g) is representative for four diagrams with particle emission from any external leg and diagrams (h) and (i) are representative for all channels and the emission from any of the four external legs with the heavy scalar χ

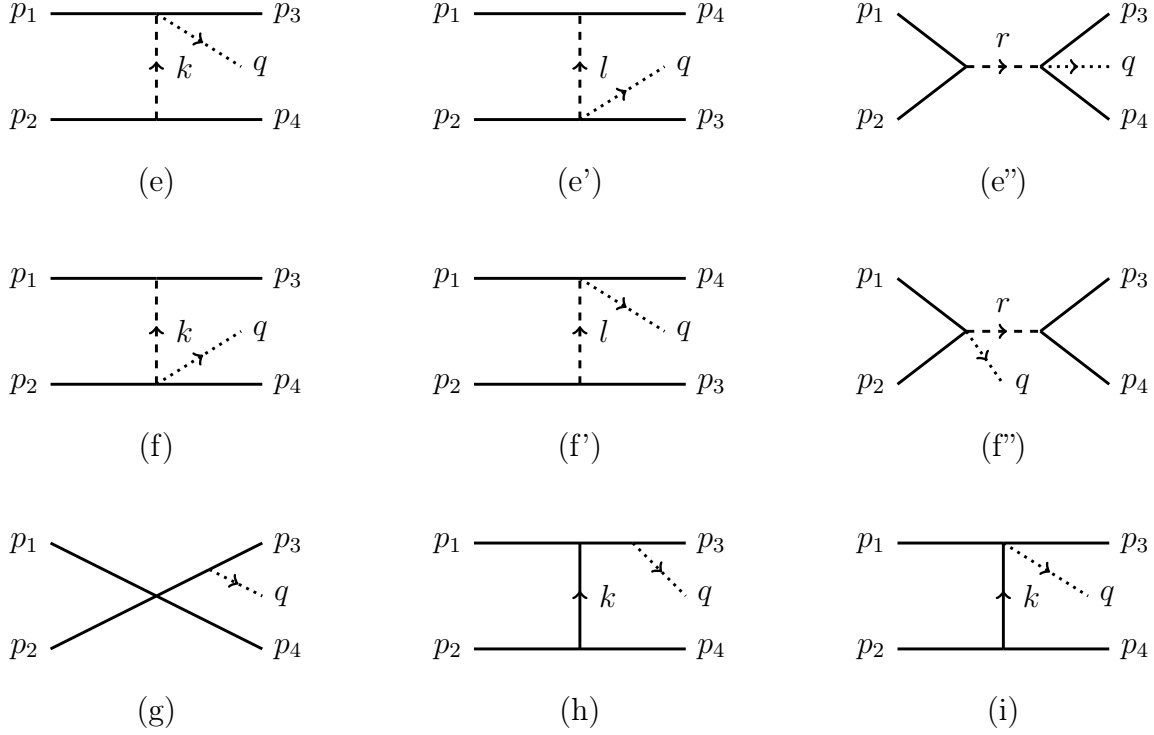


Figure 3.6: *Additional* tree level diagrams contributing to bremsstrahlung processes in scalar CDM scattering. Diagram (g) is representative for the four χ^4 diagrams (where like for all other diagrams, the particle can be emitted from any of the four external legs). We neglect (g) since it is suppressed by a factor $k^2/m_\chi^2 = \mathcal{O}(v^2)$ compared to the leading order. Diagrams (h) and (i) represent the 3 channels of the the two diagrams (18 diagrams in total) containing vertices that include an odd number of χ_S which we forbid by imposing a global $U(1)$ symmetry resulting in the conservation of the number of χ_S at each vertex. Diagrams (h) and (i), in case they are not forbidden, are also suppressed by a factor of $k^2/m_\chi^2 = \mathcal{O}(v^2)$. The momentum flow is chosen from left to right (or from bottom to top for vertical lines).

as mediator⁵, yielding 28 additional diagrams (see Fig. 3.6). For the χ^4 interaction diagrams (g), there is only one channel. We neglect the diagrams (g)-(i) because they are suppressed by a factor $k^2/m_\chi^2 = \mathcal{O}(v^2)$ compared to the diagrams (a)-(f), which yields a total number of 18 diagrams considering all three channels. The corresponding Feynman amplitudes can be found in App. A.2.

3.3.1 Gauge Interaction

We first treat the case of a vector boson, because here we have to deal with a gauge coupling which resembles the cases we have treated in the previous sections. We get the full Lagrangian for scalar CDM with a real vector boson V^μ from $\mathcal{L} = -\frac{1}{4}V_{\mu\nu}V^{\mu\nu} + (D_\mu\chi)^\dagger(D^\mu\chi) - V(\chi)$ with $V_{\mu\nu} = \partial_\mu V_\nu - \partial_\nu V_\mu$ and the gauge coupling $D_\mu = \partial_\mu - ig_V V_\mu$:

$$\mathcal{L} = (\partial_\mu\chi)^\dagger(\partial^\mu\chi) - m^2\chi^\dagger\chi \quad (\text{free scalar}) \quad (3.34a)$$

$$- \frac{1}{4}V_{\mu\nu}V^{\mu\nu} + \frac{1}{2}m_V^2V^2 \quad (\text{free vector}) \quad (3.34b)$$

$$+ g_V^2\chi^\dagger\chi V^2 + ig_V V^\mu [(\partial_\mu\chi^\dagger)\chi - \chi^\dagger(\partial_\mu\chi)] - \frac{1}{4}\lambda(\chi^\dagger\chi)^2 \quad (\text{interaction}) \quad (3.34c)$$

where the interaction part of \mathcal{L} can be read off the last line. The first two terms in (3.34c) come from the gauge coupling and the last term from the scalar potential. We assume that $g_V < 1$ and $0 < \lambda < 1$. The scalar field χ has to be complex because the gauge coupling is associated with a local $U(1)$ symmetry $\chi \rightarrow e^{i\alpha(x)}\chi$, which can only be fulfilled if χ is complex. In other words, the gauge interaction implies a positive and a negative charge and we need two degrees of freedom to represent both charges. The $U(1)$ symmetry also implies that the charge is conserved at each vertex, forbidding diagrams of the type (h) and (i) in Fig. 3.6.

Particle-Particle Scattering $\chi_S\chi_S \rightarrow \chi_S\chi_S V$

For particle-particle scattering we consider diagrams (a)-(d) and (a')-(d') in Fig. 3.1 as well as (e)-(f) and (e')-(f'). We neglect diagrams of the type (g) in Fig. 3.6 because they are suppressed by a factor m_V^2/m_χ^2 compared to the other diagrams and find for

⁵Beware that in this section χ will denote a scalar field. We will use the subscript S for scalar at points where it might be unclear in order to emphasise this fact.

the squared matrix element

$$|\mathcal{M}|^2 = \frac{32}{9} \frac{g_V^6}{\omega^2} |\vec{k}|^2 |\vec{l}|^2 \left[1 + \frac{m_{V'}}{\omega} + 2 \frac{m_{V'}^2}{\omega^2} + 3(\hat{k} \cdot \hat{l})^2 \left(1 + \frac{3}{2} \frac{m_{V'}}{\omega} + \frac{1}{2} \frac{m_{V'}^2}{\omega^2} \right) \right] \times \left[\frac{1}{(|\vec{k}|^2 + m_V^2)^2} + \frac{1}{(|\vec{l}|^2 + m_V^2)^2} + \frac{2}{(|\vec{k}|^2 + m_V^2)(|\vec{l}|^2 + m_V^2)} \right] \quad (3.35)$$

yielding for the cross section and energy loss rate for $m_{V'} \rightarrow 0$

$$\sigma = \frac{1}{18} \frac{g_V^6}{m_\chi^2 \pi^3} \int_0^u dx \frac{1}{x} [S_{sq}(u, x, y) + S_{log}(u, x, y)] \quad (3.36)$$

$$\dot{\epsilon} = \frac{1}{9} \frac{g_V^6 n_\chi^2 T^{3/2}}{\pi^{7/2} m_\chi^{5/2}} \int_0^\infty du u e^{-u} \int_0^u dx [S_{sq}(u, x, y) + S_{log}(u, x, y)] \quad (3.37)$$

with

$$S_{sq} = \frac{1}{4} \left(\frac{4x^2}{4uy + (x-y)^2} - 1 \right) \sqrt{1 - \frac{x}{u}} \quad (3.38a)$$

$$S_{log} = \frac{1}{8u} \frac{(8u^2 + 5x^2 + y^2 + 4uy - 8ux - 2xy)}{2u - x + y} \ln \left[\frac{2u - x + y + 2\sqrt{u(u-x)}}{2u - x + y - 2\sqrt{u(u-x)}} \right]. \quad (3.38b)$$

For a massless mediator, the energy loss rate is

$$\chi_S \chi_S \rightarrow \chi_S \chi_S V : \quad \dot{\epsilon} = \frac{9\pi^2 - 20}{216} \frac{g_V^6 n_\chi^2}{\pi^{7/2} m_\chi^{5/2}} T^{3/2}. \quad (3.39)$$

The temperature dependence for the emission of a vector boson is $\dot{\epsilon} \propto T^{3/2}$ for both scalar and fermionic CDM. However, the effects of a finite vector boson mass on the energy loss rate are larger for fermionic CDM than for scalar CDM as can be seen in Fig. 3.7. The difference is solely due to the interference terms, *i.e.* the last term in (3.40) and (3.24), which is larger and carries a positive sign for scalar CDM as opposed to a negative sign for fermionic CDM.

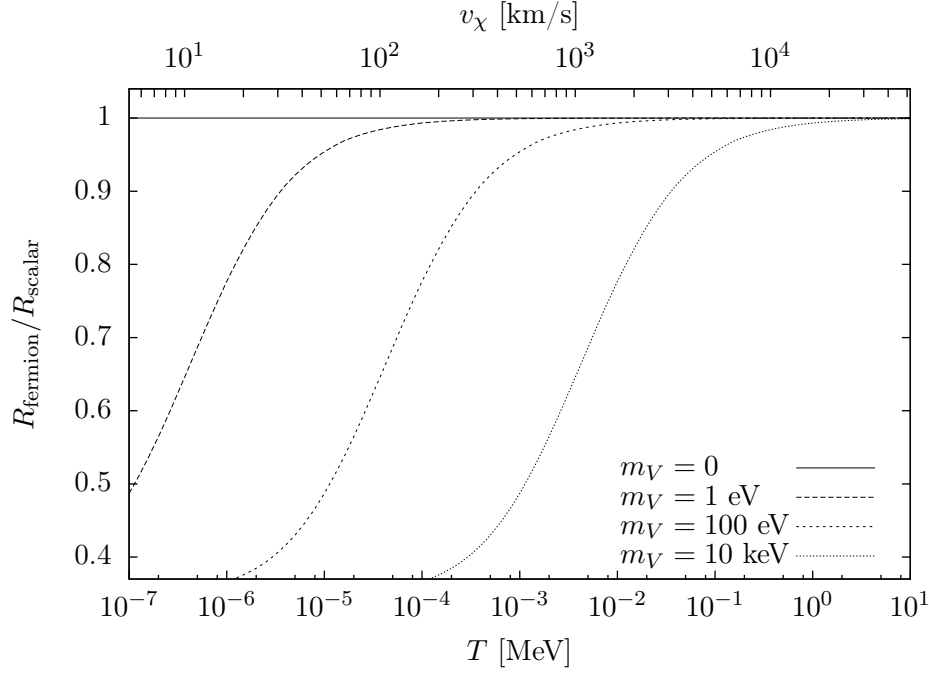


Figure 3.7: Comparison of energy loss rates for fermionic and scalar CDM scattering for $m_\chi = 1$ GeV, where $R = \dot{\epsilon}/\dot{\epsilon}_0$. The effects of a finite vector boson mass are larger for $\chi_F\chi_F \rightarrow \chi_F\chi_F V$ than for $\chi_S\chi_S \rightarrow \chi_S\chi_S V$.

Particle-Antiparticle Scattering $\chi_S\chi_S^\dagger \rightarrow \chi_S\chi_S^\dagger V$

For particle-antiparticle scattering the squared matrix element is

$$|\mathcal{M}|^2 = \frac{128}{3} \frac{g_V^6}{\omega^4} |\vec{k}|^2 \frac{|\vec{k}|^2 |\vec{l}|^2 (\hat{k} \cdot \hat{l})^2}{(|\vec{k}|^2 + m_V^2)^2} \left(1 + \frac{1}{2} \frac{m_V^2}{\omega^2} \right) \quad (3.40)$$

yielding for the cross section and energy loss rate the same expression as for $\chi_F\bar{\chi}_F \rightarrow \chi_F\bar{\chi}_F V$

$$\sigma = \frac{1}{12} \frac{g_V^6}{\pi^3 m_V^2} \int_0^u dx \frac{1}{x} \left[S_{sq}(u, x, y) + S_{log}(u, x, y) \right] \quad (3.41)$$

$$\dot{\epsilon} = \frac{1}{3} \frac{g_V^6 n_\chi^2 T^{1/2}}{\pi^{7/2} m_\chi^{3/2}} \int_0^\infty du u e^{-u} \int_0^u dx \frac{1}{y} \left[S_{sq}(u, x, y) + S_{log}(u, x, y) \right] \quad (3.42)$$

with

$$S_{sq} = -\frac{2y^2}{4uy + (x-y)^2} \sqrt{1 - \frac{x}{u}} \quad (3.43a)$$

$$S_{log} = \frac{y}{2u} \ln \left[\frac{2u - x + y + 2\sqrt{u(u-x)}}{2u - x + y - 2\sqrt{u(u-x)}} \right]. \quad (3.43b)$$

For a massless mediator, the contribution of S_{sq} to the energy loss rate can be neglected and the contribution of S_{log} becomes analytic, yielding for the energy loss rate

$$\chi S \chi_S^\dagger \rightarrow \chi S \chi_S^\dagger V : \quad \dot{\epsilon} = \frac{2}{3} \frac{g_V^6 n_\chi^2}{\pi^{7/2} m_\chi^{3/2}} T^{1/2}. \quad (3.44)$$

3.3.2 Scalar Interaction

The Lagrangian \mathcal{L} for scalar dark matter χ with a scalar ϕ reads as follows

$$\mathcal{L} = (\partial_\mu \chi)^\dagger (\partial^\mu \chi) + \frac{1}{2} (\partial_\mu \phi)^2 \quad (\text{kinetic terms}) \quad (3.45a)$$

$$- \frac{1}{2} m_\phi^2 \phi^2 - \frac{1}{3!} A_\phi \phi^3 - \frac{1}{4!} \lambda_\phi \phi^4 \quad (\phi \text{ potential}) \quad (3.45b)$$

$$- m_\chi^2 \chi^\dagger \chi - \frac{1}{4} \lambda (\chi^\dagger \chi)^2 \quad (\chi \text{ potential}) \quad (3.45c)$$

$$- \frac{1}{2} g_\phi^2 \chi^\dagger \chi \phi^2 - A_{\chi\phi} \chi^\dagger \chi \phi \quad (\text{interaction}) \quad (3.45d)$$

where we impose a global $U(1)$ symmetry for χ in order to forbid terms of the kind $\lambda' \phi \chi^\dagger \chi (\chi + \chi^\dagger)$ or $A_\chi \chi^\dagger \chi (\chi + \chi^\dagger)$. This Lagrangian differs from all previous ones in the second term, which is a trilinear coupling term between the scalar CDM χ and the light scalar ϕ . $A_{\chi\phi}$ is a coupling of dimension 1. In order to maintain the power counting scheme introduced in App. A.3, we will have to assign kinematic constraints to $A_{\chi\phi}$.

Particle-Particle Scattering $\chi S \chi S \rightarrow \chi S \chi S \phi$

For particle-particle scattering we have to consider diagrams (a)-(f) and (a')-(f') in Fig. 3.1. The full result for the squared matrix element to second order in v_χ is

$$|\mathcal{M}|^2 = \frac{|\vec{k}|^2 |\vec{l}|^2}{\omega^2} \left[\frac{1}{9} \frac{A_{\chi\phi}^6}{m_\chi^6} - \frac{4}{3} \frac{g^2 A_{\chi\phi}^4}{m_\chi^4} (\hat{k} \cdot \hat{l})^2 + 4 \frac{g^4 A_{\chi\phi}^2}{m_\chi^2} (\hat{k} \cdot \hat{l})^2 + \frac{4}{3} \frac{g^2 A_{\chi\phi}^4}{m_\chi^4} \frac{\omega}{m_\chi} \right] \times \left[\frac{1}{(|\vec{k}|^2 + m_\phi^2)^2} + \frac{1}{(|\vec{l}|^2 + m_\phi^2)^2} + \frac{2}{(|\vec{k}|^2 + m_\phi^2)(|\vec{l}|^2 + m_\phi^2)} \right]. \quad (3.46)$$

The first three terms in the first line of (3.46) are the leading order in v_χ , while the last term is the full next-to-leading-order result according to our power counting scheme, but, depending on the magnitude of $A_{\chi\phi}$, the last term might not be negligible compared to the first three terms. Imposing that the last term should be smaller than

any of the first three terms, we get

$$\underbrace{\sqrt{\frac{\omega}{m_\chi}}}_{\mathcal{O}(v_\chi)} < \frac{A_{\chi\phi}}{g_\phi m_\chi} < \underbrace{\frac{\sqrt{m_\chi^3 \omega}}{|\vec{k}||\vec{l}|}}_{\mathcal{O}(v_\chi^{-2})} \quad (3.47)$$

i.e., $A_{\chi\phi}/m_\chi$ is of approximately the same order as g_ϕ . If $A_{\chi\phi}/g_\phi m_\chi$ reaches the lower bound of (3.47), the last term in (3.46) becomes comparable to the first term. However, in this case the third term is much larger than all the other terms, which therefore can be collectively neglected. If $A_{\chi\phi}/g_\phi m_\chi$ reaches the upper bound of (3.47), the last term in (3.46) becomes comparable to the third term. In that case, the first term is much larger than all the other terms (as can be seen in Fig. 3.8). Thus, the $\mathcal{O}(v_\chi^2)$ -term never gives a dominant contribution to the squared matrix element and quantities deduced from it and can always be neglected. The only constraint, we have to impose is $A_{\chi\phi}/m_\chi < 1$ for perturbation theory to work.

In order to perform the integral in the cross section and energy loss rate using the dimensionless variables defined in App. A.3, we have to split up the remaining three terms to obtain

$$\sigma_1 = \frac{1}{2304} \frac{A_{\chi\phi}^6}{m_\chi^8 \pi^3} \int_0^u dx \frac{1}{x} \left[-y(4u - 2x + y) S_{sq}(u, x, y) + \right. \\ \left. + (4u^2 + 2x^2 + y^2 - 4ux + 4uy - 2xy) S_{log}(u, x, y) \right] \quad (3.48a)$$

$$\sigma_2 = \frac{1}{192} \frac{g_\phi^2 A_{\chi\phi}^4}{m_\chi^6 \pi^3} \int_0^u dx \left[-S_{sq}(u, x, y) - S_{log}(u, x, y) \right] \quad (3.48b)$$

$$\sigma_3 = \frac{1}{64} \frac{g_\phi^4 A_{\chi\phi}^2}{m_\chi^4 \pi^3} \int_0^u dx \left[S_{sq}(u, x, y) + S_{log}(u, x, y) \right] \quad (3.48c)$$

with $\sigma = \sigma_1 + \sigma_2 + \sigma_3$ and

$$S_{sq} = \frac{1}{4uy + (x - y)^2} \sqrt{1 - \frac{x}{u}} \quad (3.49a)$$

$$S_{log} = \frac{1}{4u} \frac{1}{2u - x + y} \ln \left[\frac{2u - x + y + 2\sqrt{u(u - x)}}{2u - x + y - 2\sqrt{u(u - x)}} \right]. \quad (3.49b)$$

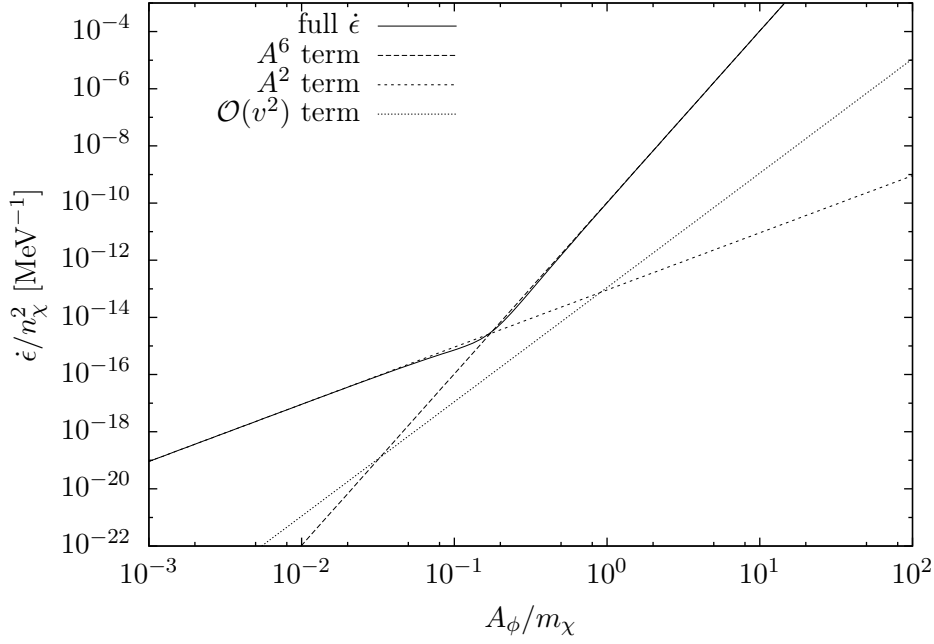


Figure 3.8: Energy loss rate as a function of the trilinear coupling constant $A_{\chi\phi}$ for $m_\chi = 1$ GeV, $g_\phi = 0.1$ and $T = 1$ MeV. At the point where the $\mathcal{O}(v^2)$ term in (3.46) becomes comparable to the $A_{\chi\phi}^2$ term, both terms are negligible to the $A_{\chi\phi}^6$ term (and vice versa).

The energy loss rate for a massless mediator ($y \rightarrow 0$) is

$$\chi_S \chi_S \rightarrow \chi_S \chi_S \phi : \quad \dot{\epsilon} = \left(\frac{5}{864} \frac{A_{\chi\phi}^6}{m_\chi^6} - \frac{3\pi^2 - 20}{576} \frac{g_\phi^2 A_{\chi\phi}^4}{m_\chi^4} + \frac{3\pi^2 - 20}{192} \frac{g_\phi^4 A_{\chi\phi}^2}{m_\chi^2} \right) \frac{n_\chi^2}{\pi^{7/2} m_\chi^{5/2}} T^{3/2} \quad (3.50)$$

and for the asymptotic cases

$$\frac{A_{\chi\phi}}{g_\phi m_\chi} \ll 1 : \quad \dot{\epsilon} = \frac{3\pi^2 - 20}{192} \frac{g_\phi^4 A_{\chi\phi}^2 n_\chi^2}{\pi^{7/2} m_\chi^{9/2}} T^{3/2} \quad (3.51a)$$

$$\frac{A_{\chi\phi}}{g_\phi m_\chi} \gg 1 : \quad \dot{\epsilon} = \frac{5}{864} \frac{A_{\chi\phi}^6 n_\chi^2}{\pi^{7/2} m_\chi^{17/2}} T^{3/2}. \quad (3.51b)$$

Particle-Antiparticle Scattering $\chi_S \chi_S^\dagger \rightarrow \chi_S \chi_S^\dagger \phi$

For particle-antiparticle scattering the squared matrix element is dominated by the t-channel, yielding

$$|\mathcal{M}|^2 = \frac{|\vec{k}|^2 |\vec{l}|^2}{\omega^2 (|\vec{k}|^2 + m_\phi^2)^2} \left(\frac{1}{9} \frac{A_{\chi\phi}^6}{m_\chi^6} - \frac{4}{3} \frac{g^2 A_{\chi\phi}^4}{m_\chi^4} (\hat{k} \cdot \hat{l})^2 + 4 \frac{g^4 A_{\chi\phi}^2}{m_\chi^2} (\hat{k} \cdot \hat{l})^2 \right). \quad (3.52)$$

The energy loss rate is

$$\chi_S \chi_S^\dagger \rightarrow \chi_S \chi_S^\dagger \phi : \quad \dot{\epsilon} = \left(\frac{1}{108} \frac{A_{\chi\phi}^6}{m_\chi^6} - \frac{1}{36} \frac{g_\phi^2 A_{\chi\phi}^4}{m_\chi^4} + \frac{1}{12} \frac{g_\phi^4 A_{\chi\phi}^2}{m_\chi^2} \right) \frac{n_\chi^2}{\pi^{7/2} m_\chi^{5/2}} T^{3/2} \quad (3.53)$$

and for the asymptotic cases of $A_{\chi\phi}$ we get

$$\frac{A_{\chi\phi}}{g_\phi m_\chi} \ll 1 : \quad \dot{\epsilon} = \frac{1}{12} \frac{g_\phi^4 A_{\chi\phi}^2 n_\chi^2}{\pi^{7/2} m_\chi^{9/2}} T^{3/2} \quad (3.54a)$$

$$\frac{A_{\chi\phi}}{g_\phi m_\chi} \gg 1 : \quad \dot{\epsilon} = \frac{1}{108} \frac{A_{\chi\phi}^6 n_\chi^2}{\pi^{7/2} m_\chi^{17/2}} T^{3/2}. \quad (3.54b)$$

Real Scalar Scattering $\tilde{\chi}_S \tilde{\chi}_S \rightarrow \tilde{\chi}_S \tilde{\chi}_S \phi$

If we consider the CDM particle to be described by a real scalar field $\tilde{\chi}_S \equiv \chi_S = \chi_S^\dagger$, we also have to consider the annihilation diagrams in Fig. 3.1 and 3.6. The Lagrangian for a real scalar field is

$$\mathcal{L} = \frac{1}{2} (\partial_\mu \chi)^2 + \frac{1}{2} (\partial_\mu \phi)^2 \quad (\text{kinetic terms}) \quad (3.55a)$$

$$- \frac{1}{2} m_\phi^2 \phi^2 - \frac{1}{3!} A_\phi \phi^3 - \frac{1}{4!} \lambda_\phi \phi^4 \quad (\phi \text{ potential}) \quad (3.55b)$$

$$- \frac{1}{2} m_\chi^2 \chi^2 - \frac{1}{3!} A_\chi \chi^3 - \frac{1}{4!} \lambda_\chi \chi^4 \quad (\chi \text{ potential}) \quad (3.55c)$$

$$- \frac{1}{4} g_\phi^2 \chi^2 \phi^2 - \frac{1}{2} A_{\chi\phi} \chi^2 \phi \quad (\text{interaction}) \quad (3.55d)$$

where we now have to consider the cubic term in (3.55c) since there is no $U(1)$ -symmetry for χ . However, imposing that $\langle \chi \rangle = 0$ we find in analogy to Fig. 3.2 that A_χ has to be small and therefore can be neglected. In accordance with the case of a Majorana fermion field, the Lagrangian for a real scalar field has gained several prefactors in comparison to the Lagrangian for a complex scalar field. These prefactors are canceled by the increased number of possible Wick contractions. Since the terms

	SCALAR BOSON EMISSION	VECTOR BOSON EMISSION
FERMION SCATTERING	$\chi\chi :$ $\frac{188-9\pi^2}{216} \frac{g^6 n_\chi^2}{\pi^{7/2} m_\chi^{5/2}} T^{3/2}$	$\frac{188-9\pi^2}{432} \frac{g^6 n_\chi^2}{\pi^{7/2} m_\chi^{5/2}} T^{3/2}$
	$\chi\bar{\chi} :$ $\frac{28}{27} \frac{g^6 n_\chi^2}{\pi^{7/2} m_\chi^{5/2}} T^{3/2}$	$\frac{2}{3} \frac{g^6 n_\chi^2}{\pi^{7/2} m_\chi^{3/2}} T^{1/2}$
SCALAR BOSON SCATTERING	$\chi\chi :$ $\left(\frac{5}{864} \frac{A_{X\phi}^6}{m_\chi^6} - \frac{3\pi^2-20}{576} \frac{g_\phi^2 A_{X\phi}^4}{m_\chi^4} + \frac{3\pi^2-20}{192} \frac{g_\phi^4 A_{X\phi}^2}{m_\chi^2} \right) \frac{n_\chi^2}{\pi^{7/2} m_\chi^{5/2}} T^{3/2}$	$\frac{9\pi^2-20}{216} \frac{g^6 n_\chi^2}{\pi^{7/2} m_\chi^{5/2}} T^{3/2}$
	$\chi\chi^\dagger :$ $\left(\frac{1}{108} \frac{A_{X\phi}^6}{m_\chi^6} - \frac{1}{36} \frac{g_\phi^2 A_{X\phi}^4}{m_\chi^4} + \frac{1}{12} \frac{g_\phi^4 A_{X\phi}^2}{m_\chi^2} \right) \frac{n_\chi^2}{\pi^{7/2} m_\chi^{5/2}} T^{3/2}$	$\frac{2}{3} \frac{g^6 n_\chi^2}{\pi^{7/2} m_\chi^{3/2}} T^{1/2}$

Table 3.1: Energy loss rates $\dot{\epsilon}$ for the emission of a massless particle for different interacting dark matter scenarios. In all models with a vanishing dipole moment the energy loss rate shows a $T^{3/2}$ behavior, while the energy loss rate for two differently charged particles shows a $T^{1/2}$ behavior.

involving annihilation diagrams are suppressed by at least a factor $k^2/r^2 \sim v^2$, the leading order contribution of real scalar scattering yields the same result as complex scalar particle-particle scattering.

3.4 Elastic Scattering Cross Section

In this section we want to compute the elastic scattering cross sections for all the CDM models discussed in this chapter. To leading order in v_χ , the squared matrix element for elastic CDM scattering for a scalar as well as a vector mediator is

$$|\mathcal{M}_{el}|^2 = 64g^4m_\chi^4 \left(\frac{1}{(|\vec{k}|^2 + m_M^2)^2} + \frac{1}{(|\vec{l}|^2 + m_M^2)^2} \pm \frac{1}{(|\vec{k}|^2 + m_M^2)(|\vec{l}|^2 + m_M^2)} \right) \quad (3.56)$$

where the sign of the last term is positive for bosons and negative for fermions and for particle-antiparticle scattering only the first term (*i.e.* t-channel) contributes. For scalar CDM with the dimensionful coupling, we have to make the replacement $g \rightarrow A/2m_\chi$. The total cross section for fermion particle-particle scattering is given by

$$\begin{aligned} \sigma_{el} &= \frac{1}{256} \frac{g^4 m_\chi^2}{\pi} \int_{-1}^1 d(\cos \theta) \frac{(|\vec{p}_{rel}|^2 + m_M^2)^2 + 3|\vec{p}_{rel}|^4 \cos^2 \theta}{\left[(|\vec{p}_{rel}|^2 + m_M^2)^2 - |\vec{p}_{rel}|^4 \cos^2 \theta \right]^2} \\ &= \frac{g^4}{16\pi} \left[\frac{1}{m_M^2 v_{rel}^2} \frac{m_\chi^2 v_{rel}^2}{m_\chi^2 v_{rel}^2 + m_M^2} - \frac{1}{m_\chi^2 v_{rel}^4} \ln \left(1 + \frac{m_\chi^2 v_{rel}^2}{m_M^2} \right) \frac{m_\chi^2 v_{rel}^2}{m_\chi^2 v_{rel}^2 + 2m_M^2} \right], \end{aligned} \quad (3.57)$$

and for scalar bosons

$$\begin{aligned} \sigma_{el} &= \frac{1}{64} \frac{g^4 m_\chi^2}{\pi^4} \int_{-1}^1 d(\cos \theta) \frac{3(|\vec{p}_{rel}|^2 + m_M^2)^2 + |\vec{p}_{rel}|^4 \cos^2 \theta}{\left((|\vec{p}_{rel}|^2 + m_M^2)^2 - |\vec{p}_{rel}|^4 \cos^2 \theta \right)^2} \\ &= \frac{g^4}{16\pi^4} \left[\frac{1}{m_M^2 v_{rel}^2} \frac{m_\chi^2 v_{rel}^2}{m_\chi^2 v_{rel}^2 + m_M^2} + \frac{1}{m_\chi^2 v_{rel}^4} \ln \left(1 + \frac{m_\chi^2 v_{rel}^2}{m_M^2} \right) \frac{m_\chi^2 v_{rel}^2}{m_\chi^2 v_{rel}^2 + 2m_M^2} \right], \end{aligned} \quad (3.58)$$

where $\vec{p}_{rel} = 2\vec{p}_i = m_\chi \vec{v}_{rel} = 2m_\chi \vec{v}_\chi$ is the relative momentum of the colliding particles, m_M is the mediator mass and $\cos \theta = (\vec{p}_i \cdot \vec{p}_f)/|\vec{p}_i||\vec{p}_f|$ is the scattering angle. For

particle-antiparticle scattering, the cross section for fermions and scalar bosons is

$$\begin{aligned}\sigma_{\text{el}} &= \frac{1}{32\pi} g^4 m_\chi^2 \int_{-1}^1 d(\cos \theta) \frac{1}{\left(|\vec{p}_{\text{rel}}|^2 + m_M^2 - |\vec{p}_{\text{rel}}|^2 \cos \theta\right)^2} \\ &= \frac{1}{16\pi} \frac{g^4}{m_M^2 v_{\text{rel}}^2} \frac{m_\chi^2 v_{\text{rel}}^2}{m_\chi^2 v_{\text{rel}}^2 + m_M^2}.\end{aligned}\quad (3.59)$$

As known from Bhabha and Møller scattering in QED, the differential cross section has a singularity along the beam axis of the colliding particles for a vanishing mediator mass. Explicitly, the differential cross section for particle-antiparticle scattering

$$\frac{d\sigma}{d\Omega} \propto \frac{1}{(1 - \cos \theta)^2} = \frac{1}{(1 - \cos^2 \frac{\theta}{2} + \sin^2 \frac{\theta}{2})^2} \propto \frac{1}{\sin^4 \frac{\theta}{2}} \quad (3.60)$$

diverges for $\theta = 0$ (*i.e.* forward scattering), while the differential cross section for particle-particle scattering

$$\frac{d\sigma}{d\Omega} \propto \frac{1}{(1 - \cos^2 \theta)^2} = \frac{1}{\sin^4 \theta} \quad (3.61)$$

has a singularity for $\theta = 0$ and $\theta = \pi$ because one cannot distinguish between forward and backward scattering of identical particles. The singularities in the differential cross section lead to a $1/m_M^2$ divergence of the cross section for a vanishing mediator mass in all cases. For forward scattering, the DM trajectories are unchanged, meaning that the diverging cross section in forward (and backward) direction does not influence the DM distribution. For this purpose, one introduces the transport cross section σ_T for particle-antiparticle scattering which regularizes the forward scattering and the viscosity cross section σ_V for particle-particle scattering of identical particles which regularizes the forward and backward scattering, *i.e.*,

$$\sigma_T = \int d\Omega (1 - \cos \theta) \frac{d\sigma}{d\Omega}, \quad (3.62a)$$

$$\sigma_V = \int d\Omega (1 - \cos^2 \theta) \frac{d\sigma}{d\Omega}. \quad (3.62b)$$

The transport/viscosity cross sections corresponding to (3.57), (3.58) and (3.59) are given by

$$\sigma_V^{\chi F \chi F} = \frac{1}{8\pi} \frac{g^4}{m_\chi^2 v_{\text{rel}}^4} \left[2 \ln \left(1 + \frac{m_\chi^2 v_{\text{rel}}^2}{m_M^2} \right) \frac{m_\chi^2 v_{\text{rel}}^2 + 5m_M^2 + 5\frac{m_M^4}{m_\chi^2 v_{\text{rel}}^2}}{m_\chi^2 v_{\text{rel}}^2 + 2m_M^2} - 5 \right], \quad (3.63)$$

$$\sigma_V^{\chi_S \chi_S} = \frac{1}{8\pi} \frac{g^4}{m_\chi^2 v_{\text{rel}}^4} \left[2 \ln \left(1 + \frac{m_\chi^2 v_{\text{rel}}^2}{m_M^2} \right) \frac{m_\chi^2 v_{\text{rel}}^2 + 3m_M^2 + 3 \frac{m_M^4}{m_\chi^2 v_{\text{rel}}^2}}{m_\chi^2 v_{\text{rel}}^2 + 2m_M^2} - 3 \right], \quad (3.64)$$

$$\sigma_T^{\chi \chi^\dagger} = \frac{1}{8\pi} \frac{g^4}{m_\chi^2 v_{\text{rel}}^4} \left[\ln \left(1 + \frac{m_\chi^2 v_{\text{rel}}^2}{m_M^2} \right) - \frac{m_\chi^2 v_{\text{rel}}^2}{m_\chi^2 v_{\text{rel}}^2 + m_M^2} \right]. \quad (3.65)$$

The transport/viscosity cross sections only diverge logarithmically with vanishing mediator mass. Equation (3.65) is in agreement with the Eqn. 6 in Ref. [32] where in the Born approximation only the t-channel was considered while (3.63) and (3.64) also include interference terms with the u-channel. For $m_M \ll m_\chi v_\chi$ the transport/viscosity cross section for all cases goes parametrically as

$$\sigma_{T,V} \propto \frac{g^4}{m_\chi^2 v_\chi^4}. \quad (3.66)$$

Soft Bremsstrahlung

In the case of soft bremsstrahlung (*i.e.* $\omega \ll m_\chi v_\chi^2$), it is possible to write the squared matrix element for fermion scattering as a product of the elastic squared matrix element and a term describing the emission of a particle

$$|\mathcal{M}|^2 \approx |\mathcal{M}_{\text{fact}}|^2 = |\mathcal{M}_{\text{el}}|^2 |\mathcal{F}|^2 \quad (3.67)$$

For the emission of a soft scalar, the fermion propagator plus external boson line is given by [compare 33, p.432]

$$g \frac{\not{p} + \not{q} + m}{(p+q)^2 - m^2} u(p) \approx g \frac{\not{p} + m}{2(p \cdot q)} u(p) = g \frac{m}{(p \cdot q)} u(p) \quad (3.68)$$

where in the last step we have used that $\not{p} u(p) = m u(p)$. For the factor $|\mathcal{F}|^2$ we get for both cases $\chi_F \chi_F \rightarrow \chi_F \chi_F \phi$ and $\chi_F \bar{\chi}_F \rightarrow \chi_F \bar{\chi}_F \phi$

$$\begin{aligned} |\mathcal{F}|^2 &= g^2 m^2 \left(\frac{1}{(p_3 \cdot q)} + \frac{1}{(p_4 \cdot q)} - \frac{1}{(p_1 \cdot q)} - \frac{1}{(p_2 \cdot q)} \right)^2 \\ &= \frac{4}{9} \frac{g^2}{m^4 \omega^2} |\vec{k}|^2 |\vec{l}|^2 \end{aligned} \quad (3.69)$$

which yields for particle-particle scattering

$$|\mathcal{M}_{\text{fact}}|^2 = \frac{256}{9} \frac{g^6}{\omega^2} |\vec{k}|^2 |\vec{l}|^2 \left(\frac{1}{(|\vec{k}|^2 + m_\phi^2)^2} + \frac{1}{(|\vec{l}|^2 + m_\phi^2)^2} - \frac{1}{(|\vec{k}|^2 + m_\phi^2)(|\vec{l}|^2 + m_\phi^2)} \right) \quad (3.70)$$

and the same expression without the last two terms for particle-antiparticle scattering. Comparing (3.70) to (3.11) and (3.17) one can see that $|\mathcal{M}_{\text{fact}}|^2$ lacks a term $[1 + 3(\hat{k} \cdot \hat{l})^2]$, *i.e.*,

$$|\mathcal{M}|^2 = |\mathcal{M}_{\text{fact}}|^2 \left[1 + 3(\hat{k} \cdot \hat{l})^2 \right] \quad (3.71)$$

This discrepancy can be explained by the fact, that the power counting scheme introduced in App. A.3 only assumes small CDM velocities $v_\chi \ll 1$ but does not make any assumptions (except of kinematical kind) about the energy ω of the emitted particle. Assuming that $\omega \ll m_\chi v_\chi^2$ renders the second term in (3.71) negligible since

$$(\hat{k} \cdot \hat{l}) = \mathcal{O} \left(\frac{\omega}{m_\chi v_\chi^2} \right). \quad (3.72)$$

For the emission of a soft vector boson, the fermion propagator plus external boson line is given by

$$g \frac{\not{p} + \not{q} + m}{(p+q)^2 - m^2} (\gamma \cdot \epsilon^*) u(p) \approx g \frac{\not{p} + m}{2(p \cdot q)} (\gamma \cdot \epsilon^*) u(p) = g \frac{(p \cdot \epsilon^*)}{(p \cdot q)} u(p) \quad (3.73)$$

where in addition to $\not{p} u(p) = m u(p)$ we have now used the property of the γ -matrices that $(\gamma \cdot p)(\gamma \cdot \epsilon^*) = 2(p \cdot \epsilon^*) - (\gamma \cdot \epsilon^*)(\gamma \cdot p)$. We get for particle-particle scattering $\chi_F \chi_F \rightarrow \chi_F \chi_F V$

$$\begin{aligned} |\mathcal{F}|^2 &= g^2 \left(\frac{(p_3 \cdot \epsilon)}{(p_3 \cdot q)} + \frac{(p_4 \cdot \epsilon)}{(p_4 \cdot q)} - \frac{(p_1 \cdot \epsilon)}{(p_1 \cdot q)} - \frac{(p_2 \cdot \epsilon)}{(p_2 \cdot q)} \right)^2 \\ &= \frac{2}{9} \frac{g^2}{m^4 \omega^2} |\vec{k}|^2 |\vec{l}|^2 \left(1 + 3(\hat{k} \cdot \hat{l})^2 \right) \end{aligned} \quad (3.74)$$

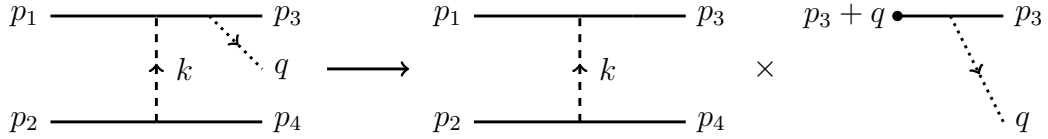
and for particle-antiparticle scattering $\chi_F \bar{\chi}_F \rightarrow \chi_F \bar{\chi}_F V$

$$|\mathcal{F}|^2 = g^2 \left(\frac{(p_3 \cdot \epsilon)}{(p_3 \cdot q)} - \frac{(p_4 \cdot \epsilon)}{(p_4 \cdot q)} - \frac{(p_1 \cdot \epsilon)}{(p_1 \cdot q)} + \frac{(p_2 \cdot \epsilon)}{(p_2 \cdot q)} \right)^2 \quad (3.75)$$

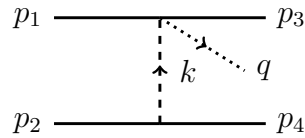
$$= \frac{8}{3} \frac{g^2}{m^4 \omega^4} |\vec{k}|^4 |\vec{l}|^2 (\hat{k} \cdot \hat{l})^2$$

yielding the same results for the squared matrix element as (3.24) and (3.29). It is noteworthy, that (3.74) and (3.75) are gauge invariant, as expected, since a gauge transformation $\epsilon \rightarrow \epsilon + q$ only yields trivial factors of 1 which cancel in the sum, as can easily be checked.

For scalar boson scattering, this factorization is not possible due to the diagrams (e) and (f) in Fig. 3.6 because these diagrams do not contain an internal fermion line. The factorization can be explained in terms of Feynman diagrams as cutting the diagram in two pieces at the fermion propagator, *i.e.*,



where for the factorization it is essential that $p_3 + q \approx p_3$. This internal propagator is not present in the diagrams of scalar boson scattering, where the bremsstrahlung is emitted directly at the vertex, *i.e.*,



and therefore these diagrams don't allow for a factorization of the cross section.

Effects of Dissipation on Structure Formation

In order to estimate the relevance of the energy loss due to bremsstrahlung during structure formation, in this chapter we will compare the typical time scale of the cooling process due to dissipation t_{cool} to the time scale of the gravitational collapse t_{grav} of a cloud of particles, as well as to the Hubble time t_0 and the time between two elastic scattering events t_{el} .

As mentioned in Chap. 2, matter over-densities in the early universe get amplified. Over-dense patches in the universe expand slower than the Hubble rate because of their internal gravitational attraction and eventually stop expanding and, for the general solution of the spherical collapse model (2.12), *i.e.*,

$$r = A(1 - \cos \theta) \quad t = B(\theta - \sin \theta)$$

with $B = \sqrt{A^3/GM}$, start collapsing at a turnaround time $t_{\text{turn}} = \pi B = \pi\sqrt{A^3/GM}$. Following [13, p.733ff] and [14, p.215ff], we approximate the time it takes for a halo to virialize as $t_{\text{grav}} = 2t_{\text{turn}}$. Assuming a spherically symmetric density distribution, we get a turnaround radius $r_{\text{turn}} = 2A$ and with $M = 4\pi r^3 \rho / 3$ estimate a gravitational collapse time of

$$t_{\text{grav}} = \sqrt{\frac{3\pi}{8m_\chi n_\chi G}}. \quad (4.1)$$

If the gravitational time scale is larger than the cooling time due to dissipation [13,

p.764]

$$t_{\text{cool}} = \frac{3n_{\chi}T}{\dot{\epsilon}} \quad (4.2)$$

which is the ratio of the thermal energy content and the energy loss rate, we concede that the energy loss due to bremsstrahlung has major effects on the gravitational collapse of gas clouds in the universe. However, if $t_{\text{grav}} < t_{\text{cool}} < t_0$, *i.e.* the cooling time is smaller than the age of the universe, cooling can still have an impact on structure formation. We want to analyze the parameter space where structure formation is influenced by dissipation due to bremsstrahlung. For that reason we define two regions of interest, *i.e.*

$$t_{\text{cool}} < t_0 \quad \Rightarrow \quad \frac{3n_{\chi}T}{\dot{\epsilon}} < H_0^{-1} \quad (4.3)$$

and the more extreme region

$$t_{\text{cool}} < t_{\text{grav}} \quad \Rightarrow \quad \frac{3n_{\chi}T}{\dot{\epsilon}} < \sqrt{\frac{3\pi}{8m_{\chi}n_{\chi}G}}. \quad (4.4)$$

For $\dot{\epsilon}$ in (4.2) we substitute the energy loss rates calculated in Chap. 3. Keeping in mind that dark matter self-interactions were introduced to solve the cusp vs. core problem via heat transfer due to elastic dark matter scattering, we define an elastic scattering timescale

$$t_{\text{el}} = (n_{\chi}\sigma_T v_{\text{vir}})^{-1} \quad (4.5)$$

where the transport¹ cross section σ_T is evaluated at v_{vir} . The small structure problems can be solved if

$$t_{\text{el}} < t_0 \quad \Rightarrow \quad (n_{\chi}\sigma_T v_{\text{vir}})^{-1} < H_0^{-1}. \quad (4.6)$$

Using t_{el} we can try to find a region where elastic scattering could solve the small structure problems, but dissipative effects are dominant preventing the solution, *i.e.*, $t_{\text{cool}} < t_{\text{el}} < t_0$. As it turns out, this condition is not reachable with a coupling $\alpha < 1$

¹The reader should be aware that in this chapter, for the sake of simplicity, the regularized cross section will be referred to as transport cross section σ_T , when in fact we distinguish between the transport cross section (3.62a) used for particle-antiparticle scattering and the viscosity cross section (3.62b) used for particle-particle scattering.

in the non-relativistic limit because with $\dot{\epsilon}_{\chi\chi} \sim \alpha^3 n_\chi^2 v_{\text{vir}}^3 / m$ and $\dot{\epsilon}_{\chi\bar{\chi}} \sim \alpha^3 n_\chi^2 v_{\text{vir}} / m$ and $\sigma_T \sim \alpha^2 / (m_\chi v_{\text{vir}})^2$, we find that the cooling time is larger than the elastic scattering time by a factor

$$\chi\chi : \quad \frac{t_{\text{cool}}}{t_{\text{el}}} \sim \frac{1}{\alpha v_{\text{vir}}^4}, \quad (4.7a)$$

$$\chi\bar{\chi} : \quad \frac{t_{\text{cool}}}{t_{\text{el}}} \sim \frac{1}{\alpha v_{\text{vir}}^2}. \quad (4.7b)$$

However, for $t_{\text{el}} < t_{\text{cool}} < t_0$, cooling can still have an influence on structure formation, counteracting the effects of elastic scattering, with heat being transferred to the center of the halo by elastic collisions at first, but on larger timescales $t_{\text{cool}} < t_0$ dissipating the gained thermal energy via bremsstrahlung. Since in all models t_{cool} is a few orders of magnitude larger than t_{el} , we find that (4.6) is always fulfilled in the regions (4.3) and (4.4).

In the following we discuss fermionic dark matter with a gauge interaction. However, the only input for the cooling time that “knows” about particle character and interactions is the energy loss rate $\dot{\epsilon}$. Looking at Tab. 3.1 one realizes that most of the energy loss rates have a temperature dependence of $\dot{\epsilon} \propto T^{3/2}$ with same dependence on the particle mass, coupling and particle density and basically only differ in prefactors which in our heuristic treatment we can neglect. The gauged models yield a different temperature dependence $\dot{\epsilon} \propto T^{1/2}$ for particle-antiparticle scattering. We will therefore analyze $\chi_F \chi_F \rightarrow \chi_F \chi_F V$ representative for all models that yield $\dot{\epsilon} \propto T^{3/2}$ and $\chi_F \bar{\chi}_F \rightarrow \chi_F \bar{\chi}_F V$ for $\dot{\epsilon} \propto T^{1/2}$.

Particle-particle scattering

The energy loss rate for the emission of a massless vector boson as calculated in Chap. 3 is

$$\dot{\epsilon} = \frac{188 - 9\pi^2}{432} \frac{g_V^6 n_\chi^2}{\pi^{7/2} m_\chi^{5/2}} T^{3/2}.$$

Demanding $t_{\text{cool}} \lesssim t_0$, we get

$$T_{\text{vir}} \gtrsim \left(3 \frac{432\pi^{7/2}}{188 - 9\pi^2} \right)^2 H_0^2 m_\chi^5 g_V^{-12} n_\chi^{-2} \quad (4.8a)$$

$$\approx 60 \text{ meV} \quad \left(\frac{0.1}{\alpha} \right)^6 \left(\frac{m_\chi}{10 \text{ MeV}} \right)^7 \left(\frac{\text{GeV/cm}^3}{\rho_\chi} \right)^2, \quad (4.8b)$$

	$t_{\text{cool}} \lesssim t_0$	$t_{\text{cool}} \lesssim t_{\text{grav}}$
DWARF GALAXIES	$m_\chi/\alpha \lesssim 70 \text{ MeV}$	$m_\chi/\alpha \lesssim 10 \text{ MeV}$
GALAXY CLUSTERS	$m_\chi/\alpha \lesssim 300 \text{ MeV}$	$m_\chi/\alpha \lesssim 50 \text{ MeV}$

Table 4.1: Bounds on m_χ/α for particle-particle scattering for the two conditions $t_{\text{cool}} \lesssim t_0$ and $t_{\text{cool}} \lesssim t_{\text{grav}}$. Dwarf galaxies have a virial velocity $v_{\text{vir}} \approx 10 \text{ km/s}$ and galaxy clusters have $v_{\text{vir}} \approx 1000 \text{ km/s}$.

$$v_{\text{vir}} \gtrsim 40 \text{ km/s} \quad \left(\frac{0.1}{\alpha}\right)^3 \left(\frac{m_\chi}{10 \text{ MeV}}\right)^3 \left(\frac{\text{GeV/cm}^3}{\rho_\chi}\right) \quad (4.8c)$$

with $\alpha = g_V^2/4\pi$ for particle-particle scattering and, which tells us that for a particle with 10 MeV and a coupling $\alpha = 0.1$ the condition (4.3) can be fulfilled in the non-relativistic limit for a typical dark matter density $\rho_\chi \sim 1 \text{ GeV/cm}^3$. As one can see in (4.8c), the coupling α and the dark matter mass m_χ appear with the same power. Therefore, we can go to higher masses by increasing the coupling by the same factor, yielding the same virial velocity. Increasing the coupling strength to $\alpha = 0.3$ we can still fulfill (4.3) for 100 MeV particles on cluster scales with $v_\chi \sim 1000 \text{ km/s}$. Due to the linear relation between the dark matter mass and the coupling strength, we combine the two into m_χ/α in Tab. 4.1 showing the values for which $t_{\text{cool}} \lesssim t_0$ and $t_{\text{cool}} \lesssim t_{\text{grav}}$.

For $t_{\text{cool}} \lesssim t_{\text{grav}}$, we get

$$T_{\text{vir}} \gtrsim 24 \left(\frac{432\pi^3}{188 - 9\pi^2}\right)^2 G m_\chi^6 g_V^{-12} n_\chi^{-1} \quad (4.9a)$$

$$\approx 3 \text{ keV} \quad \left(\frac{0.1}{\alpha}\right)^6 \left(\frac{m_\chi}{10 \text{ MeV}}\right)^7 \left(\frac{\text{GeV/cm}^3}{\rho_\chi}\right), \quad (4.9b)$$

$$v_{\text{vir}} \gtrsim 9 \times 10^3 \text{ km/s} \quad \left(\frac{0.1}{\alpha}\right)^3 \left(\frac{m_\chi}{10 \text{ MeV}}\right)^3 \left(\frac{\text{GeV/cm}^3}{\rho_\chi}\right)^{1/2}. \quad (4.9c)$$

This means that in order to fulfill (4.4) for smaller structures we need stronger coupling or smaller masses compared to (4.3). The results are presented for $m_\chi = 10 \text{ MeV}$ and $\alpha = 0.1$ in a contour plot in the ρ, T -plane in Fig. 4.1.

As one can see in the upper plot in Fig. 4.1, for a fixed $\alpha = 0.1$ and DM mass $m_\chi \lesssim 10 \text{ MeV}$ cooling is relevant for structures of galactic scales or larger ($v_{\text{vir}} \gtrsim 10^2 \text{ km/s}$). In order for cooling to influence smaller structures with $v_{\text{vir}} \sim 10 \text{ km/s}$, one would have to go to smaller DM masses $m_\chi \lesssim 5 \text{ MeV}$ or stronger couplings $\alpha \gtrsim 0.2$.

	$t_{\text{cool}} \lesssim t_0$	$t_{\text{cool}} \lesssim t_{\text{grav}}$
DWARF GALAXIES	$m_\chi/\alpha \lesssim 200 \text{ GeV}$	$m_\chi/\alpha \lesssim 30 \text{ GeV}$
GALAXY CLUSTERS	$m_\chi/\alpha \lesssim 30 \text{ GeV}$	$m_\chi/\alpha \lesssim 6 \text{ GeV}$

Table 4.2: Bounds on m_χ/α for particle-antiparticle scattering for the two conditions $t_{\text{cool}} \lesssim t_0$ and $t_{\text{cool}} \lesssim t_{\text{grav}}$. Dwarf galaxies have a virial velocity $v_{\text{vir}} \approx 10 \text{ km/s}$ and galaxy clusters have $v_{\text{vir}} \approx 1000 \text{ km/s}$.

Particle-antiparticle scattering

The energy loss rate for the emission of a massless vector boson for particle-antiparticle scattering as calculated in Chap. 3 is

$$\dot{\epsilon} = \frac{2}{3} \frac{g_V^6 n_\chi^2}{\pi^{7/2} m_\chi^{3/2}} T^{1/2}.$$

Again demanding $t_{\text{cool}} \lesssim t_0$, yields

$$T_{\text{vir}} \lesssim \frac{4}{81\pi^7} H_0^{-2} m_\chi^{-3} g_V^{12} n_\chi^2 \quad (4.10a)$$

$$\approx 1 \text{ MeV} \left(\frac{\alpha}{0.1} \right)^6 \left(\frac{\text{GeV}}{m_\chi} \right)^5 \left(\frac{\rho_\chi}{\text{GeV/cm}^3} \right)^2, \quad (4.10b)$$

$$v_{\text{vir}} \lesssim 2 \times 10^4 \text{ km/s} \left(\frac{\alpha}{0.1} \right)^3 \left(\frac{\text{GeV}}{m_\chi} \right)^3 \left(\frac{\rho_\chi}{\text{GeV/cm}^3} \right) \quad (4.10c)$$

meaning that (4.3) is fulfilled for all non-relativistic particles. It is worth mentioning that, due to the different temperature dependence of particle-antiparticle scattering (*i.e.* $\dot{\epsilon} \propto T^{3/2}$ for $\chi\chi$ and $\dot{\epsilon} \propto T^{1/2}$ for $\chi\bar{\chi}$, as shown in Chap. 3), the conditions (4.3) and (4.4) also show different properties for $\chi\chi$ and for $\chi\bar{\chi}$, *i.e.* in (4.8c) the condition yields a lower bound for T_{vir} and v_{vir} while in (4.10c) it yields upper bounds. This means that for $\chi\chi$ -scattering the cooling due to bremsstrahlung is more relevant for larger structures with higher virial velocities and for $\chi\bar{\chi}$ -scattering it is more relevant for smaller structures. This can also be seen in Fig. 4.1 comparing the shaded regions of the top and bottom plot.

For $t_{\text{cool}} \lesssim t_{\text{grav}}$, we get

$$T_{\text{vir}} \lesssim \frac{3}{162\pi^6} G^{-1} m_\chi^{-4} g_V^{12} n_\chi \quad (4.11a)$$

$$\approx 0.1 \text{ keV} \left(\frac{\alpha}{0.1} \right)^6 \left(\frac{\text{GeV}}{m_\chi} \right)^5 \left(\frac{\rho_\chi}{\text{GeV/cm}^3} \right), \quad (4.11b)$$

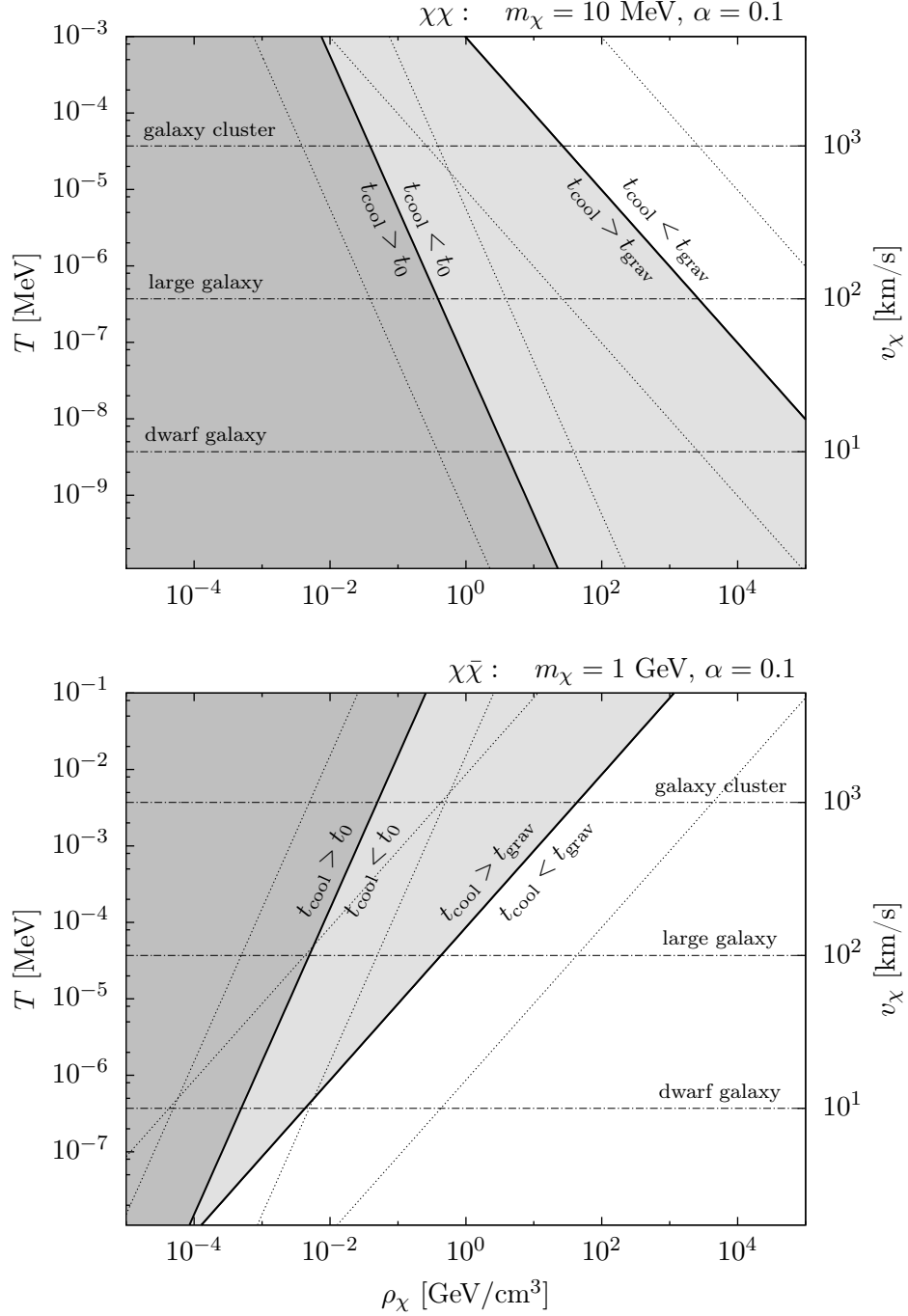


Figure 4.1: Comparison of cooling time t_{cool} with gravitational time t_{grav} and Hubble time t_0 for fermionic dark matter with a massless vector boson. The solid lines denotes the contours where $t_{\text{cool}} = t_{\text{grav}}$ and $t_{\text{cool}} = t_0$ respectively, while the dotted lines are $t_{\text{cool}}/t_{\text{grav}} = 10^{\pm 1}$ and $t_{\text{cool}}/t_0 = 10^{\pm 1}$ in order to give an impression of the magnitudes. In the dark grey region $t_{\text{grav}} < t_0 < t_{\text{cool}}$, in the light grey region $t_{\text{grav}} < t_{\text{cool}} < t_0$ and in the white region $t_{\text{cool}} < t_{\text{grav}} < t_0$. The dashed-dotted lines represent the typical virial velocities of dwarf galaxies, larger galaxies and galaxy clusters. Top: $\chi_F\chi_F \rightarrow \chi_F\chi_F V$ for $m_\chi = 10 \text{ MeV}$ and $\alpha = 0.1$. Bottom: $\chi_F\bar{\chi}_F \rightarrow \chi_F\bar{\chi}_F V$ for $m_\chi = 1 \text{ GeV}$ and $\alpha = 0.1$.

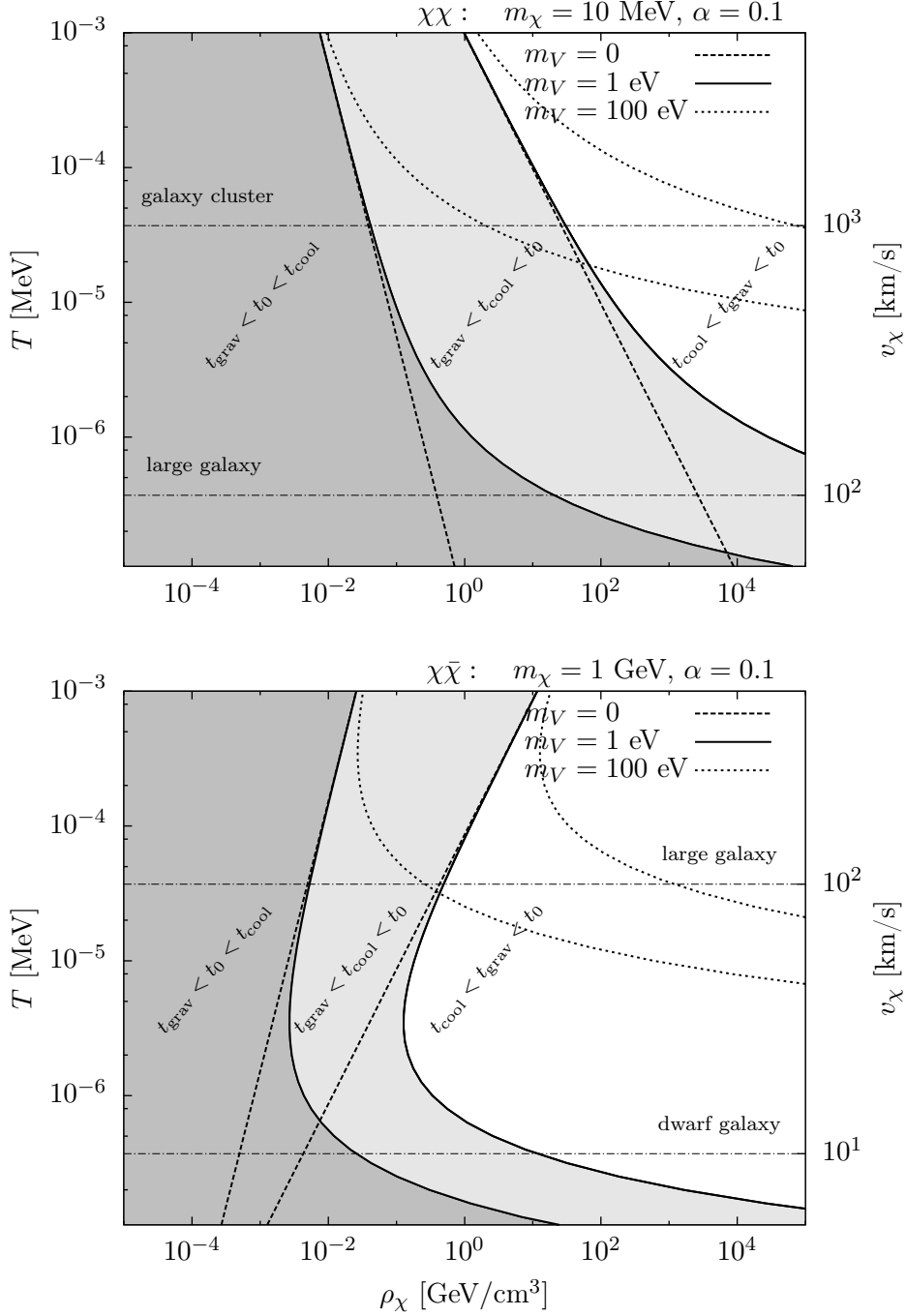


Figure 4.2: Comparison of cooling time t_{cool} with gravitational time t_{grav} and Hubble time t_0 for fermionic dark matter with a massive vector boson. The solid lines denotes the contours where $t_{\text{cool}} = t_{\text{grav}}$ and $t_{\text{cool}} = t_0$ respectively for $m_V = 1$ eV, while the dashed lines denote the contours for $m_V = 0$ from Fig. 4.1 and the dotted lines denote the contours for $m_V = 100$ eV. For $m_V = 1$ eV, in the dark grey region $t_{\text{grav}} < t_0 < t_{\text{cool}}$, in the light grey region $t_{\text{grav}} < t_{\text{cool}} < t_0$ and in the white region $t_{\text{cool}} < t_{\text{grav}} < t_0$. The dashed-dotted lines represent the typical virial velocities of dwarf galaxies, larger galaxies and galaxy clusters. Top: $\chi_F\chi_F \rightarrow \chi_F\chi_F V$ for $m_\chi = 10$ MeV, $\alpha = 0.1$. Bottom: $\chi_F\bar{\chi}_F \rightarrow \chi_F\bar{\chi}_F V$ for $m_\chi = 1$ GeV, $\alpha = 0.1$.

$3T/m_V$	$x(T; m_V)$	$3T/m_V$	$x(T; m_V)$
0.01	$\approx 10^{-29}$	1	$\approx 10^{-2}$
0.1	$\approx 10^{-15}$	10^1	≈ 0.5
0.3	$\approx 10^{-6}$	10^2	≈ 0.9
0.6	$\approx 10^{-3}$	10^3	≈ 1

Table 4.3: Suppression factors of the energy loss rate as a function of the temperature and mediator mass for fermionic dark matter with a gauge coupling.

$$v_{\text{vir}} \lesssim 150 \text{ km/s} \left(\frac{\alpha}{0.1} \right)^3 \left(\frac{\text{GeV}}{m_\chi} \right)^3 \left(\frac{\rho_\chi}{\text{GeV/cm}^3} \right)^{1/2} \quad (4.11c)$$

for particle-antiparticle scattering. In Tab. 4.2 we show the values of m_χ/α for which $t_{\text{cool}} \lesssim t_0$ and $t_{\text{cool}} \lesssim t_{\text{grav}}$ for particle-antiparticle scattering.

For a finite mass of the vector boson $m_V > 0$, the energy loss rate gets suppressed by a factor $x(T, m_V) < 1$ compared to the massless case, *i.e.*,

$$\dot{\epsilon}(T, m_V) = x(T, m_V) \dot{\epsilon}(T, m_V = 0) \quad (4.12)$$

as can be seen, *e.g.*, in Fig. 3.4. This leads to the lower bounds for T_{vir} in (4.8b) and (4.9b) being increased and the upper bounds for T_{vir} in (4.10b) and (4.11b) being decreased by the square of the suppression factor, leading to the implicit equations

$$T_{\text{vir}}^{\chi\chi}(m_V) = x^{-2}(T_{\text{vir}}^{\chi\chi}(m_V), m_V) T_{\text{vir}}^{\chi\chi}(m_V = 0), \quad (4.13)$$

$$T_{\text{vir}}^{\chi\bar{\chi}}(m_V) = x^2(T_{\text{vir}}^{\chi\bar{\chi}}(m_V), m_V) T_{\text{vir}}^{\chi\bar{\chi}}(m_V = 0). \quad (4.14)$$

In order to make a quick comparison possible, we present a few values of $x(T, m_V)$ in Tab. 4.3. One can see, as described in more detail in Chap. 3, that for high temperatures x is almost independent of m_V . However, when the kinetic energy of the system $m_\chi v_\chi^2 = 3T_{\text{vir}}$ drops below m_V , x decreases exponentially. We present in Fig. 4.2 how the contours in the ρ, T -plane change with increasing mediator mass. As expected, the contours $t_{\text{cool}} = t_0$ and $t_{\text{cool}} = t_{\text{grav}}$ for $m_V > 0$ deviate visibly from the contours for $m_V = 0$ when the temperature sinks below the mass of the emitted particle. While for high temperatures the contours are given by a power law $T \propto \rho_\chi^k$, for low temperatures the contours flatten out as $T \exp(T/m_V) \propto \rho_\chi^k$. This yields stringent lower bounds on the temperature ($3T \gtrsim m_V$) in order for cooling to influence structure formation.

It is important to analyze the parameter space where our approximations hold. It is

constrained for high temperatures (*i.e.* from above in Fig. 4.1) by the border of the non-relativistic limit

$$\frac{3T}{m_\chi} \simeq 1 \quad (4.15)$$

and for low temperatures and high densities by the border of the non-degenerate limit where the inter-particle distance $r_{\text{int}} \approx (4\pi\rho_\chi/3m_\chi)^{-1/3}$ becomes comparable to the de-Broglie wavelength $\lambda \approx (3m_\chi T)^{-1/2}$ of the particles

$$\frac{243}{16\pi^2} \rho_\chi^{-2} m_\chi^5 T^3 \simeq 1 \quad (4.16)$$

whereas these limits depend on the DM mass m_χ which in Fig. 4.1 is taken to be 10 MeV for $\chi\chi$ and 1 GeV for $\chi\bar{\chi}$. For increasing m_χ the region of validity gets broader and for decreasing m_χ it gets narrower. However, in the region depicted in the figures in this chapter, our approximation of a non-degenerate, non-relativistic gas of particles is well justified.

It is possible to do the same analysis as the above in terms of the mass of the halo M and the redshift z at which it was formed instead of the virial temperature and density, using the fact from Sec. 2.2, that the density of a halo after virialization is

$$\rho_M^{\text{vir}} = \rho_\chi^{\text{vir}} + \rho_b^{\text{vir}} = 18\pi^2 \bar{\rho}_M = 18\pi^2 \rho_M^0 (1+z)^3 = 18\pi^2 \Omega_M^0 \rho_c^0 (1+z)^3 \quad (4.17)$$

where $\rho_c^0 \approx 0.47 \times 10^{-5} \text{ GeV/cm}^3$ is the current critical density of our universe defined in (2.5), $\Omega_M^0 \approx 0.3$ the normalized matter density and the factor $(1+z)^3$ stems from the fact that the matter density scales with a^{-3} . Approximating $\rho_M^{\text{vir}} \approx \rho_\chi^{\text{vir}}$ allows us to calculate contours in the z, M -plane. Using (2.21) and (4.17) and assuming for the halo a homogeneous sphere $r_{\text{vir}}^3 = 3M/(4\pi\rho_\chi^{\text{vir}})$ we get

$$T_{\text{vir}} = \left(\frac{24\pi^3}{125} M^2 \Omega_M^0 \rho_c^0 \right)^{1/3} G m_\chi (1+z). \quad (4.18)$$

This yields for particle-particle scattering for the condition $t_{\text{cool}} \lesssim t_0$

$$M \gtrsim 4 \times 10^4 \text{ M}_\odot \left(\frac{0.5}{\alpha} \right)^9 \left(\frac{m_\chi}{10 \text{ MeV}} \right)^9 \left(\frac{10}{1+z} \right)^{21/2} \quad (4.19)$$

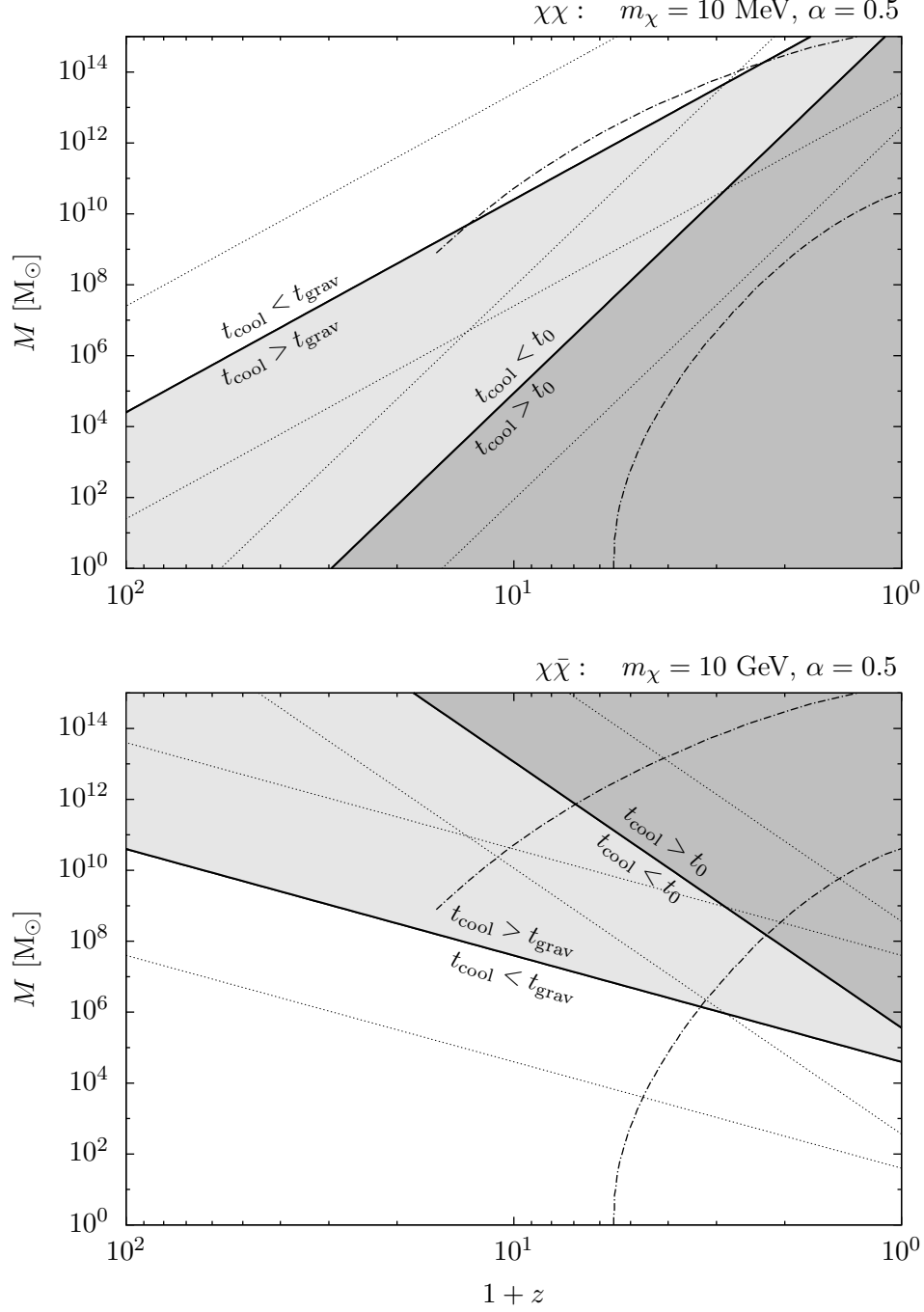


Figure 4.3: Comparison of cooling time t_{cool} with gravitational time t_{grav} and Hubble time t_0 for fermionic dark matter with a massless vector boson. The solid lines denote the contour where $t_{\text{cool}} = t_{\text{grav}}$ and $t_{\text{cool}} = t_0$ respectively, while the dotted lines are $t_{\text{cool}}/t_{\text{grav}} = 10^{\pm 1}$ and $t_{\text{cool}}/t_0 = 10^{\pm 1}$ lines in order to give an impression of the magnitudes. In the dark grey region $t_{\text{grav}} < t_0 < t_{\text{cool}}$, in the light grey region $t_{\text{grav}} < t_{\text{cool}} < t_0$ and in the white region $t_{\text{cool}} < t_{\text{grav}} < t_0$. The dashed-dotted lines enclose the halo mass range based on Press-Schechter theory in Λ CDM, which is also depicted in Fig. 2.4 [16]. Top: $\chi_F\chi_F \rightarrow \chi_F\chi_F V$ for $m_\chi = 10 \text{ MeV}$ and $\alpha = 0.5$. Bottom: $\chi_F\bar{\chi}_F \rightarrow \chi_F\bar{\chi}_F V$ for $m_\chi = 10 \text{ GeV}$ and $\alpha = 0.5$.

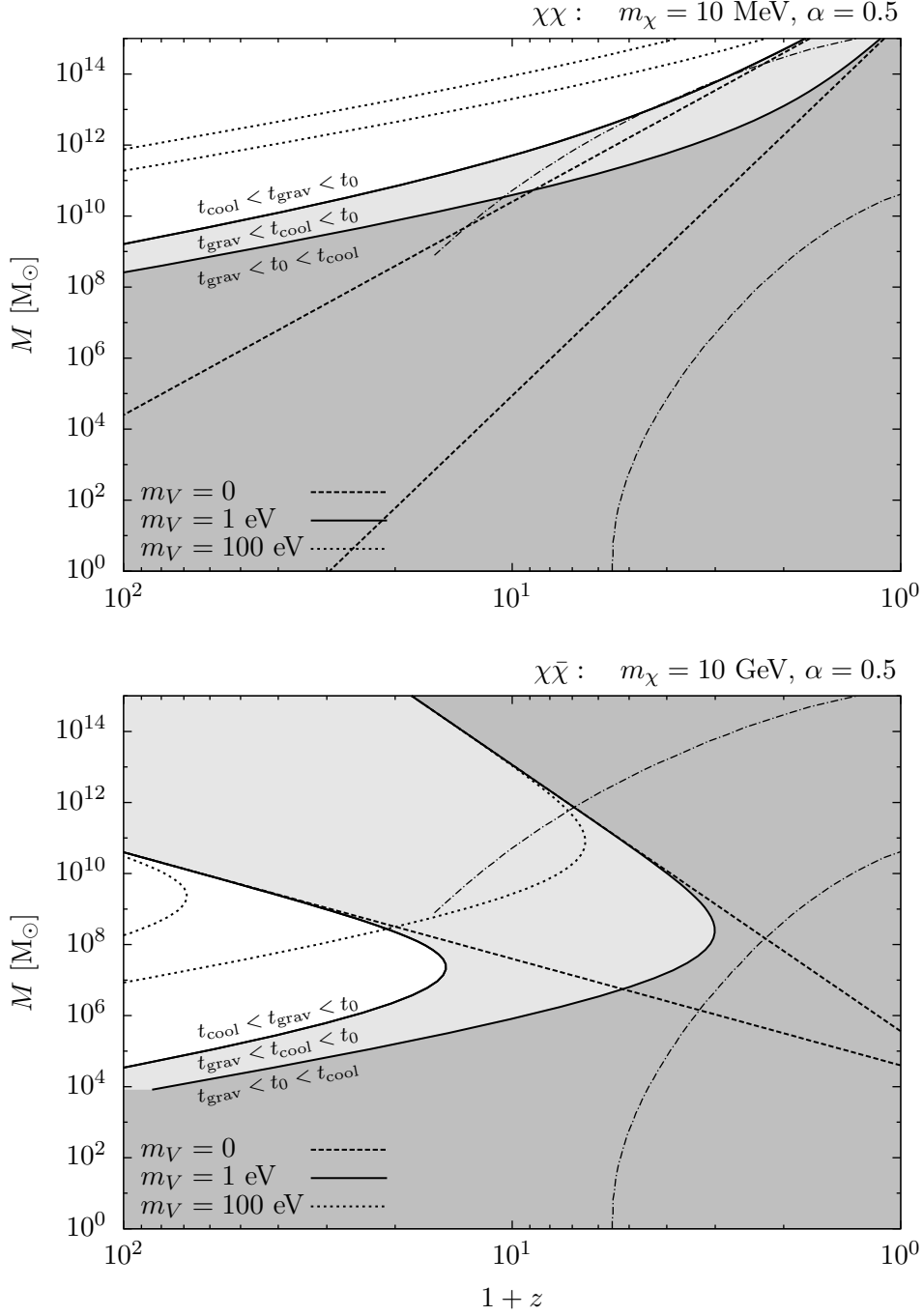


Figure 4.4: Comparison of cooling time t_{cool} with gravitational time t_{grav} and Hubble time t_0 for fermionic dark matter with a massless vector boson. The solid lines denote the contours where $t_{\text{cool}} = t_{\text{grav}}$ and $t_{\text{cool}} = t_0$ respectively for $m_V = 1 \text{ eV}$, while the dashed lines denote the contours for $m_V = 0$ from Fig. 4.1 and the dotted lines denote the contours for $m_V = 100 \text{ eV}$. For $m_V = 1 \text{ eV}$, in the dark grey region $t_{\text{grav}} < t_0 < t_{\text{cool}}$, in the light grey region $t_{\text{grav}} < t_{\text{cool}} < t_0$ and in the white region $t_{\text{cool}} < t_{\text{grav}} < t_0$. The dashed-dotted lines enclose the halo mass range based on Press-Schechter theory in ΛCDM , which is also depicted in Fig. 2.4 [16]. Top: $\chi_F\chi_F \rightarrow \chi_F\chi_F V$ for $m_\chi = 10 \text{ MeV}$ and $\alpha = 0.5$. Bottom: $\chi_F\bar{\chi}_F \rightarrow \chi_F\bar{\chi}_F V$ for $m_\chi = 10 \text{ GeV}$ and $\alpha = 0.5$.

and for $t_{\text{cool}} \lesssim t_{\text{grav}}$

$$M \gtrsim 8 \times 10^{10} \text{ M}_{\odot} \quad \left(\frac{0.5}{\alpha}\right)^9 \left(\frac{m_{\chi}}{10 \text{ MeV}}\right)^9 \left(\frac{10}{1+z}\right)^6. \quad (4.20)$$

For particle-antiparticle scattering, we get for $t_{\text{cool}} \lesssim t_0$

$$M \lesssim 2 \times 10^{13} \text{ M}_{\odot} \quad \left(\frac{\alpha}{0.5}\right)^9 \left(\frac{10 \text{ GeV}}{m_{\chi}}\right)^9 \left(\frac{1+z}{10}\right)^{15/2} \quad (4.21)$$

and for $t_{\text{cool}} \lesssim t_{\text{grav}}$

$$M \lesssim 5 \times 10^7 \text{ M}_{\odot} \quad \left(\frac{\alpha}{0.5}\right)^9 \left(\frac{10 \text{ GeV}}{m_{\chi}}\right)^9 \left(\frac{1+z}{10}\right)^3. \quad (4.22)$$

Again, $\chi\chi$ and $\chi\bar{\chi}$ show a different analytical structure due to the analytical structure of the energy loss rate. The results for a massless vector boson are presented in a contour plot in the z, M -plane in Fig. 4.3, together with the halo mass range [16] (which has been presented in Fig. 2.4). One can see in Fig. 4.3 that for particle-particle scattering and the given parameters $m_{\chi} = 10 \text{ MeV}$ and $\alpha = 0.5$, almost all relevant masses within the halo mass range (depicted by the dashed-dotted line) are within the region $t_{\text{grav}} < t_{\text{cool}} < t_0$. The contours of the time scales as well as the halo mass function all go from small masses at large redshift to large masses at small redshift. Only for a narrow region of large halo masses within the halo mass range the condition $t_{\text{cool}} < t_{\text{grav}}$ is fulfilled. For particle-antiparticle scattering and the parameters $m_{\chi} = 10 \text{ GeV}$ and $\alpha = 0.5$, the $t_{\text{cool}} < t_0$ and $t_{\text{cool}} < t_{\text{grav}}$ contours are perpendicular to the contours of the halo mass function in the z, M -plane, meaning that radiative cooling becomes more important for smaller structures that were formed at larger redshift.

In Fig. 4.4, we present how the contours in the z, M -plane change with increasing mediator mass. For particle-particle scattering the region of interest is pushed to higher masses within the halo mass range for a very light mediator $m_V = 1 \text{ eV}$ while for a heavier mediator $m_V = 100 \text{ eV}$ the region of interest does not lie within the halo mass range anymore (see Fig 4.4, top). In the latter case, one would have to increase the coupling in order for cooling to influence any of the structures within the halo mass range. For particle-antiparticle scattering, cooling is dominant for small masses if $m_V = 0$, yielding $t_{\text{cool}} < t_{\text{grav}}$ for all structures below $\sim 10^7 \text{ M}_{\odot}$ (see Fig 4.3, bottom) which would have drastic consequences for small structures. However, this region gets pushed to higher masses and larger redshift and thereby almost entirely out of the halo

mass range for $m_V = 1$ eV and even further out for $m_V = 100$ eV (see Fig 4.4, bottom). Having shown that the condition $t_{\text{el}} < t_{\text{cool}} < t_0$ or even $t_{\text{el}} < t_{\text{cool}} < t_{\text{grav}}$ can be met with reasonable parameters, we now want to analyze in more detail the parameter space that fulfills the observational constraint

$$\frac{\sigma_T}{m_\chi} \lesssim 1 \text{ cm}^2/\text{g} \quad (4.23)$$

from gravitational lensing measurements of the Bullet cluster [32]. Using (4.7), yields for the condition $t_{\text{cool}} < t_0$

$$\rho_\chi > \frac{m_\chi}{\sigma_T} \frac{H_0}{\alpha v_{\text{vir}}^{2k+1}} \quad (4.24)$$

with $k = 1$ for particle-antiparticle and $k = 2$ for particle-particle scattering. With (4.23) and a typical virial velocity $v \sim 10^{-2}$ at cluster scales we get a lower bound for the density

$$\chi\chi : \quad \rho_\chi \gtrsim \frac{10^6}{\alpha} \text{ GeV/cm}^3 \left(\frac{10^{-2}}{v_\chi} \right)^5, \quad (4.25a)$$

$$\chi\bar{\chi} : \quad \rho_\chi \gtrsim \frac{10^2}{\alpha} \text{ GeV/cm}^3 \left(\frac{10^{-2}}{v_\chi} \right)^3 \quad (4.25b)$$

and, putting (3.66) into (4.23), a lower bound for the DM mass

$$m_\chi \gtrsim 10 \alpha^{3/2} \text{ GeV} \left(\frac{10^{-2}}{v_\chi} \right)^{4/3}. \quad (4.26)$$

Equations (4.25) and (4.26) show that the conditions $t_{\text{el}} < t_0$ and $t_{\text{cool}} < t_0$ cannot be met simultaneously for the fiducial DM density $\rho_\chi \sim 1 \text{ GeV/cm}^3$ which is approximately the DM density in our local group. However, if the DM density increases by a few orders of magnitude and the DM mass is in the GeV range or higher, which are still reasonable numbers, it is possible to fulfill $t_{\text{el}} < t_{\text{cool}} < t_0$ entering a regime where the small structure problems are solved by elastic scattering while bremsstrahlung is prevalent enough for dissipative cooling to influence structure formation.

It is important to mention that the results obtained in this thesis are based on tree level calculations (*i.e.* the Born approximation) requiring, for a heavy mediator, that $\alpha m_\chi/m_V \ll 1$ [32]. For a light mediator, this becomes a condition for the coupling and the DM velocity $\alpha/v_\chi \ll 1$ [33, p. 323]. The second condition is relevant for

bremsstrahlung where the mediator has to be light in order for it to be produced in non-relativistic collisions. In the parameter space analyzed in this chapter, the Born condition is not always fulfilled which would lead to non-perturbative effects. However, the non-perturbative effects for the elastic scattering cross section can, to a good approximation, be factorized into a Sommerfeld enhancement factor times the tree level results [32]. If this also holds true for the energy loss rate in inelastic scattering and the energy loss rate gets enhanced by approximately the same factor as the elastic scattering cross section, the regions of interest for ρ_χ in (4.25) and m_χ in (4.26) stay intact.

Conclusions and Outlook

In this thesis, the effects of bremsstrahlung in dark matter collisions on structure formation in the universe were analyzed. For this purpose, four different generic models of self-interacting dark matter were assumed, including fermionic and scalar dark matter with the self-interaction being mediated by either scalar or vector bosons.

Following these simple models, the energy radiated away in form of bremsstrahlung (*i.e.* the energy loss rate $\dot{\epsilon}$) was calculated perturbatively in a non-relativistic and non-degenerate limit. Systems with a vanishing dipole moment show a different temperature dependence of the energy loss rate than systems with a non-vanishing dipole moment. It was found that $\dot{\epsilon} \propto T_{\text{vir}}^{1/2}$ for particle-antiparticle scattering in the gauged models (*i.e.*, for the processes $\chi_F \bar{\chi}_F \rightarrow \chi_F \bar{\chi}_F V$ and $\chi_S \chi_S^\dagger \rightarrow \chi_S \chi_S^\dagger V$) and $\dot{\epsilon} \propto T_{\text{vir}}^{3/2}$ in all other models that were analyzed for vanishing masses of the mediator m_m and the emitted particle m_e . While for vanishing masses the energy loss rates were solved analytically, for finite masses numerical methods were used to solve the phase space integrals. It was found that the energy loss rate is independent of m_m and m_e for $T_{\text{vir}} \gg m_m$ and $T_{\text{vir}} \gg m_e$. When the kinetic energy of the system $m_\chi v_{\text{vir}}^2 = 3T_{\text{vir}} = m_m = m_e$, the energy loss rate is suppressed by approximately a factor 0.01 and drops exponentially for lower temperatures. This can be explained by the fact that the mass of the emitted particle has to be “drawn” from the kinetic energy of the system and therefore its production becomes more unlikely when the temperature decreases.

The energy loss rates obtained in the perturbative calculations were used to calculate the cooling time t_{cool} , *i.e.*, the time it takes a gas with a given thermal energy content to cool down through radiative dissipation. The cooling time was compared to the Hubble time t_0 (*i.e.* approximately the age of the universe), the gravitational time scale t_{grav} (*i.e.* the time it takes a spherical over-density to contract and virialize) and the elastic

scattering time t_{el} (*i.e.* the average time between two elastic scattering events). It was found that $t_{\text{cool}}/t_{\text{el}} \propto \alpha^{-2}$ and therefore a coupling $\alpha < 1$ always leads to t_{cool} being larger than t_{el} . Considering that $t_{\text{grav}} < t_0$, cooling due to dissipation can have an effect on structure formation if $t_{\text{cool}} < t_0$ and even greater effects if $t_{\text{cool}} < t_{\text{grav}}$. Both conditions can be met for certain ratios of the dark matter mass m_χ and the coupling constant of the self-interaction α for a fiducial dark matter density of 1 GeV/cm^3 . For these regions of interest, the condition $t_{\text{el}} < t_0$ is always fulfilled which is a prerequisite for SIDM solving the small structure problems. The scenario of fermionic dark matter with the emission of a massless vector boson was treated as a representative case.

For particle-particle scattering, the condition $t_{\text{cool}} < t_0$ can be met for $m_\chi/\alpha \lesssim 70 \text{ MeV}$ in small structures like dwarf galaxies with a virial velocity of a few dozen km/s and for up to $m_\chi/\alpha \lesssim 300 \text{ MeV}$ for large galaxy clusters with virial velocities of 1000 km/s. This means that for particles with a mass in the MeV range, the self-interaction has to be very strong in order for radiative cooling to influence structure formation in the universe, while for lighter particles weaker interactions are possible. For particle-antiparticle scattering, the condition $t_{\text{cool}} < t_0$ yields looser bounds on m_χ/α , *i.e.* in dwarf galaxies the condition can be met by $m_\chi/\alpha \lesssim 200 \text{ GeV}$ while large galaxy clusters require $m_\chi/\alpha \lesssim 30 \text{ GeV}$. Both processes, $\chi\chi \rightarrow \chi\chi V$ and $\chi\bar{\chi} \rightarrow \chi\bar{\chi} V$, yield upper bounds on the dark matter mass, but for fixed mass and coupling the $\chi\chi$ -process is more relevant for larger structures while the $\chi\bar{\chi}$ -process is more relevant for smaller structures. Since the energy loss rate is suppressed by the mediator and the emitted particle's mass, the parameter space where radiative cooling can influence structure formation gets bounded from below by the condition $3T = m_\chi v_\chi^2 \gtrsim m_V$.

Considering the observational constraint $\sigma_T/m_\chi \lesssim 1 \text{ cm}^2/\text{g}$ at cluster scales of $v_\chi \sim 10^{-2}$, it was found that $t_{\text{el}} < t_{\text{cool}} < t_0$ can only be fulfilled if $m_\chi/\alpha^{3/2} \gtrsim 10 \text{ GeV}$ with dark matter densities $\alpha \rho_\chi \gtrsim 10^6 \text{ GeV/cm}^3$ for $\chi\chi$ -scattering and $\alpha \rho_\chi \gtrsim 10^2 \text{ GeV/cm}^3$ for $\chi\bar{\chi}$ -scattering.

The results presented in this thesis are all based on perturbative calculations. However, especially for non-relativistic collisions and light mediators non-perturbative effects gain significance [32]. These lead to a ‘‘Sommerfeld enhancement’’ of the cross section, which would also lead to an enhancement in the energy loss rate. This enhancement could possibly reduce t_{cool} by orders of magnitude and thereby loosen the bounds on the parameter space where radiative cooling is a significant factor for structure formation in the universe. For elastic scattering, to a good approximation, the non-perturbative effects can be factorized into a Sommerfeld enhancement factor times the tree level

results. If this also holds true for inelastic scattering, the results obtained in this thesis are an important basis for further investigations. Finally, the presented toy-models of dark matter should be studied in the broader context of cosmological and experimental viability.

Appendix

A.1 Massive $U(1)$ Gauge Field

In this appendix, we comment on the mass of $U(1)$ gauge fields. The most general Lagrangian for interacting fermions χ , gauged under a massless $U(1)$ vector boson is given by

$$\begin{aligned}\mathcal{L}_{QED} &= \bar{\chi}(i\not{D} - m_\chi)\chi - \frac{1}{4}V_{\mu\nu}V^{\mu\nu} \\ &= i\bar{\chi}\not{\partial}\chi - m_\chi\bar{\chi}\chi - \frac{1}{4}V_{\mu\nu}V^{\mu\nu} + g_V V_\mu \bar{\chi}\gamma^\mu\chi\end{aligned}\tag{A.1}$$

with the field strength tensor $V_{\mu\nu} = \partial_\mu V_\nu - \partial_\nu V_\mu$ and the covariant derivative $D_\mu = \partial_\mu - ig_V V_\mu$. This Lagrangian is invariant under the gauge transformations

$$V^\mu \rightarrow V'^\mu = V^\mu + \frac{1}{g_V}\partial^\mu\Lambda,\tag{A.2a}$$

$$\chi \rightarrow \chi' = e^{-i\Lambda}\chi\tag{A.2b}$$

where $\Lambda = \Lambda(x)$ is the gauge parameter. If we want to add a mass term to \mathcal{L}_{QED} , we realize that the theory is not gauge invariant anymore because

$$\frac{1}{2}m_V^2 V^2 \rightarrow \frac{1}{2}m_V^2 V'^2 = \frac{1}{2}m_V^2 V^2 + \frac{m_V^2}{2g_V^2}\partial_\mu\Lambda\partial^\mu\Lambda + \frac{m_V^2}{g_V}V^\mu\partial_\mu\Lambda.\tag{A.3}$$

Gauge invariance can be restored by the Stueckelberg trick [34], as sketched in the following. The starting point is to add a mass term to the Lagrangian of a massless

vector boson $-\frac{1}{4}V_{\mu\nu}V^{\mu\nu}$. This yields the Proca Lagrangian of a massive vector boson,

$$\mathcal{L}_P = -\frac{1}{4}V_{\mu\nu}V^{\mu\nu} + \frac{1}{2}m_V^2 V^2. \quad (\text{A.4})$$

The equations of motion following from this Lagrangian are

$$\partial_\mu V^{\mu\nu} + m_V^2 V^\nu = 0. \quad (\text{A.5})$$

After differentiation with respect to x^ν we realize that the Lorentz condition

$$\partial_\nu V^\nu = 0, \quad (\text{A.6})$$

restricting the gauge invariance, is manifestly satisfied in the Proca Lagrangian. The restriction can be lifted by adding to the Lagrangian a Lagrange multiplier $[-\frac{1}{2\xi}(\partial_\mu V^\mu)^2]$ with $\xi = 1$ to subtract the gauge condition. This leaves us with the Lagrangian

$$\mathcal{L} = -\frac{1}{2}\partial_\mu V_\nu \partial^\mu V^\nu + \frac{1}{2}m_V^2 V^2. \quad (\text{A.7})$$

where the Lorentz condition does not follow from the equations of motions. However, this has the consequence that the Hamiltonian is not positive definite anymore [34] and the Lagrangian is still not gauge invariant. Stueckelberg showed in 1938 that one gets a gauge invariant Lagrangian with positive definite Hamiltonian by introducing a new scalar field B , known as the Stueckelberg field, with the Lagrangian

$$\mathcal{L}_B = \frac{1}{2}(\partial_\mu B)^2 - \frac{1}{2}m_V^2 B^2. \quad (\text{A.8})$$

The full Stueckelberg Lagrangian

$$\begin{aligned} \mathcal{L}_{\text{St}} &= \mathcal{L}_P - \frac{1}{2}(\partial_\mu V^\mu)^2 + \mathcal{L}_B \\ &= -\frac{1}{2}\partial_\mu V_\nu \partial^\mu V^\nu + \frac{1}{2}m_V^2 V^2 + \frac{1}{2}(\partial_\mu B)^2 - \frac{1}{2}m_V^2 B^2 \end{aligned} \quad (\text{A.9})$$

fulfills a new gauge invariance

$$V^\mu \rightarrow V'^\mu = V^\mu + \frac{1}{g_V} \partial^\mu \Lambda \quad (\text{A.10a})$$

$$B \rightarrow B' = B + \frac{1}{g_V} m_V \Lambda \quad (\text{A.10b})$$

which becomes apparent if we rewrite (A.9) to get

$$\begin{aligned}\mathcal{L}_{\text{St}} = & -\frac{1}{4}V_{\mu\nu}V^{\mu\nu} + \frac{1}{2}m_V^2\left(V_\mu - \frac{1}{m_V}\partial_\mu B\right)\left(V^\mu - \frac{1}{m}\partial^\mu B\right) \\ & - \frac{1}{2}\left(\partial_\mu V^\mu + m_V B\right)\left(\partial_\nu V^\nu + m_V B\right).\end{aligned}\quad (\text{A.11})$$

Interestingly, the Stueckelberg field B is decoupled from the vector boson V^μ , *i.e.* there are no terms in (A.9) through which B and V^μ interact, meaning that we do not have to consider the Stueckelberg field in our calculations.

The Stueckelberg mechanism can be seen as a limit of the Abelian Higgs mechanism (see, *e.g.* [35] or [28]) where the vacuum expectation value of the Higgs field is taken to infinity while the gauge coupling is taken to zero. In the Abelian Higgs mechanism we introduce a complex scalar field ϕ with Lagrangian

$$\mathcal{L}_\phi = (\partial_\mu \phi)^\dagger (\partial^\mu \phi) - \mu^2 \phi^\dagger \phi - \frac{1}{4}\lambda(\phi^\dagger \phi)^2 \quad (\text{A.12})$$

which couples to the vector boson via a gauge coupling $D_\mu \phi = \partial_\mu \phi - igV_\mu \phi$. After symmetry breaking and expanding around the minimum of the potential, we get the Higgs Lagrangian

$$\mathcal{L}_{\text{Higgs}} = \underbrace{\frac{1}{2}g^2v^2V^2}_{\text{gauge field}} + \underbrace{\frac{1}{2}(\partial_\mu h)^2 - \lambda v^2h^2}_{\text{massive scalar}} + \underbrace{g^2vV^2h + \frac{1}{2}g^2V^2h^2}_{h - V^\mu \text{ interaction}} - \underbrace{\lambda vh^3 - \frac{1}{4}\lambda h^4}_{\text{Higgs self-interaction}} \quad (\text{A.13})$$

with v being the vacuum expectation value of ϕ and h the real Higgs field. If we now take the limit $v \rightarrow \infty$ and $g \rightarrow 0$ while keeping $gv = \sqrt{2\lambda}v = m_V$ we get the Stueckelberg Lagrangian with the Stueckelberg field h .

A.2 Feynman Rules and Amplitudes

In the following, the Feynman rules for the models presented in Chap. 3 shall be presented. The kinetic and mass terms of the Lagrangian for fermions χ , scalar bosons ϕ and vector bosons V

$$\mathcal{L}_F = \bar{\chi} (i\not{\partial} - m) \chi \quad (\text{A.14a})$$

$$\mathcal{L}_S = \frac{1}{2}\partial_\mu \phi \partial^\mu \phi - \frac{1}{2}m_\phi^2 \phi^2 \quad (\text{A.14b})$$

$$\mathcal{L}_V = -\frac{1}{4}V^{\mu\nu}V_{\mu\nu} + \frac{1}{2}m_V^2 V^2 \quad (\text{A.14c})$$

lead to the following Feynman rules where the arrows on fermion lines denote the direction of the fermion flow while the arrows on boson lines show the direction of the momentum. Unless an arrow on a boson line states otherwise, the momentum is chosen to flow from left to right:

External fermion legs:

$$\text{---}\xrightarrow{p}\bullet = u(p) \quad (\text{A.15a})$$

$$\bullet \xrightarrow{p}\text{---} = \bar{u}(p) \quad (\text{A.15b})$$

$$\text{---}\xleftarrow{p}\bullet = v(p) \quad (\text{A.15c})$$

$$\bullet \xleftarrow{p}\text{---} = \bar{v}(p) \quad (\text{A.15d})$$

Fermion propagator:

$$\bullet \xrightarrow{p} \bullet = i \frac{\not{p} + m^2}{p^2 - m^2} \quad (\text{A.16a})$$

$$\bullet \xleftarrow{p} \bullet = i \frac{-\not{p} + m^2}{p^2 - m^2} \quad (\text{A.16b})$$

External scalar boson legs:

$$\bullet \text{---}\xrightarrow{p}\text{---} = 1 \quad (\text{A.17})$$

Scalar boson propagator:

$$\bullet \text{---}\xrightarrow{p}\text{---} \bullet = \frac{i}{p^2 - m^2} \quad (\text{A.18})$$

External vector boson legs:

$$\text{~~~~~}\xrightarrow{p}\bullet = \epsilon^\mu(p) \quad (\text{A.19a})$$

$$\bullet \text{~~~~~}\xrightarrow{p} = \epsilon^{\mu*}(p) \quad (\text{A.19b})$$

Vector boson propagator:

$$\bullet \text{~~~~~}\xrightarrow{p}\bullet = i \frac{-g^{\mu\nu} + (1 - \xi) \frac{p^\mu p^\nu}{p^2 - \xi m^2}}{p^2 - m^2} \quad (\text{A.20})$$

In Chap. 3, we introduce various models of DM self interaction, which contain the following vertices:

Yukawa interaction (fermion/scalar):

$$\mathcal{L}_{int} = g\phi\bar{\chi}\chi \quad \begin{array}{c} \text{---} \nearrow \bullet \text{---} \\ \nwarrow \text{---} \end{array} \text{---} = ig \quad (\text{A.21})$$

Gauge interaction (fermion/vector):

$$\mathcal{L}_{int} = gV_\mu\bar{\chi}\gamma^\mu\chi \quad \begin{array}{c} \text{---} \nearrow \bullet \text{---} \\ \nwarrow \text{---} \end{array} \text{---} = ig\gamma^\mu \quad (\text{A.22})$$

ϕ^3 and ϕ^4 interaction (scalar/scalar):

$$\mathcal{L}_{int} = A(\phi^\dagger\phi)\phi \quad \begin{array}{c} \text{---} \nearrow \bullet \text{---} \\ \nwarrow \text{---} \end{array} \text{---} = iA \quad (\text{A.23a})$$

$$\mathcal{L}_{int} = \frac{\lambda}{4}(\phi^\dagger\phi)^2 \quad \begin{array}{c} \text{---} \nearrow \bullet \text{---} \\ \nwarrow \text{---} \end{array} \text{---} = i\lambda \quad (\text{A.23b})$$

Gauge interaction (scalar/vector):

$$\mathcal{L}_{int} = igV^\mu [(\partial_\mu\phi^\dagger)\phi - \phi^\dagger(\partial_\mu\phi)] \quad \begin{array}{c} \text{---} \nearrow \bullet \text{---} \\ \nwarrow \text{---} \end{array} \text{---} = -ig(p+p')^\mu \quad (\text{A.24a})$$

$$\mathcal{L}_{int} = g^2(\phi^\dagger\phi)V^2 \quad \begin{array}{c} \text{---} \nearrow \bullet \text{---} \\ \nwarrow \text{---} \end{array} \text{---} = 2ig^2g^{\mu\nu} \quad (\text{A.24b})$$

For Majorana fermions, deducing Feynman rules is a bit more subtle than for Dirac fermions, since the fermion flow is not fixed, *i.e.* one cannot distinguish between particle and antiparticle. In order to construct Feynman rules in a tractable fashion, we follow the conventions of Ref. [31] who introduce a fermion flow (*i.e.* an orientation of a fermion line) in contrast to the fermion number flow of Dirac fermions, which is a new conserved quantity, which in this context means the orientation of a fermion line cannot change at a vertex and denote the orientation by an arrow next to the fermion line. The Feynman rules depend on the orientation with respect to the momentum flow but the differences cancel when computing the whole Feynman amplitude since

the orientation is a random choice which physical quantities should not depend on. We also use the fermion flow method to determine the relative sign of interfering Feynman graphs.

External fermion legs for Majorana fermions:

$$\overrightarrow{\quad\quad\quad} \bullet = u(p) \quad (A.25a)$$

$$\bullet \overrightarrow{\quad\quad\quad} = \bar{u}(p) \quad (A.25b)$$

$$\overleftarrow{\quad\quad\quad} \bullet = v(p) \quad (A.25c)$$

$$\bullet \overleftarrow{\quad\quad\quad} = \bar{v}(p) \quad (A.25d)$$

Majorana fermion propagator:

$$\bullet \overrightarrow{\quad\quad\quad} \bullet = i \frac{\not{p} + m^2}{p^2 - m^2} \quad (A.26a)$$

$$\bullet \overleftarrow{\quad\quad\quad} \bullet = i \frac{-\not{p} + m^2}{p^2 - m^2} \quad (A.26b)$$

Yukawa interaction (Majorana fermion/scalar):

$$\mathcal{L}_{int} = \frac{1}{2} g \phi \tilde{\chi}^2 \quad \begin{array}{c} \diagup \\ \diagdown \end{array} \begin{array}{c} \bullet \\ \bullet \end{array} \begin{array}{c} \diagdown \\ \diagup \end{array} \begin{array}{c} \text{---} \\ \text{---} \end{array} = \begin{array}{c} \diagup \\ \diagdown \end{array} \begin{array}{c} \bullet \\ \bullet \end{array} \begin{array}{c} \diagdown \\ \diagup \end{array} \begin{array}{c} \text{---} \\ \text{---} \end{array} = ig \quad (A.27)$$

Since we do not have diagrams with both Dirac and Majorana fermions, both orientations lead to the same amplitudes in our calculations.

Feynman Amplitudes for Fermion Scattering

Following the Feynman rules stated above, the Feynman amplitudes corresponding to the t-channel diagrams in Fig. 3.1 are for particle-particle scattering

$$\mathcal{A} = (+1) b(q) \bar{u}(p_4) \Gamma_2 u(p_2) \Delta(k) \bar{u}(p_3) \Gamma_3 S_F(p_3 + q) \Gamma_1 u(p_1) \quad (A.28a)$$

$$\mathcal{B} = (+1) b(q) \bar{u}(p_3) \Gamma_1 u(p_1) \Delta(k) \bar{u}(p_4) \Gamma_3 S_F(p_4 + q) \Gamma_2 u(p_2) \quad (A.28b)$$

$$\mathcal{C} = (+1) b(q) \bar{u}(p_4) \Gamma_2 u(p_2) \Delta(k) \bar{u}(p_3) \Gamma_1 S_F(p_1 - q) \Gamma_3 u(p_1) \quad (A.28c)$$

$$\mathcal{D} = (+1) b(q) \bar{u}(p_3) \Gamma_1 u(p_1) \Delta(k) \bar{u}(p_4) \Gamma_2 S_F(p_2 - q) \Gamma_3 u(p_2) \quad (A.28d)$$

and $p_3 \leftrightarrow p_4$ for the u-channel. Additionally, the exchange amplitudes obtain a relative sign due to the permutation of spinors relative to the chosen ordering (1,3,2,4).

For particle-antiparticle scattering, the t-channel diagrams are

$$\mathcal{A} = (-1) b(q) \bar{v}(p_2) \Gamma_2 v(p_4) \Delta(k) \bar{u}(p_3) \Gamma_3 S_F(p_3 + q) \Gamma_1 u(p_1) \quad (\text{A.29a})$$

$$\mathcal{B} = (-1) b(q) \bar{u}(p_3) \Gamma_1 u(p_1) \Delta(k) \bar{v}(p_2) \Gamma_2 S_F(-p_4 - q) \Gamma_3 v(p_4) \quad (\text{A.29b})$$

$$\mathcal{C} = (-1) b(q) \bar{v}(p_2) \Gamma_2 v(p_4) \Delta(k) \bar{u}(p_3) \Gamma_1 S_F(p_1 - q) \Gamma_3 u(p_1) \quad (\text{A.29c})$$

$$\mathcal{D} = (-1) b(q) \bar{u}(p_3) \Gamma_1 u(p_1) \Delta(k) \bar{v}(p_2) \Gamma_3 S_F(-p_2 + q) \Gamma_2 v(p_4) \quad (\text{A.29d})$$

and $p_1 \leftrightarrow -p_4$ plus a relative sign for the s-channel.

For Majorana particles, we have to consider all above channels plus the interference terms between s and u-channel. Following the Feynman rules in [31], we get for the s-channel

$$\mathcal{A}' = (+1) b(q) \bar{v}(p_1) \Gamma_1 v(p_4) \Delta(l) \bar{u}(p_3) \Gamma_3 S_F(p_3 + q) \Gamma_2 u(p_2) \quad (\text{A.30a})$$

$$\mathcal{B}' = (+1) b(q) \bar{u}(p_3) \Gamma_2 u(p_2) \Delta(l) \bar{v}(p_1) \Gamma_1 S_F(-p_4 - q) \Gamma_3 v(p_4) \quad (\text{A.30b})$$

$$\mathcal{C}' = (+1) b(q) \bar{u}(p_3) \Gamma_2 u(p_2) \Delta(l) \bar{v}(p_1) \Gamma_3 S_F(-p_1 + q) \Gamma_1 v(p_4) \quad (\text{A.30c})$$

$$\mathcal{D}' = (+1) b(q) \bar{v}(p_1) \Gamma_1 v(p_4) \Delta(l) \bar{u}(p_3) \Gamma_2 S_F(p_2 - q) \Gamma_3 u(p_2) \quad (\text{A.30d})$$

and $p_2 \leftrightarrow -p_4$ plus a relative sign for the u-channel.

In (A.28a) to (A.30d) Γ_1 and Γ_2 are the vertices connecting the fermions to the mediator, Γ_3 the vertex connecting the fermions to the emitted particle, $b(q)$ is the emitted particle's asymptotic state, which is either $b_{\text{scalar}}(k) = 1$ or $b_{\text{vector}}(k) = \epsilon_\mu^*(k)$ depending on the model, $u(p)$ and $v(p)$ are the asymptotic states of the fermions, $\Delta(p)$ is the mediator's propagator and $S_F(p)$ the fermion propagator.

Feynman Amplitudes for Scalar Boson Scattering

For scalar boson scattering, the amplitudes $\mathcal{A}\mathcal{D}$ can be adopted, but the spinors have to be replaced by the asymptotic states of scalar bosons $u(p) \rightarrow 1$ and $v(p) \rightarrow 1$ and the fermion propagator has to be replaced by a scalar propagator $S_F(p+q) \rightarrow \Delta(p+q)$ and the amplitudes do not gain a relative sign. The vertices have to be adapted following the corresponding Feynman rules. In addition to the amplitudes $\mathcal{A}\mathcal{D}$ we get two more

amplitudes \mathcal{E} and \mathcal{F} corresponding to the new diagrams in Fig. 3.6.

$$\mathcal{E} = b(q) \Gamma_2 \Delta(k) \Gamma_4 \quad (\text{A.31a})$$

$$\mathcal{F} = b(q) \Gamma_1 \Delta(k) \Gamma_4 \quad (\text{A.31b})$$

where Γ_4 is the vertex containing the mediator and the emitted boson. It is now trivial to deduce from the Feynman rules the missing amplitudes of the diagrams (g) to (i), but since we neglect these diagrams we do not write down the amplitudes explicitly.

A.3 Calculation of $|\mathcal{M}|^2$ for $\chi\chi \rightarrow \chi\chi\phi$

In this section, the full calculation of $|\mathcal{M}|^2$ for a scalar mediator and the emission of a scalar

$$\mathcal{L}_{int} = g_\phi \phi \bar{\chi} \chi \quad (\text{A.32})$$

shall be demonstrated. Using the Feynman rules in App. A.2, the Feynman diagram \mathcal{A} yields

$$\begin{aligned} \mathcal{A} &= \bar{u}(p_4) g_\phi u(p_2) \frac{1}{k^2 - m_\phi^2} \bar{u}(p_3) g_\phi \frac{\not{p}_3 + \not{q} + m_\chi}{(p_3 + q)^2 - m_\chi^2} g_\phi u(p_1) \\ &= g_\phi^3 \frac{1}{k^2 - m_\phi^2} \frac{1}{(p_3 + q)^2 - m_\chi^2} \bar{u}(p_4) u(p_2) \bar{u}(p_3) (\not{p}_3 + \not{q} + m_\chi) u(p_1) \end{aligned} \quad (\text{A.33})$$

where p_1 and p_2 are the momenta of the incoming particles, p_3 and p_4 the outgoing ones, k is the momentum transfer, q is the momentum of the emitted particle, m_ϕ is the mediator's mass, m_χ is the fermion mass and g_ϕ is the coupling strength which we assume to be < 1 for perturbation theory to work. For the computation of \mathcal{A}^* , one needs to make use of the following relations

$$\begin{aligned} (\gamma^0)^\dagger &= \gamma^0 & \gamma^0 \gamma^0 &= 1 \\ (\gamma^i)^\dagger &= -\gamma^i & \bar{u}(p) &= u^\dagger(p) \gamma^0. \end{aligned}$$

Thus follows

$$\mathcal{A}^* = g_\phi^3 \frac{1}{k^2 - m_\phi^2} \frac{1}{(p_3 + q)^2 - m_\chi^2} \bar{u}(p_1) (\not{p}_3 + \not{q} + m_\chi) u(p_3) \bar{u}(p_2) u(p_4) \quad (\text{A.34})$$

and without the prefactors, the squared matrix element (with spinor indices in latin letters) reads

$$|\mathcal{A}|^2 \propto \bar{u}_a(p_4) \mathbb{1}_{ab} u_b(p_2) \bar{u}_c(p_3) \mathbb{1}_{cd} (\not{p}_3 + \not{q} + m_\chi) \mathbb{1}_{de} u_e(p_1) \times \bar{u}_f(p_1) \mathbb{1}_{fg} (\not{p}_3 + \not{q} + m_\chi) \mathbb{1}_{gh} u_h(p_3) \bar{u}_i(p_2) \mathbb{1}_{ij} u_j(p_4) \quad (\text{A.35})$$

where we have added the the gamma identity matrices $\mathbb{1}$ at the vertices in order to emphasize that, generally, gamma matrices can enter the expression at these places. Keeping track of the spinor indices, we can now restructure (A.35) and using

$$\sum_{\text{spins}} u(p) \bar{u}(p) = \not{p} + m \quad (\text{A.36a})$$

$$\sum_{\text{spins}} v(p) \bar{v}(p) = \not{p} - m \quad (\text{A.36b})$$

yields the following expression:

$$\begin{aligned} \sum_{\text{spins}} |\mathcal{A}|^2 \propto & \sum_{\text{spins}} u_j(p_4) \bar{u}_a(p_4) \mathbb{1}_{ab} u_b(p_2) \bar{u}_i(p_2) \mathbb{1}_{ij} \\ & \times u_h(p_3) \bar{u}_c(p_3) \mathbb{1}_{cd} (\not{p}_3 + \not{q} + m_\chi) \mathbb{1}_{de} u_e(p_1) \bar{u}_f(p_1) \mathbb{1}_{fg} (\not{p}_3 + \not{q} + m_\chi) \mathbb{1}_{gh} \end{aligned} \quad (\text{A.37a})$$

$$\begin{aligned} = & \left(\not{p}_4 + m_\chi \right)_{ja} \mathbb{1}_{ab} \left(\not{p}_2 + m_\chi \right)_{bi} \mathbb{1}_{ij} \\ & \times \left(\not{p}_3 + m_\chi \right)_{hc} \mathbb{1}_{cd} \left(\not{p}_3 + \not{q} + m_\chi \right)_{de} \left(\not{p}_1 + m_\chi \right)_{ef} \mathbb{1}_{fg} \left(\not{p}_3 + \not{q} + m_\chi \right)_{gh} \end{aligned} \quad (\text{A.37b})$$

$$\begin{aligned} = & \underbrace{\text{tr} \left[\left(\not{p}_4 + m_\chi \right) \left(\not{p}_2 + m_\chi \right) \right]}_a \\ & \times \underbrace{\text{tr} \left[\left(\not{p}_3 + m_\chi \right) \left(\not{p}_3 + \not{q} + m_\chi \right) \left(\not{p}_1 + m_\chi \right) \left(\not{p}_3 + \not{q} + m_\chi \right) \right]}_b \end{aligned} \quad (\text{A.37c})$$

To evaluate the Dirac traces in (A.37c) one can use the properties of the gamma matrices

$$\text{tr}[\mathbb{1}] = 4 \quad (\text{A.38a})$$

$$\text{tr}[\gamma^\mu] = 0 \quad (\text{A.38b})$$

$$\text{tr}[\gamma^\mu \gamma^\nu] = 4g^{\mu\nu} \quad (\text{A.38c})$$

$$\text{tr}[\gamma^\mu \gamma^\nu \gamma^\sigma] = 0 \quad (\text{A.38d})$$

$$\text{tr}[\gamma^\mu \gamma^\nu \gamma^\sigma \gamma^\rho] = 4(g^{\mu\nu} g^{\sigma\rho} - g^{\mu\sigma} g^{\nu\rho} + g^{\mu\rho} g^{\nu\sigma}) \quad (\text{A.38e})$$

and thus

$$(a) = \text{tr} \left[\gamma_\mu p_4^\mu \gamma_\nu p_2^\nu + m_\chi \gamma_\mu p_2^\mu + m_\chi \gamma_\mu p_4^\mu + m_\chi^2 \right] \quad (\text{A.39a})$$

$$= 4(g_{\mu\nu} p_4^\mu p_2^\nu + m_\chi^2) \quad (\text{A.39b})$$

$$= 4(p_2 \cdot p_4 + m_\chi^2) \quad (\text{A.39c})$$

$$(b) = \text{tr} \left[(\gamma_\mu p_3^\mu + m_\chi) (\gamma_\nu p_3^\nu + \gamma_\nu q^\nu + m_\chi) (\gamma_\rho p_1^\rho + m_\chi) (\gamma_\sigma p_3^\sigma + \gamma_\sigma q^\sigma + m_\chi) \right] \quad (\text{A.39d})$$

$$= 4 \left(2(p_1 \cdot q)(p_3 \cdot q) + 2m_\chi^2(p_1 \cdot q) + 4m_\chi^2(p_3 \cdot q) + m_\chi^2 q^2 + 2p_3^2(p_1 \cdot q) \right. \\ \left. - q^2(p_1 \cdot p_3) + 3m_\chi^2(p_1 \cdot p_3) + 3m_\chi^2 p_3^2 + p_3^2(p_1 \cdot p_3) + m_\chi^4 \right) \quad (\text{A.39e})$$

In the next step, we want to use kinematic conditions to reduce the expression to a minimal set of momenta k , l , r and q . The connection to the Mandelstam variables is $k^2 = t$, $l^2 = u$, $r^2 = s$. Using that the momentum is conserved at each vertex, we get

$$q = p_1 + p_2 - p_3 - p_4 \quad (\text{A.40a})$$

$$k = p_2 - p_4 \quad (\text{A.40b})$$

$$= p_3 - p_1 + q$$

$$l = p_4 - p_1 \quad (\text{A.40c})$$

$$= p_2 - p_3 - q$$

$$r = p_1 + p_2 \quad (\text{A.40d})$$

$$= p_3 + p_4 + q$$

Using (A.40a) to (A.40d), we can express all possible scalar products in terms of the minimal set of momenta.

$$p_1 \cdot p_2 = m_\chi^2 - \frac{k^2 + l^2}{2} - k \cdot l \quad (\text{A.41a})$$

$$p_1 \cdot p_3 = m_\chi^2 - \frac{k^2 + q^2}{2} + k \cdot q \quad (\text{A.41b})$$

$$p_1 \cdot p_4 = m_\chi^2 - \frac{l^2}{2} \quad (\text{A.41c})$$

$$p_2 \cdot p_3 = m_\chi^2 - \frac{l^2 + q^2}{2} - l \cdot q \quad (\text{A.41d})$$

$$p_2 \cdot p_4 = m_\chi^2 - \frac{k^2}{2} \quad (\text{A.41e})$$

$$p_3 \cdot p_4 = m_\chi^2 - \frac{k^2 + l^2 + q^2}{2} + (k - l) \cdot q + k \cdot l \quad (\text{A.41f})$$

$$p_1 \cdot q = \frac{q^2}{2} - k \cdot q - k \cdot l \quad (\text{A.41g})$$

$$p_2 \cdot q = \frac{q^2}{2} + l \cdot q - k \cdot l \quad (\text{A.41h})$$

$$p_3 \cdot q = -\frac{q^2}{2} - k \cdot l \quad (\text{A.41i})$$

$$p_4 \cdot q = \frac{q^2}{2} + (l - k) \cdot q - k \cdot l \quad (\text{A.41j})$$

$$k \cdot p_1 = -\frac{k^2}{2} - k \cdot l \quad (\text{A.41k})$$

$$k \cdot p_2 = \frac{k^2}{2} \quad (\text{A.41l})$$

$$k \cdot p_3 = \frac{k^2}{2} - k \cdot q - k \cdot l \quad (\text{A.41m})$$

$$k \cdot p_4 = -\frac{k^2}{2} \quad (\text{A.41n})$$

$$l \cdot p_1 = -\frac{l^2}{2} \quad (\text{A.41o})$$

$$l \cdot p_2 = \frac{l^2}{2} + k \cdot l \quad (\text{A.41p})$$

$$l \cdot p_3 = -\frac{l^2}{2} - l \cdot q + k \cdot l \quad (\text{A.41q})$$

$$l \cdot p_4 = \frac{l^2}{2} \quad (\text{A.41r})$$

Only a few of them are needed for the calculation of $|\mathcal{A}|^2$, but for the full calculation of $|\mathcal{M}|^2$, all of them will be needed.

In order to make the calculation tractable, further calculations will be done in the non-relativistic limit, meaning that we assume the velocity of the fermions $v \ll 1$. Following this assumption, we incorporate the following power counting scheme

$$k^2 \approx -|\vec{k}|^2 \sim \mathcal{O}(m_\chi^2 v^2) \quad (\text{A.42a})$$

$$l^2 \approx -|\vec{l}|^2 \sim \mathcal{O}(m_\chi^2 v^2) \quad (\text{A.42b})$$

$$r^2 \approx 4m_\chi^2 + |\vec{k}|^2 + |\vec{l}|^2 + 2(\vec{k} \cdot \vec{l}) \sim \mathcal{O}(m_\chi^2) \quad (\text{A.42c})$$

$$k \cdot l \approx -(\vec{k} \cdot \vec{l}) \sim \mathcal{O}(m_\chi^2 v^2) \quad (\text{A.42d})$$

$$k \cdot r \approx (\vec{k} \cdot \vec{l}) \sim \mathcal{O}(m_\chi^2 v^2) \quad (\text{A.42e})$$

$$l \cdot r \approx -(\vec{k} \cdot \vec{l}) \sim \mathcal{O}(m_\chi^2 v^2) \quad (\text{A.42f})$$

$$k \cdot q \approx -(\vec{k} \cdot \vec{q}) \sim \mathcal{O}(m_\chi^2 v^3) \quad (\text{A.42g})$$

$$l \cdot q \approx -(\vec{l} \cdot \vec{q}) \sim \mathcal{O}(m_\chi^2 v^3) \quad (\text{A.42h})$$

$$r \cdot q \approx 2m_\chi \omega - (\vec{r} \cdot \vec{q}) \sim \mathcal{O}(m_\chi^2 v^2) \quad (\text{A.42i})$$

and in order for the emitted particle to be produced on-shell

$$q^2 = m_\phi^2 < 4m_\chi^2 v^4 \quad (\text{A.43})$$

Applying the replacements and the on-shell conditions $p_1 = p_2 = p_3 = p_4 = m^2$ on

$$\begin{aligned} \sum_{\text{spin}} |\mathcal{A}|^2 = & \frac{16g_\phi^6}{(k^2 - m_\phi^2)^2} \frac{1}{((p_3 + q)^2 - m_\chi^2)^2} \left(p_2 \cdot p_4 + m_\chi^2 \right) \left(2(p_1 \cdot q)(p_3 \cdot q) \right. \\ & + 2m_\chi^2(p_1 \cdot q) + 4m_\chi^2(p_3 \cdot q) + m_\chi^2 q^2 + 2p_3^2(p_1 \cdot q) - q^2(p_1 \cdot p_3) \\ & \left. + 3m_\chi^2(p_1 \cdot p_3) + 3m_\chi^2 p_3^2 + p_3^2(p_1 \cdot p_3) + m_\chi^4 \right) \end{aligned} \quad (\text{A.44})$$

and expanding the expression for small v yields

$$\begin{aligned} \sum_{\text{spin}} |\mathcal{A}|^2 = & \frac{4g_\phi^6}{\omega^2 (|\vec{k}|^2 + m_\phi^2)^2} \left(\underbrace{16m_\chi^4}_{\mathcal{O}(1)} + \underbrace{8m_\chi^2 |\vec{k}|^2 + 16|\vec{k}||\vec{l}|(\hat{k} \cdot \hat{l})}_{\mathcal{O}(v^2)} \right. \\ & \left. + \underbrace{|\vec{k}|^4 + 4|\vec{k}|^3 |\vec{l}|(\hat{k} \cdot \hat{l}) + 16|\vec{k}|^2 |\vec{l}|^2 (\hat{k} \cdot \hat{l})^2}_{\mathcal{O}(v^4)} + \mathcal{O}(v^6) \right) \end{aligned} \quad (\text{A.45})$$

where ω is the emitted particle's energy. All terms in (A.45) except the last one will cancel identically with other diagrams in the t-channel.

For the calculation of the other diagonal elements in the t-channel $|\mathcal{B}|^2$, $|\mathcal{C}|^2$ and $|\mathcal{D}|^2$, one can use exactly the same procedure as for $|\mathcal{A}|^2$. The interference terms $(\mathcal{A}\mathcal{B}^* + \mathcal{B}\mathcal{A}^*)$, $(\mathcal{A}\mathcal{C}^* + \mathcal{C}\mathcal{A}^*)$..., however, contain scalar products involving the 3-momentum of the emitted particle \vec{q} . Since, in future calculations, we will not be interested in the direction of \vec{q} , we can do an angular average right away

$$\langle (\hat{k} \cdot \hat{q}) \rangle = \langle (\hat{l} \cdot \hat{q}) \rangle = \langle (\hat{r} \cdot \hat{q}) \rangle = 0 \quad (\text{A.46a})$$

$$\langle (\hat{k} \cdot \hat{q})^2 \rangle = \langle (\hat{l} \cdot \hat{q})^2 \rangle = \langle (\hat{r} \cdot \hat{q})^2 \rangle = \frac{1}{3} \quad (\text{A.46b})$$

$$\langle (\hat{k} \cdot \hat{q})(\hat{l} \cdot \hat{q}) \rangle = \frac{\hat{k} \cdot \hat{l}}{3} \quad (\text{A.46c})$$

$$\langle (\hat{k} \cdot \hat{q})(\hat{r} \cdot \hat{q}) \rangle = \frac{\hat{k} \cdot \hat{r}}{3} \quad (\text{A.46d})$$

$$\langle (\hat{l} \cdot \hat{q})(\hat{r} \cdot \hat{q}) \rangle = \frac{\hat{l} \cdot \hat{r}}{3} \quad (\text{A.46e})$$

Following the same procedure for all other amplitudes of the t and u -channel, we get for the direct and exchange terms

$$\sum_{\text{spin}} |\mathcal{A} + \mathcal{B} + \mathcal{C} + \mathcal{D}|^2 = \frac{256}{9} \frac{g_\phi^6}{\omega^2} \frac{|\vec{k}|^2 |\vec{l}|^2 (1 + 3(\hat{k} \cdot \hat{l})^2)}{(|\vec{k}|^2 + m_\phi^2)^2} \quad (\text{A.47})$$

$$\sum_{\text{spin}} |\mathcal{A}' + \mathcal{B}' + \mathcal{C}' + \mathcal{D}'|^2 = \frac{256}{9} \frac{g_\phi^6}{\omega^2} \frac{|\vec{k}|^2 |\vec{l}|^2 (1 + 3(\hat{k} \cdot \hat{l})^2)}{(|\vec{l}|^2 + m_\phi^2)^2} \quad (\text{A.48})$$

The interference terms are more difficult to evaluate, because they involve longer Dirac traces and therefore yield much longer expressions, but thoroughly following the above

steps, we get

$$\sum_{\text{spin}} (\mathcal{A}^* + \mathcal{B}^* + \mathcal{C}^* + \mathcal{D}^*) (\mathcal{A}' + \mathcal{B}' + \mathcal{C}' + \mathcal{D}') + h.c. = -\frac{256}{9} \frac{g_\phi^6}{\omega^2} \frac{|\vec{k}|^2 |\vec{l}|^2 (1 + 3(\hat{k} \cdot \hat{l})^2)}{(|\vec{k}|^2 + m_\phi^2)(|\vec{l}|^2 + m_\phi^2)} \quad (\text{A.49})$$

The terms involving annihilation diagrams are suppressed by at least a factor $k^2/r^2 \sim v^2$ in the scalar propagator and therefore only contribute to higher order corrections in v .

A.4 Phase Space Integration

In order to calculate the cross section σ , one has to evaluate the phase space integral

$$\sigma = \frac{S_f (2\pi)^4}{(2E_1)(2E_2)|\vec{v}_1 - \vec{v}_2|} \int \frac{d^3 p_3}{(2\pi)^3 2E_3} \frac{d^3 p_4}{(2\pi)^3 2E_4} \int \frac{d^3 q}{(2\pi)^3 2\omega} |\mathcal{M}|^2 \delta^{(4)}(p_1 + p_2 - p_3 - p_4 - q) \quad (\text{A.50})$$

whereas $|\mathcal{M}|^2$ (summed over initial and final spins) is generally a function of all 4-momenta p_1, p_2, p_3, p_4 and q minus the degrees of freedom that can be eliminated due to kinematical constraints. In the non-relativistic limit and for the emission of a light particle, one can replace $d^3 p_i/2E_i \approx d^3 p_i/2m$, $E_i \approx m + p_i^2/2m$ for $i \in [1, 4]$ in the energy δ -function and one can neglect the emitted particle's momentum in the momentum δ function. This allows us to trivially integrate over one of the 3-momenta to get

$$\sigma = \frac{1}{|\vec{v}_1 - \vec{v}_2|} \frac{S_f}{m_\chi^4 2^{10} \pi^5} \int d^3 p_3 d^3 q \frac{1}{\omega} \frac{1}{g_\chi^2} |\mathcal{M}|^2 \delta\left(\frac{|\vec{p}_1|^2 + |\vec{p}_2|^2 - |\vec{p}_3|^2 - |\vec{p}_4|^2}{2m_\chi} - \omega\right) \quad (\text{A.51})$$

with $\vec{p}_4 = \vec{p}_1 + \vec{p}_2 - \vec{p}_3$. The factor g_χ accounts for the number of spin states in the initial states. Furthermore, one can simplify the integration by introducing center-of-mass (CM) momenta such that

$$\begin{aligned} \vec{p}_1 &= \vec{P} + \vec{p}_i & \vec{p}_2 &= \vec{P} - \vec{p}_i \\ \vec{p}_3 &= \vec{P} + \vec{p}_f & \vec{p}_4 &= \vec{P} - \vec{p}_f \end{aligned}$$

Replacing the external momenta with the CM momenta \vec{P} , \vec{p}_i and \vec{p}_f yields for the cross section in the CM frame

$$\begin{aligned}\sigma &= \frac{1}{|2\vec{p}_i|} \frac{S_f}{m_\chi^3 2^{10} \pi^5} \int d^3 p_f d^3 q \frac{1}{\omega} \frac{1}{g_\chi^2} |\mathcal{M}|^2 \delta\left(\frac{|\vec{p}_i|^2 - |\vec{p}_f|^2}{m_\chi} - \omega\right) \\ &= \frac{1}{|2\vec{p}_i|} \frac{S_f}{m_\chi^3 2^8 \pi^4 g_\chi^2} \int d\Omega_f dp_f p_f^2 d\omega \omega |\mathcal{M}|^2 \delta\left(\frac{|\vec{p}_i|^2 - |\vec{p}_f|^2}{m_\chi} - \omega\right)\end{aligned}\quad (\text{A.52})$$

where in the second line we have used that the angular integration for the emitted particle only gives a trivial factor 4π because we have already done an angular average in the calculation of the squared matrix element. In addition, we assumed that the emitted particle has a very small mass, such that $|\vec{q}| \approx \omega$.

In the next step, we want to calculate the energy loss rate

$$\dot{\epsilon} = \frac{S_i g_\chi^2}{(2\pi)^6} \int d^3 p_1 d^3 p_2 f(E_1) f(E_2) |\vec{v}_1 - \vec{v}_2| \int d\omega \omega \frac{d\sigma}{d\omega} \quad (\text{A.53})$$

with

$$\frac{d\sigma}{d\omega} = \frac{\omega}{|2\vec{p}_i|} \frac{S_f}{m_\chi^3 2^8 \pi^4 g_\chi^2} \int d\Omega_f dp_f p_f^2 |\mathcal{M}|^2 \delta\left(\frac{|\vec{p}_i|^2 - |\vec{p}_f|^2}{m_\chi} - \omega\right) \quad (\text{A.54})$$

Again, we rewrite in terms of CM momenta and with the Jacobian $\left| \frac{\partial(\vec{p}_1, \vec{p}_2)}{\partial(\vec{P}, \vec{p}_i)} \right| = 8$ we get

$$\dot{\epsilon} = \frac{8 S_i g_\chi^2}{(2\pi)^6} \int d^3 P d^3 p_i f(E_1) f(E_2) \frac{|2\vec{p}_i|}{m} \int d\omega \omega \frac{d\sigma}{d\omega} \quad (\text{A.55})$$

In the non-degenerate limit we can use a Maxwell-Boltzmann distribution for the fermions/bosons

$$f(p) = \frac{n_\chi}{g_\chi} \left(\frac{2\pi}{m_\chi T} \right)^{3/2} e^{-\frac{p^2}{2mT}} \quad (\text{A.56})$$

such that the number density $n_\chi = g_\chi / (2\pi)^3 \int d^3 p f(p)$. The factor g_χ accounts for the number of possible spin configurations in the initial states. Introducing the dimensionless quantities

$$u_i = \frac{p_i^2}{m_\chi T} \quad (\text{A.57a})$$

$$u_f = \frac{p_f^2}{m_\chi T} \quad (\text{A.57b})$$

$$x = \frac{\omega}{T} \quad (\text{A.57c})$$

$$y = \frac{m_\phi^2}{m_\chi T} \quad (\text{A.57d})$$

$$z = \frac{\vec{p}_i \cdot \vec{p}_f}{|\vec{p}_i| |\vec{p}_f|} = \cos \theta_{if} \quad (\text{A.57e})$$

we can rewrite

$$d^3 p_f = d\Omega_f dp_f p_f^2 \quad (\text{A.58a})$$

$$d\Omega_f = 2\pi dz \quad (\text{A.58b})$$

$$dp_f p_f^2 = \frac{(m_\chi T)^{3/2}}{2} \sqrt{u_f} du_f \quad (\text{A.58c})$$

$$d^3 q = d\Omega_q dq q^2 \quad (\text{A.58d})$$

$$d\Omega_q = 4\pi \quad (\text{A.58e})$$

$$dq q^2 = T^3 x^2 dx \quad (\text{A.58f})$$

to get

$$\dot{\epsilon} = \frac{8S_i g_\chi^2}{(2\pi)^6} \int d^3 P d^3 p_i f(E_1) f(E_2) \frac{|2\vec{p}_i|}{m} \int d\omega \omega \frac{d\sigma}{d\omega} \quad (\text{A.59a})$$

$$= \frac{S_i m_\chi T^3}{2\pi^5} n_\chi^2 \left(\frac{2\pi}{m_\chi T} \right)^3 \underbrace{\int d^3 P e^{-\frac{P^2}{m_\chi T}}}_{(\pi m T)^{3/2}} \int_0^\infty du_i u_i e^{-u_i} \int_0^\infty dx x \frac{d\sigma}{dx} \quad (\text{A.59b})$$

$$= \frac{4S_i n_\chi^2 T^{3/2}}{\pi^{1/2} m_\chi^{1/2}} \int_0^\infty du_i u_i e^{-u_i} \int_0^\infty dx x \frac{d\sigma}{dx} \quad (\text{A.59c})$$

$$= \frac{S n_\chi^2 T^{7/2}}{2^7 g_\chi^2 \pi^{7/2} m_\chi^{5/2}} \int_0^\infty du_i \sqrt{u_i} e^{-u_i} \int_0^\infty du_f \sqrt{u_f} \int_0^\infty dx x^2 \int_{-1}^1 dz |\mathcal{M}|^2 \delta(u_i - u_f - x) \quad (\text{A.59d})$$

whereas $S = S_i \cdot S_f$ is a symmetry factor for identical particles in the initial and final state. Executing the u_f -integration in (A.59d) yields

$$\dot{\epsilon} = \frac{S n_\chi^2}{2^7 g_\chi^2} \frac{T^{7/2}}{\pi^{7/2} m_\chi^{5/2}} \int_0^\infty du e^{-u} \int_0^u dx \sqrt{u(u-x)} x^2 \int_{-1}^1 dz |\mathcal{M}(u, x, y, z)|^2 \quad (\text{A.60})$$

The squared matrix element $|\mathcal{M}|^2$, as we calculated it in App. A.3 will usually be a function of $|\vec{k}|^2$, $|\vec{l}|^2$ and $(\vec{k} \cdot \vec{l})$, which we can rewrite in terms of dimensionless variables in the following way

$$\begin{aligned} \frac{|\vec{k}|^2}{m_\chi T} &= u_i + u_f - 2z\sqrt{u_i u_f} \\ &= 2u - x - 2z\sqrt{u(u-x)} \end{aligned} \tag{A.61a}$$

$$\begin{aligned} \frac{|\vec{l}|^2}{m_\chi T} &= u_i + u_f + 2z\sqrt{u_i u_f} \\ &= 2u - x + 2z\sqrt{u(u-x)} \end{aligned} \tag{A.61b}$$

$$\begin{aligned} \frac{\vec{k} \cdot \vec{l}}{m_\chi T} &= u_i - u_f \\ &= x \end{aligned} \tag{A.61c}$$

with $u = u_i = u_f + x$.

References

- [1] Gianfranco Bertone, Dan Hooper, and Joseph Silk. “Particle dark matter: evidence, candidates and constraints”. In: *Physics Reports* 405.5–6 (2005), pp. 279–390. ISSN: 0370-1573.
- [2] F. Zwicky. “Die Rotverschiebung von extragalaktischen Nebeln”. In: *Helvetica Physica Acta* 6 (1933), pp. 110–127.
- [3] F. Zwicky. “On the Masses of Nebulae and of Clusters of Nebulae”. In: *Astrophys. J.* 86 (Oct. 1937), p. 217.
- [4] Vera C Rubin and W Kent Jr Ford. “Rotation of the Andromeda Nebula from a Spectroscopic Survey of Emission Regions”. In: *Astrophys. J.* 159 (Jan. 1970), p. 379.
- [5] V. C. Rubin, N. Thonnard, and W. K. Ford Jr. “Rotational properties of 21 SC galaxies with a large range of luminosities and radii, from NGC 4605 $R = 4$ kpc to UGC 2885 $R = 122$ kpc”. In: *Astrophys. J.* 238 (1980), p. 471.
- [6] M Markevitch et al. “Direct Constraints on the Dark Matter Self-Interaction Cross Section from the Merging Galaxy Cluster 1E 0657–56”. In: *Astrophys J.* 606.2 (May 2004), pp. 819–824.
- [7] Timothy Clifton et al. “Modified gravity and cosmology”. In: *Physics Reports* 513.1–3 (2012). Modified Gravity and Cosmology, pp. 1–189. ISSN: 0370-1573.
- [8] David H. Weinberg et al. “Cold dark matter: controversies on small scales”. In: (2013). arXiv: 1306.0913 [astro-ph.CO].
- [9] David N. Spergel and Paul J. Steinhardt. “Observational Evidence for Self-Interacting Cold Dark Matter”. In: *Phys. Rev. Lett.* 84 (17 2000), pp. 3760–3763.
- [10] Planck Collaboration et al. “Planck 2015 results. XIII. Cosmological parameters”. In: *arXiv.org* (Feb. 2015). arXiv: 1502.01589v2 [astro-ph.CO].

-
- [11] Stefano Borgani and Luigi Guzzo. “X-ray clusters of galaxies as tracers of structure in the Universe : Article : Nature”. In: *Nature* 409.6816 (Jan. 2001), pp. 39–45.
 - [12] Edward Kolb and Michael Turner. *The Early Universe*. New York: Westview Press, 1994. ISBN: 081-3-346-452-.
 - [13] James Binney and Scott Tremaine. *Galactic Dynamics*. 2nd ed. Kassel: Princeton University Press, 2011. ISBN: 140-0-828-724-.
 - [14] Houjun Mo, Frank van den Bosch, and Simon White. *Galaxy Formation and Evolution*. Cambridge University Press, May 2010.
 - [15] Max Tegmark et al. “How Small Were the First Cosmological Objects?” In: *Astrophys. J.* 474.1 (1997), p. 1.
 - [16] Jeremy L Tinker et al. “Toward a halo mass function for precision cosmology: the limits of universality”. In: *arXiv.org* 2 (Mar. 2008), pp. 709–728. arXiv: 0803.2706v1 [astro-ph].
 - [17] Edmund Bertschinger. “Simulations of structure formation in the universe”. In: *Annual Review of Astronomy and Astrophysics* 36.1 (1998), pp. 599–654.
 - [18] G. Kauffmann, S. D. M. White, and B. Guiderdoni. “The formation and evolution of galaxies within merging dark matter haloes”. In: *Monthly Notices of the Royal Astronomical Society* 264.1 (1993), pp. 201–218.
 - [19] Anatoly Klypin et al. “Where Are the Missing Galactic Satellites?” In: *Astrophys. J.* 522.1 (1999), p. 82.
 - [20] Ben Moore et al. “Dark Matter Substructure within Galactic Halos”. In: *Astrophys. J. Lett.* 524.1 (1999), p. L19.
 - [21] Renyue Cen and Jeremiah P Ostriker. “Where are the baryons? 2. feedback effects”. In: *Mon. Not. Roy. Astron. Soc.* 650.2 (2006), pp. 560–572.
 - [22] Michael Boylan-Kolchin, James S. Bullock, and Manoj Kaplinghat. “Too big to fail? The puzzling darkness of massive Milky Way subhaloes”. In: *Monthly Notices of the Royal Astronomical Society: Letters* 415.1 (2011), pp. L40–L44.
 - [23] Papastergis, E. et al. “Is there a “too big to fail” problem in the field?” In: *Astronomy and Astrophysics* 574 (2015), A113.
 - [24] W. J. G. de Blok. “The Core-Cusp Problem”. In: *Adv. Astron.* 2010 (2010), p. 789293. arXiv: 0910.3538 [astro-ph.CO].
 - [25] Benjamin D. Wandelt et al. “Selfinteracting dark matter”. In: (2000), pp. 263–274. arXiv: astro-ph/0006344 [astro-ph].

-
- [26] Oliver D. Elbert et al. “Core formation in dwarf haloes with self-interacting dark matter: no fine-tuning necessary”. In: *Monthly Notices of the Royal Astronomical Society* 453.1 (2015), pp. 29–37.
 - [27] Leanne D Duffy and Karl van Bibber. “Axions as dark matter particles”. In: *New Journal of Physics* 11.10 (Oct. 2009), p. 105008.
 - [28] Matthew D. Schwartz. *Quantum Field Theory and the Standard Model*. New. Cambridge: Cambridge University Press, 2014. ISBN: 978-1-107-03473-0.
 - [29] M J Rees and J P Ostriker. “Cooling, dynamics and fragmentation of massive gas clouds: clues to the masses and radii of galaxies and clusters”. In: *Monthly Notices of the Royal Astronomical Society* 179.4 (Aug. 1977), pp. 541–559.
 - [30] JiJi Fan et al. “A Dark-Disk Universe”. In: *arXiv.org* 21 (Mar. 2013), p. 211302. arXiv: 1303.3271v2 [hep-ph].
 - [31] Ansgar Denner et al. “Feynman rules for fermion number violating interactions”. In: *Nucl. Phys.* B387 (1992), pp. 467–484.
 - [32] Sean Tulin, Hai-Bo Yu, and Kathryn M Zurek. “Beyond Collisionless Dark Matter: Particle Physics Dynamics for Dark Matter Halo Structure”. In: *arXiv.org* 11 (Feb. 2013), p. 115007. arXiv: 1302.3898v1 [hep-ph].
 - [33] V B Berestetskii, L. P. Pitaevskii, and E.M. Lifshitz. *Quantum Electrodynamics*. 2. Aufl. Oxford: Butterworth-Heinemann, 2012. ISBN: 978-0-080-50346-2.
 - [34] Henri Ruegg and Marti Ruiz-Altaba. “The Stueckelberg Field”. In: *arXiv.org* 20 (Apr. 2003), pp. 3265–3347. arXiv: hep-th/0304245v2 [hep-th].
 - [35] Paul Langacker. *The Standard Model and Beyond*. Boca Raton, Fla: CRC Press, 2009. ISBN: 978-1-420-07907-4.